COMMUNICATIONS

Dear reader,

Theoretical and experimental solutions of technical problems meeting their purposes in a given period do not bring about such serious problems within society as the current impact of the economic crisis does.

If we want mechanical engineering to maintain its previous important position of the force influencing the growth of national economy also in the future, it will be necessary to pay continuous attention to the issues relating to economical use of eco-friendly raw materials.

In this volume of the Scientific Letters you will have an opportunity to read papers written by authors who are specialists in their field. You will find a topic dealing with a stress sensitivity analysis of the beam and shell finite elements; a paper presenting a non-traditional computational approach for a structural analysis with uncertainties in materials, geometry and load parameters; an article describing a new method of continuous source functions used for composites reinforced by finite length fibres with a large aspect ratio and composites reinforced with spherical inclusions. In another article the authors discuss steps towards the design, construction and production of a device used for lifetime assessment of large-scale bearings; other authors offer their research results from gaseous emissions of a combined cogeneration unit. The topics of the railway wheel unroundness and railway wheel profile design are dealt with in the two next articles.

I believe that each of you will find something which makes you think of possible innovative steps in your own field of research.

Vladimir Hlavna

Milan Saga – Milan Vasko *

STRESS SENSITIVITY ANALYSIS OF THE BEAM AND SHELL FINITE ELEMENTS

The stress sensitivity analysis in conjunction with finite elements method represents an important tool for the influence analysis of the structural parameters. This analysis plays a significant role in the decision process of the formulation of the structural optimizing or probability analysis. The goal of the paper is to present theoretic and numerical aspects of the beam and shell element stress sensitivity analysis with the respect to the cross section parameters (cross section area, thickness, etc.). The whole computational procedure was inbuilt into Matlab's software module MATFEM.

Keywords: stress sensitivity analysis, beam, thin shell element, Matlab

1. Introduction

Nowadays the sensitivity analysis is a significant tool helping to realize a structural parameters influence analysis. This analysis is usually very computer time consuming but the results are very innovative. This process is often applied to a structural analysis, i.e. in stress and strain analysis, modal and spectral or buckling analysis, stochastic analysis and so on [3, 6].

Application of the sensitivity analysis is not associated only with the structural optimizing but also with the analysis of the mechanical systems with uncertain parameters, mainly in the usage of so-called perturbation methods based on differentiation of the response with respect to the uncertain system parameters (stiffness, mass, damping, etc.). Implementation of this computational process into the finite element method characterized mainly the era of development of structural optimizing techniques in the eighties.

2. Stress sensitivity analysis for beam finite element

We will consider classic linear two-nodes beam element with a constant cross section (There is more information in [1, 5].).

Let's consider only a well-known linear distribution of the normal stress, i.e.

$$\sigma_x = \frac{N_x}{A} - \frac{M_{oz}}{J_z}\cdot y + \frac{M_{oy}}{J_y}\cdot z\,, \tag{1}$$

where N_x is the internal axial force, M_{oz} and M_{oy} are bending moments, A is the element cross-section area, J_z and J_y are moments of inertia [2, 5, 7, 8].

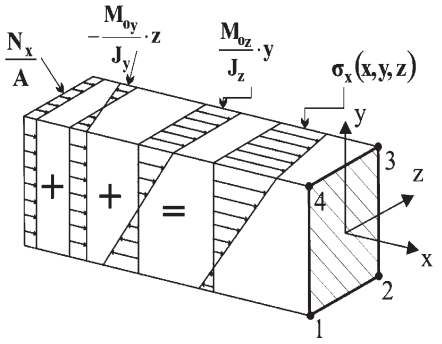

Fig. 1 Stress distribution in beam

If the bending moment is [1, 6]

$$M_o(x) = \left[\left(1 - \frac{x}{l}\right)\frac{x}{l}\right]\cdot\begin{bmatrix}M_{o1}\\ M_{o2}\end{bmatrix}, \tag{2}$$

than the normal stress function is following

$$\sigma_x(x,y,z) = \left\{0\,0\,0\,0\left[\frac{z}{J_y}\cdot\left(1-\frac{x}{l}\right)\right]\left[-\frac{y}{J_z}\cdot\left(1-\frac{x}{l}\right)\right]\cdot\right.$$
$$\left.\cdot\left(\frac{1}{A}\right)0\,0\,0\left(\frac{z}{J_y}\cdot\frac{x}{l}\right)\left(-\frac{y}{J_z}\cdot\frac{x}{l}\right)\right\}\cdot \tag{3}$$
$$\cdot\left[N_{x1}\,T_{y1}\,T_{z1}\,M_{k1}\,M_{y1}\,M_{z1}N_{x2}\,T_{y2}\,T_{z2}\,M_{k2}\,M_{y2}\,M_{z2}\right]^T\quad.$$

In agreement with points in Fig. 1 it is possible to write the relationship between normal stress in these marginal points of the cross-section and internal elements forces and moments, i.e.

* **Milan Saga, Milan Vasko**
Department of Applied Mechanics, Faculty of Mechanical Engineering, University of Zilina, E-mail: milan.saga@fstroj.uniza.sk

$$\begin{Bmatrix}\sigma_{x11}\\ \sigma_{x12}\\ \sigma_{x13}\\ \sigma_{x14}\\ \sigma_{x21}\\ \sigma_{x22}\\ \sigma_{x23}\\ \sigma_{x24}\end{Bmatrix}=\begin{Bmatrix}0&0&0&0&\frac{z_1}{J_y}&-\frac{y_1}{J_z}&\frac{1}{A}&0&0&0&0&0\\ 0&0&0&0&\frac{z_2}{J_y}&-\frac{y_2}{J_z}&\frac{1}{A}&0&0&0&0&0\\ 0&0&0&0&\frac{z_3}{J_y}&-\frac{y_3}{J_z}&\frac{1}{A}&0&0&0&0&0\\ 0&0&0&0&\frac{z_4}{J_y}&-\frac{y_4}{J_z}&\frac{1}{A}&0&0&0&0&0\\ 0&0&0&0&0&0&\frac{1}{A}&0&0&0&\frac{z_1}{J_y}&-\frac{y_1}{J_z}\\ 0&0&0&0&0&0&\frac{1}{A}&0&0&0&\frac{z_2}{J_y}&-\frac{y_2}{J_z}\\ 0&0&0&0&0&0&\frac{1}{A}&0&0&0&\frac{z_3}{J_y}&-\frac{y_3}{J_z}\\ 0&0&0&0&0&0&\frac{1}{A}&0&0&0&\frac{z_4}{J_y}&-\frac{y_4}{J_z}\end{Bmatrix}\cdot\begin{Bmatrix}N_{x1}\\ T_{y1}\\ T_{z1}\\ M_{k1}\\ M_{y1}\\ M_{z1}\\ N_{x2}\\ T_{y2}\\ T_{z2}\\ M_{k2}\\ M_{y2}\\ M_{z2}\end{Bmatrix} \quad (4)$$

or

$$\boldsymbol{\sigma}_L^j=\mathbf{C}_L^j\cdot\mathbf{f}_L^j, \quad (5)$$

The stress sensitivity centre is the derivative (5) with respect to a design variable X_i, i.e.

$$\frac{\partial\boldsymbol{\sigma}_L^j}{\partial X_i}=\frac{\partial\mathbf{C}_L^j}{\partial X_i}\cdot\mathbf{f}_L^j+\mathbf{C}_L^j\cdot\frac{\partial\mathbf{f}_L^j}{\partial X_i}. \quad (6)$$

Using the well-known finite element theory, the internal forces vector $\mathbf{f}_L^j$ in the local coordinate system is given by

$$\mathbf{f}_L^j=\mathbf{K}_L^j\cdot\mathbf{u}_L^j=\mathbf{K}_L^j\cdot\mathbf{T}_{LG}^j\cdot\mathbf{T}_{01}^j\cdot\mathbf{K}_G^{-1}\cdot\mathbf{f}_G, \quad (7)$$

where $\mathbf{K}_G$ is the global stiffness matrix (in the global coordinate system), $\mathbf{f}_G$ is the external nodal forces vector (in the global coordinate system), $\mathbf{T}_{LG}^j$ is a transformation matrix between the local and global coordinate systems, $\mathbf{T}_{01}^j$ is a Boolean matrix, i.e. the localization matrix determining the element position in the global stiffness matrix, it means

$$\mathbf{u}_G^j=\mathbf{T}_{01}^j\cdot\mathbf{u}_G. \quad (8)$$

Let's now realize the derivation of the internal nodal forces vector (7) with respect to X_i:

$$\frac{\partial\mathbf{f}_L^j}{\partial X_i}=\frac{\partial\mathbf{K}_L^j}{\partial X_i}\cdot\mathbf{u}_L^j+\mathbf{K}_L^j\cdot\frac{\partial\mathbf{u}_L^j}{\partial X_i}=\frac{\partial\mathbf{K}_L^j}{\partial X_i}\cdot\mathbf{T}_{LG}^j\cdot\mathbf{T}_{01}^j\cdot\mathbf{K}_G^{-1}\cdot\\ \cdot\mathbf{f}_G+\mathbf{K}_L^j\cdot\frac{\partial\mathbf{u}_L^j}{\partial X_i}. \quad (9)$$

Applying the derivation on the well-known "FEA" equation $\mathbf{K}_G\cdot\mathbf{u}_G=\mathbf{f}_G$ we can write

$$\frac{\partial\mathbf{K}_G}{\partial X_i}\cdot\mathbf{u}_G+\mathbf{K}_G\cdot\frac{\partial\mathbf{u}_G}{\partial X_i}=\frac{\partial\mathbf{f}_G}{\partial X_i}. \quad (10)$$

where

$$\frac{\partial\mathbf{K}_G}{\partial X_i}=\sum_{j=1}^{ni}\mathbf{T}_{01}^{j\,T}\cdot\mathbf{T}_{LG}^{j\,T}\cdot\frac{\partial\mathbf{K}_L^j}{\partial X_i}\cdot\mathbf{T}_{LG}^j\cdot\mathbf{T}_{01}^j, \quad (11)$$

and n_i is a number of all the elements containing X_i. Further, the gradient of a global vector of the nodal displacements can be following

$$\frac{\partial\mathbf{u}_G}{\partial X_i}=\mathbf{K}_G^{-1}\cdot\left(\frac{\partial\mathbf{f}_G}{\partial X_i}-\frac{\partial\mathbf{K}_G}{\partial X_i}\cdot\mathbf{u}_G\right)=\mathbf{K}_G^{-1}\cdot\left[\frac{\partial\mathbf{f}_G}{\partial X_i}-\right.\\ \left.-\sum_{j=1}^{ni}\left(\mathbf{T}_{01}^{j\,T}\cdot\mathbf{T}_{LG}^{j\,T}\cdot\frac{\partial\mathbf{K}_L^j}{\partial X_i}\cdot\mathbf{T}_{LG}^j\cdot\mathbf{T}_{01}^j\right)\cdot\mathbf{u}_G\right]=\mathbf{K}_G^{-1}\cdot\\ \cdot\left[\frac{\partial\mathbf{f}_G}{\partial X_i}-\sum_{j=1}^{ni}\left(\mathbf{T}_{01}^{j\,T}\cdot\mathbf{T}_{LG}^{j\,T}\cdot\frac{\partial\mathbf{K}_L^j}{\partial X_i}\cdot\mathbf{T}_{LG}^j\cdot\mathbf{T}_{01}^j\right)\cdot\mathbf{K}_G^{-1}\cdot\mathbf{u}_G\right]. \quad (12)$$

Relationship between $\mathbf{u}_L^j$ and $\mathbf{u}_G$ will be given by

$$\frac{\partial\mathbf{u}_L^j}{\partial X_i}=\mathbf{T}_{LG}^j\cdot\frac{\partial\mathbf{u}_G^j}{\partial X_i}=\mathbf{T}_{LG}^j\cdot\mathbf{T}_{01}^j\cdot\frac{\partial\mathbf{u}_G}{\partial X_i}=\mathbf{T}_{LG}^j\cdot\mathbf{T}_{01}^j\cdot\mathbf{K}_G^{-1}\cdot\\ \cdot\left[\frac{\partial\mathbf{f}_G}{\partial X_i}-\sum_{j=1}^{ni}\left(\mathbf{T}_{01}^{j\,T}\cdot\mathbf{T}_{LG}^{j\,T}\cdot\frac{\partial\mathbf{K}_L^j}{\partial X_i}\cdot\mathbf{T}_{LG}^j\cdot\mathbf{T}_{01}^j\right)\cdot\mathbf{K}_G^{-1}\cdot\mathbf{f}_G\right]. \quad (13)$$

Substituting (13) into (9), we can obtain the derivation of the $\mathbf{f}_L^j$ with respect to X_i as follows

$$\frac{\partial\mathbf{f}_L^j}{\partial X_i}=\frac{\partial\mathbf{K}_L^j}{\partial X_i}\cdot\mathbf{T}_{LG}^j\cdot\mathbf{T}_{01}^j\cdot\mathbf{K}_G^{-1}\cdot\mathbf{f}_G+\mathbf{K}_L^j\cdot\mathbf{T}_{LG}^j\cdot\mathbf{T}_{01}^j\cdot\mathbf{K}_G^{-1}\cdot\\ \cdot\left[\frac{\partial\mathbf{f}_G}{\partial X_i}-\sum_{j=1}^{ni}\left(\mathbf{T}_{01}^{j\,T}\cdot\mathbf{T}_{LG}^{j\,T}\cdot\frac{\partial\mathbf{K}_L^j}{\partial X_i}\cdot\mathbf{T}_{LG}^j\cdot\mathbf{T}_{01}^j\right)\cdot\mathbf{K}_G^{-1}\cdot\mathbf{f}_G\right]. \quad (14)$$

Finally, after the substituting (14) into (6) we give the gradient of the j-th element stress vector

$$\frac{\partial\boldsymbol{\sigma}_L^j}{\partial X_i}=\frac{\partial\mathbf{C}_L^j}{\partial X_i}\cdot\mathbf{K}_L^j\cdot\mathbf{T}_{LG}^j\cdot\mathbf{T}_{01}^j\cdot\mathbf{K}_G^{-1}\cdot\mathbf{f}_G+\mathbf{C}_L^j\cdot\left\{\frac{\partial\mathbf{K}_L^j}{\partial X_i}\cdot\right.\\ \cdot\mathbf{T}_{LG}^j\cdot\mathbf{T}_{01}^j\cdot\mathbf{K}_G^{-1}\cdot\mathbf{f}_G+\mathbf{K}_L^j\cdot\mathbf{T}_{LG}^j\cdot\mathbf{T}_{01}^j\cdot\mathbf{K}_G^{-1}\cdot\left[\frac{\partial\mathbf{f}_G}{\partial X_i}-\right.\\ \left.\left.-\sum_{j=1}^{ni}\left(\mathbf{T}_{01}^{j\,T}\cdot\mathbf{T}_{LG}^{j\,T}\cdot\frac{\partial\mathbf{K}_L^j}{\partial X_i}\cdot\mathbf{T}_{LG}^j\cdot\mathbf{T}_{01}^j\right)\cdot\mathbf{K}_G^{-1}\cdot\mathbf{f}_G\right]\right\}. \quad (15)$$

It should be noted that the derivation of the matrix $\boldsymbol{C}_j$ with respect to X_i, depends on the used cross-section. To realize the derivation $\frac{\partial\boldsymbol{\sigma}_L^j}{\partial X_i}$ means to find the following derivations $\frac{\partial\mathbf{K}_L^j}{\partial X_i}$, $\frac{\partial\mathbf{C}_L^j}{\partial X_i}$ and $\frac{\partial\mathbf{f}_G}{\partial X_i}$. The last derivation usually equals to zero or is not significant for the sensitivity analysis.

Let the cross-section area be variable X_i then other cross-section characteristics will be expressed as follows

$$J_y=a\cdot X_i^p, J_z=b\cdot X_i^q, J_y=a\cdot X_i^r, \quad (16)$$

where parameters *a, b, c* and exponents *p, q, r* will be obtained exactly (a simple cross-section) or numerically (a more complicated cross section), using the least squares method. The values of these parameters are presented in Tab. 1.

Parameters *a, b, c* and exponents *p, q, r* for chosen cross sections — Tab. 1

Cross-section	$J_y = a \cdot X_i^p$	$J_z = b \cdot X_i^q$	$J_y = a \cdot X_i^r$
Circle 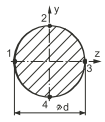	$a = 0.0796$	$b = 0.0796$	$c = 0.1592$
	$p = 2$	$q = 2$	$r = 2$
Square 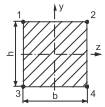	$a = 0.0833$	$b = 0.0833$	$c = 0.14$
	$p = 2$	$q = 2$	$r = 2$
I 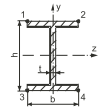	$a = 1.4389$	$b = 0.7947$	$c = 0.0094$
	$p = 2.0401$	$q = 1.7588$	$r = 2.0276$
Box 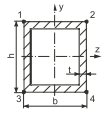	$a = 11.8364$	$b = 13.8364$	$c = 2.7273$
	$p = 1.6047$	$q = 1.6217$	$r = 1.3592$

The derivation $\frac{\partial \mathbf{K}_L^j}{\partial X_i}$ can be given by

$$\frac{\partial \mathbf{K}_L^j}{\partial X_i} = \frac{\delta_{ij}}{X_i} \cdot \left[\mathbf{K}_1^j(X_i) + p \cdot \mathbf{K}_2^j(a \cdot X_i^p) + \right. \\ \left. + q \cdot \mathbf{K}_3^j(b \cdot X_i^q) + r \cdot \mathbf{K}_4^j(c \cdot X_i^r)\right], \tag{17}$$

where δ_{ij} is Kronecker delta and matrices $\mathbf{K}_{1,2,3,4}^j$ are sub-matrices of the stiffness matrix corresponding axial, bending (about axes y and z) and torsion stiffness of the used cross section (More information about stiffness parameters is in [1, 5, 6]).

Let's now focus on the derivation $\frac{\partial \mathbf{C}_L^j}{\partial X_i}$. The transformations matrix $\mathbf{C}_L^j$ depends on coordinates of the marginal points 1, 2, 3, 4, which have to be expressed by the variable X_i. Considering these conditions we can express matrix $\mathbf{C}_L^j$ for circular section as follows

$$\mathbf{C}_L^i = \begin{Bmatrix} 0\ 0\ 0\ 0 & -\frac{4\cdot\sqrt{\pi}}{\sqrt{X_i^3}} & 0 & \frac{1}{X_i}\ 0\ 0\ 0 & 0 & 0 \\ 0\ 0\ 0\ 0 & 0 & \frac{4\cdot\sqrt{\pi}}{\sqrt{X_i^3}} & \frac{1}{X_i}\ 0\ 0\ 0 & 0 & 0 \\ 0\ 0\ 0\ 0 & \frac{4\cdot\sqrt{\pi}}{\sqrt{X_i^3}} & 0 & \frac{1}{X_i}\ 0\ 0\ 0 & 0 & 0 \\ 0\ 0\ 0\ 0 & 0 & -\frac{4\cdot\sqrt{\pi}}{\sqrt{X_i^3}} & \frac{1}{X_i}\ 0\ 0\ 0 & 0 & 0 \\ 0\ 0\ 0\ 0 & 0 & 0 & \frac{1}{X_i}\ 0\ 0\ 0 & -\frac{4\cdot\sqrt{\pi}}{\sqrt{X_i^3}} & 0 \\ 0\ 0\ 0\ 0 & 0 & 0 & \frac{1}{X_i}\ 0\ 0\ 0 & 0 & \frac{4\cdot\sqrt{\pi}}{\sqrt{X_i^3}} \\ 0\ 0\ 0\ 0 & 0 & 0 & \frac{1}{X_i}\ 0\ 0\ 0 & \frac{4\cdot\sqrt{\pi}}{\sqrt{X_i^3}} & 0 \\ 0\ 0\ 0\ 0 & 0 & 0 & \frac{1}{X_i}\ 0\ 0\ 0 & 0 & -\frac{4\cdot\sqrt{\pi}}{\sqrt{X_i^3}} \end{Bmatrix} \tag{18}$$

and the analyzed derivation of this matrix gets the following form

$$\frac{\partial \mathbf{C}_L^i}{\partial X_i} = \begin{Bmatrix} 0\ 0\ 0\ 0 & \frac{6\cdot\sqrt{\pi}}{\sqrt{X_i^5}} & 0 & -\frac{1}{X_i^2}\ 0\ 0\ 0 & 0 & 0 \\ 0\ 0\ 0\ 0 & 0 & -\frac{6\cdot\sqrt{\pi}}{\sqrt{X_i^5}} & -\frac{1}{X_i^2}\ 0\ 0\ 0 & 0 & 0 \\ 0\ 0\ 0\ 0 & -\frac{6\cdot\sqrt{\pi}}{\sqrt{X_i^5}} & 0 & -\frac{1}{X_i^2}\ 0\ 0\ 0 & 0 & 0 \\ 0\ 0\ 0\ 0 & 0 & \frac{6\cdot\sqrt{\pi}}{\sqrt{X_i^5}} & -\frac{1}{X_i^2}\ 0\ 0\ 0 & 0 & 0 \\ 0\ 0\ 0\ 0 & 0 & 0 & -\frac{1}{X_i^2}\ 0\ 0\ 0 & \frac{6\cdot\sqrt{\pi}}{\sqrt{X_i^5}} & 0 \\ 0\ 0\ 0\ 0 & 0 & 0 & -\frac{1}{X_i^2}\ 0\ 0\ 0 & 0 & -\frac{6\cdot\sqrt{\pi}}{\sqrt{X_i^5}} \\ 0\ 0\ 0\ 0 & 0 & 0 & -\frac{1}{X_i^2}\ 0\ 0\ 0 & -\frac{6\cdot\sqrt{\pi}}{\sqrt{X_i^5}} & 0 \\ 0\ 0\ 0\ 0 & 0 & 0 & -\frac{1}{X_i^2}\ 0\ 0\ 0 & 0 & \frac{6\cdot\sqrt{\pi}}{\sqrt{X_i^5}} \end{Bmatrix}. \tag{19}$$

It is possible to get exactly the previous matrices but, for example, $\mathbf{C}_L^j$ of the I-section has to be analyzed numerically [6].

Example 1

Let us consider the structural sensitivity analysis of normal stresses of the beam element from Fig. 2. Given: $E = 2.1e5$ MPa $F_1 = 800$ N, $F_2 = 6000$ N, $A_1 = 200$ mm^2, $A_2 = 35$ mm^2, $L_1 = 1$ m, $L_2 = 0.5$ m.

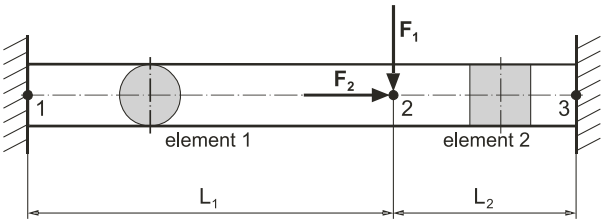

Fig. 2 Simple beam structure with 2 cross section

Applying previous relationships we can obtain the following derivations of matrices $\mathbf{C}_L^1$ and $\mathbf{C}_L^2$

$$\frac{\partial \mathbf{C}_L^1}{\partial X_1} = \begin{Bmatrix} 0 & 0 & 0 & -2.5e-5 & 0 & 0 \\ 0 & 0 & -1.8e-5 & -2.5e-5 & 0 & 0 \\ 0 & 0 & 0 & -2.5e-5 & 0 & 0 \\ 0 & 0 & -1.8e-5 & -2.5e-5 & 0 & 0 \\ 0 & 0 & 0 & -2.5e-5 & 0 & 0 \\ 0 & 0 & 0 & -2.5e-5 & 0 & -1.8e-5 \\ 0 & 0 & 0 & -2.5e-5 & 0 & 0 \\ 0 & 0 & 0 & -2.5e-5 & 0 & -1.8e-5 \end{Bmatrix},$$

$$\frac{\partial \mathbf{C}_L^2}{\partial X_2} = \begin{Bmatrix} 0 & 0 & -3.9e-6 & -8.16e-6 & 0 & 0 \\ 0 & 0 & -3.9e-6 & -8.16e-6 & 0 & 0 \\ 0 & 0 & -3.9e-6 & -8.16e-6 & 0 & 0 \\ 0 & 0 & -3.9e-6 & -8.16e-6 & 0 & 0 \\ 0 & 0 & 0 & -8.16e-6 & 0 & -3.9e-6 \\ 0 & 0 & 0 & -8.16e-6 & 0 & -3.9e-6 \\ 0 & 0 & 0 & -8.16e-6 & 0 & -3.9e-6 \\ 0 & 0 & 0 & -8.16e-6 & 0 & -3.9e-6 \end{Bmatrix}$$

and finally stress gradients in marginal points of the used cross-sections are the following

$$\frac{\partial \sigma_L^{(1)}}{\partial A_1} = \begin{Bmatrix} -0{,}0222 \\ -0{,}8077 \\ -0{,}0222 \\ 0{,}7632 \\ -0{,}0222 \\ -1{,}1897 \\ -0{,}0222 \\ 1{,}1452 \end{Bmatrix} \text{ and } \frac{\partial \sigma_L^{(1)}}{\partial A_1} = \begin{Bmatrix} -0{,}0222 \\ -0{,}8077 \\ -0{,}0222 \\ 0{,}7632 \\ -0{,}0222 \\ -1{,}1897 \\ -0{,}0222 \\ 1{,}1452 \end{Bmatrix} \text{ [MPa/mm}^2\text{]}.$$

The graphic presentation of the stress gradients is in Fig. 3. The presented stress gradient analysis was confronted with a "classical" numerical computational approach ($\Delta\sigma j / \Delta X_i$) and it's possible to observe the absolute consensus.

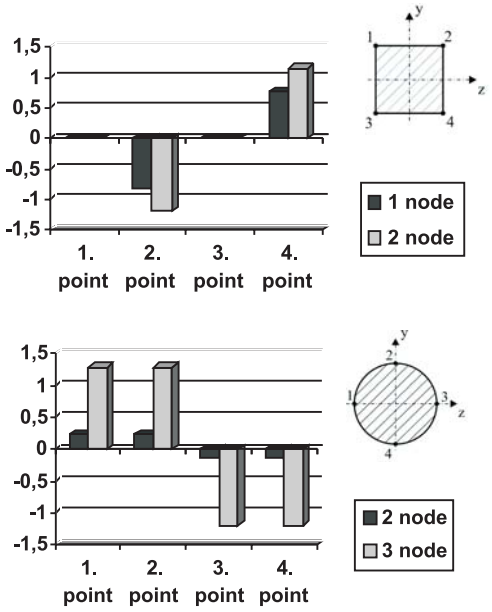

Fig. 3 Values of the stress gradient in the first and second element

3. Stress sensitivity analysis for a thin shell finite element

The finite element modeling of box, shell or thin-walled structures are usually realized using thin shell finite elements (Kirchhoff's or Mindlin's formulation) [1, 4, 9]. The stiffness parameters depend on material constants and element geometry, mainly on its thickness. Therefore, the thickness t_i will be the variable in the following theoretical and numerical stress sensitivity analysis of the shell finite element; the fundamental information about this analysis can be found in [1, 4, 9].

At first we have to prepare the stress calculation process. This process is based on the expression of the *j*-th element membrane forces and bending moments (without shear forces) [4, 6], i.e.

$$\begin{aligned} \left[F_{xx} \;\; F_{yy} \;\; F_{xy}\right]_j^T = \mathbf{F}_m^j = \int_S \mathbf{E}_m^j \cdot \varepsilon_m^j dS_j = \\ = \mathbf{E}_m^j \cdot \int_S \mathbf{B}_m^j dS_j \cdot \mathbf{u}_L^j = t_j \cdot \mathbf{D}_j \cdot \mathbf{I}_m^j \cdot \mathbf{u}_L^j \end{aligned} \tag{20}$$

and

$$\begin{aligned} \left[M_{xx} \;\; M_{yy} \;\; M_{xy}\right]_j^T = \mathbf{M}_b^j = \int_S \mathbf{E}_b^j \cdot \varepsilon_b^j dS_j = \\ = \mathbf{E}_b^j \cdot \int_S \mathbf{B}_b^j dS_j \cdot \mathbf{u}_L^j = \frac{t_j^3}{12} \cdot \mathbf{D}_j \cdot \mathbf{I}_b^j \cdot \mathbf{u}_L^j. \end{aligned} \tag{21}$$

The auxiliary matrices $\mathbf{I}_m$ and $\mathbf{I}_b$ can be calculated only using the numerical approach. Further details about $\mathbf{E}_m$, $\mathbf{E}_b$, $\mathbf{D}$, $\mathbf{B}_m$, $\mathbf{B}_b$, $\mathbf{u}_{el}$ and t are presented in [6]. The extreme stress values can be expected at the top or at the bottom surface. Generally, it means or in compliance with the previous beam element (eq. 5)

$$\begin{bmatrix} \sigma_{mb} \mid_{top} \\ \sigma_{mb} \mid_{bot} \end{bmatrix}^j = \begin{Bmatrix} \sigma_{xx,top} \\ \sigma_{yy,top} \\ \sigma_{xy,top} \\ \sigma_{xx,bot} \\ \sigma_{yy,bot} \\ \sigma_{xy,bot} \end{Bmatrix}^j = \begin{bmatrix} 1/t_j & 0 & 0 & 6/t_j^2 & 0 & 0 \\ 0 & 1/t_j & 0 & 0 & 6/t_j^2 & 0 \\ 0 & 0 & 1/t_j & 0 & 0 & 6/t_j^2 \\ 1/t_j & 0 & 0 & 6/t_j^2 & 0 & 0 \\ 0 & 1/t_j & 0 & 0 & 6/t_j^2 & 0 \\ 0 & 0 & 1/t_j & 0 & 0 & 6/t_j^2 \end{bmatrix} \cdot \begin{Bmatrix} F_{xx} \\ F_{yy} \\ F_{xy} \\ M_{xx} \\ M_{yy} \\ M_{xy} \end{Bmatrix} = \begin{bmatrix} \mathbf{A}_{t,top} \\ \mathbf{A}_{t,bot} \end{bmatrix}^j \cdot \begin{Bmatrix} \mathbf{F}_m \\ \mathbf{M}_b \end{Bmatrix}^j, \tag{22}$$

$$\boldsymbol{\sigma}^{j}_{mb\_L} = \mathbf{C}^{j}_{L} \cdot \mathbf{f}^{j}_{L}. \tag{23}$$

Let's build new material and auxiliary matrices

$$\mathbf{E}_{mb} = \begin{bmatrix} t_j \cdot \mathbf{I}_3 & 0_3 \\ 0_3 & \dfrac{t_j^3}{12} \cdot \mathbf{I}_3 \end{bmatrix} \cdot \begin{Bmatrix} \mathbf{D} \\ \mathbf{D} \end{Bmatrix}_j = \mathbf{D}_t \cdot \mathbf{D}_{mb}, \; \mathbf{I}_{mb} = \begin{Bmatrix} \mathbf{I}^j_m \\ \mathbf{I}^j_b \end{Bmatrix}, \tag{24}$$

where the matrix $\mathbf{I}_3$ is the classical unit matrix. Then (22) can be written as follows

$$\boldsymbol{\sigma}_{j\_mb}\big|_{top} = \mathbf{A}_{t,top} \cdot \mathbf{E}_{mb} \cdot \mathbf{I}_{mb} \cdot \mathbf{u}^j_L = \mathbf{A}_{t,top} \cdot \mathbf{D}_t \cdot \mathbf{D}_{mb} \cdot \mathbf{I}_{mb} \cdot \mathbf{u}^j_L, \tag{25a}$$

$$\boldsymbol{\sigma}_{j\_mb}\big|_{bot} = \mathbf{A}_{t,bot} \cdot \mathbf{E}_{mb} \cdot \mathbf{I}_{mb} \cdot \mathbf{u}^j_L = \mathbf{A}_{t,bot} \cdot \mathbf{D}_t \cdot \mathbf{D}_{mb} \cdot \mathbf{I}_{mb} \cdot \mathbf{u}^j_L. \tag{25b}$$

Generally, the top or bottom von Mises stresses may be calculated from relations

$$\sigma^2_{j\_ekv}\big|_{top} = \boldsymbol{\sigma}^T_{j\_mb}\big|_{top} \cdot \mathbf{T}_{mb} \cdot \boldsymbol{\sigma}_{j\_mb}\big|_{top}$$

or

$$\sigma^2_{j\_ekv}\big|_{bot} = \boldsymbol{\sigma}^T_{j\_mb}\big|_{bot} \cdot \mathbf{T}_{mb} \cdot \boldsymbol{\sigma}_{j\_mb}\big|_{bot} \tag{26}$$

where

$$T_{mb} = \begin{bmatrix} 1 & -0.5 & 0 \\ -0.5 & 1 & 0 \\ 0 & 0 & 3 \end{bmatrix}. \tag{27}$$

Using (25) and (27) in (26) we obtain

$$\boldsymbol{\sigma}^2_{j\_ekv}\big|_{top} = \boldsymbol{\sigma}^T_{j\_mb}\big|_{top} \cdot \mathbf{T}_{mb} \cdot \boldsymbol{\sigma}_{j\_mb}\big|_{top} =$$

$$= \mathbf{u}^{jT}_L \cdot \mathbf{I}^T_{mb} \cdot \mathbf{D}^T_{mb} \cdot \mathbf{D}^T_t \cdot \mathbf{A}^T_{t,top} \cdot \mathbf{T}_{mb} \cdot \mathbf{A}_{t,top} \cdot \mathbf{D}_t \cdot \mathbf{D}_{mb} \cdot \mathbf{I}_{mb} \cdot \mathbf{u}^j_L = \tag{28a}$$

$$= \mathbf{u}^{jT}_L \cdot \mathbf{I}^T_{mb} \cdot \mathbf{D}^T_{mb} \cdot \mathbf{D}_{mb} \cdot \mathbf{I}_{mb} \cdot \mathbf{u}^j_L$$

and

$$\sigma^2_{j\_ekv}\big|_{bot} = \boldsymbol{\sigma}^T_{j\_mb}\big|_{bot} \cdot \mathbf{T}_{mb} \cdot \boldsymbol{\sigma}_{j\_mb}\big|_{bot} =$$

$$= \mathbf{u}^{jT}_L \cdot \mathbf{I}^T_{mb} \cdot \mathbf{D}^T_{mb} \cdot \mathbf{D}^T_t \cdot \mathbf{A}^T_{t,bot} \cdot \mathbf{T}_{mb} \cdot \mathbf{A}_{t,bot} \cdot \mathbf{D}_t \cdot \mathbf{D}_{mb} \cdot \mathbf{I}_{mb} \cdot \mathbf{u}^j_L = \tag{28b}$$

$$= \mathbf{u}^{jT}_L \cdot \mathbf{I}^T_{mb} \cdot \mathbf{D}^T_{mb} \cdot \mathbf{D}_{mb} \cdot \mathbf{I}_{mb} \cdot \mathbf{u}^j_L$$

where

Assuming a relation between the local element displacements $\mathbf{u}^j_L$ and the global displacement vector $\mathbf{u}_G$

$$\mathbf{u}^j_L = \mathbf{T}_{LG} \cdot \mathbf{T}_{01} \cdot \mathbf{u}_G, \tag{30}$$

then (28a,b) may be rewritten as

$$\sigma^2_{j\_ekv}\big|_{top} = \mathbf{u}^T_G \cdot \mathbf{T}^T_{01} \cdot \mathbf{T}^T_{LG} \cdot \mathbf{I}^T_{mb} \cdot \mathbf{D}^T_{mb} \cdot \mathbf{T}_{t,top} \cdot \mathbf{D}_{mb} \cdot \cdot \mathbf{I}_{mb} \cdot \mathbf{T}_{LG} \cdot \mathbf{T}_{01} \cdot \mathbf{u}_G, \tag{31a}$$

and

$$\sigma^2_{j\_ekv}\big|_{bot} = \mathbf{u}^T_G \cdot \mathbf{T}^T_{01} \cdot \mathbf{T}^T_{LG} \cdot \mathbf{I}^T_{mb} \cdot \mathbf{D}^T_{mb} \cdot \mathbf{T}_{t,bot} \cdot \mathbf{D}_{mb} \cdot \cdot \mathbf{I}_{mb} \cdot \mathbf{T}_{LG} \cdot \mathbf{T}_{01} \cdot \mathbf{u}_G \tag{31b}$$

where $\mathbf{T}_{LG}$ is a classical transformation matrix between the local and the global coordinate systems, $\mathbf{T}_{01}$ is again a Boolean matrix, i.e. the localization matrix determining the element position in the global stiffness matrix.

The stress sensitivity analysis means the finding of von Mises stress derivative with respect to a chosen structural parameter, in our case the element thickness *t*. Let's analyze the differentiation of von Mises stress of *j*-th element with respect to the *i*-th element thickness t_i. Applying (31a, b) we can obtain

$$\frac{\partial \sigma^2_{j\_ekv}\big|_{top}}{\partial t_i} = \frac{\partial \mathbf{u}^T}{\partial t_i} \cdot \mathbf{T}^T_{j\_01} \cdot \mathbf{T}^T_{j\_LG} \cdot \mathbf{I}^T_{j\_mb} \cdot \mathbf{D}^T_{j\_mb} \cdot \mathbf{T}_{j\_t,top} \cdot \cdot \mathbf{D}_{j\_mb} \cdot \mathbf{I}_{j\_mb} \cdot \mathbf{T}_{vLG} \cdot \mathbf{T}_{j\_01} \cdot \mathbf{u} + \mathbf{u}^T \cdot \mathbf{T}^T_{j\_01} \cdot \mathbf{T}^T_{j\_LG} \cdot \mathbf{I}^T_{j\_mb} \cdot \cdot \mathbf{D}^T_{j\_mb} \cdot \delta_{ij} \cdot \frac{\partial \mathbf{T}_{j\_t,top}}{\partial t_i} \cdot D_{j\_mb} \cdot \mathbf{I}_{j\_mb} \cdot \mathbf{T}_{j\_LG} \cdot \mathbf{T}_{j\_01} \cdot \mathbf{u} + \tag{32a}$$

$$+ \mathbf{u}^T \cdot \mathbf{T}^T_{j\_01} \cdot \mathbf{T}^T_{j\_LG} \cdot \mathbf{I}^T_{j\_mb} \cdot \mathbf{D}^T_{j\_mb} \cdot \mathbf{T}_{j\_t,top} \cdot \mathbf{D}_{j\_mb} \cdot \mathbf{I}_{j\_mb} \cdot \cdot \mathbf{T}_{j\_LG} \cdot \mathbf{T}_{j\_01} \cdot \frac{\partial \mathbf{u}}{\partial t_i},$$

$$T_{t,top} = \begin{bmatrix} 1 & -0.5 & 0 & 0.5 \cdot t_j & -0.25 \cdot t_j & 0 \\ -0.5 & 1 & 0 & -0.25 \cdot t_j & 0.5 \cdot t_j & 0 \\ 0 & 0 & 3 & 0 & 0 & 1.5 \cdot t_j \\ 0.5 \cdot t_j & -0.25 \cdot t_j & 0 & 0.25 \cdot t_j^2 & -0.125 \cdot t_j^2 & 0 \\ -0.25 \cdot t_j & 0.5 \cdot t_j & 0 & -0.125 \cdot t_j^2 & 0.25 \cdot t^2 & 0 \\ 0 & 0 & 1.5 \cdot t_j & 0 & 0 & 0.75 \cdot t_j^2 \end{bmatrix} \tag{29a}$$

and

$$T_{t,bot} = \begin{bmatrix} 1 & -0.5 & 0 & -0.5 \cdot t_j & 0.25 \cdot t_j & 0 \\ -0.5 & 1 & 0 & 0.25 \cdot t_j & -0.5 \cdot t_j & 0 \\ 0 & 0 & 3 & 0 & 0 & -1.5 \cdot t_j \\ -0.5 \cdot t_j & 0.25 \cdot t_j & 0 & 0.25 \cdot t_j^2 & -0.125 \cdot t_j^2 & 0 \\ 0.25 \cdot t_j & -0.5 \cdot t_j & 0 & -0.125 \cdot t_j^2 & 0.25 \cdot t_j^2 & 0 \\ 0 & 0 & -1.5 \cdot t_j & 0 & 0 & 0.75 \cdot t_j^2 \end{bmatrix} \tag{29b}$$

$$\frac{\partial \sigma^2_{j\_ekv}\,|_{\,bot}}{\partial t_i} = \frac{\partial \mathbf{u}^T}{\partial t_i}\cdot \mathbf{T}^T_{j\_01}\cdot \mathbf{T}^T_{j\_LG}\cdot \mathbf{I}^T_{j\_mb}\cdot \mathbf{D}^T_{j\_mb}\cdot \mathbf{T}_{j\_t,bot}\cdot$$
$$\cdot \mathbf{D}_{j\_mb}\cdot \mathbf{I}_{j\_mb}\cdot \mathbf{T}_{vLG}\cdot \mathbf{T}_{j\_01}\cdot \mathbf{u} + \mathbf{u}^T\cdot \mathbf{T}^T_{j\_01}\cdot \mathbf{T}^T_{j\_LG}\cdot \mathbf{I}^T_{j\_mb}\cdot$$

$$\cdot \mathbf{D}^T_{j\_mb}\cdot \delta_{ij}\cdot \frac{\partial \mathbf{T}_{j\_t,bot}}{\partial t_i}\cdot D_{j\_mb}\cdot \mathbf{I}_{j\_mb}\cdot \mathbf{T}_{j\_LG}\cdot \mathbf{T}_{j\_01}\cdot \mathbf{u} + \quad , \text{(32b)}$$
$$+ \mathbf{u}^T\cdot \mathbf{T}^T_{j\_01}\cdot \mathbf{T}^T_{j\_LG}\cdot \mathbf{I}^T_{j\_mb}\cdot \mathbf{D}^T_{j\_mb}\cdot \mathbf{T}_{j\_t,bot}\cdot \mathbf{D}_{j\_mb}\cdot \mathbf{I}_{j\_mb}\cdot$$

$$\cdot \mathbf{T}_{j\_LG}\cdot \mathbf{T}_{j\_01}\cdot \frac{\partial \mathbf{u}}{\partial t_i},$$

where

$$\frac{\partial \sigma^2_{j\_ekv}\,|_{\,top}}{\partial t_i} = \frac{1}{2\sigma_{j\_ekv}\,|_{\,top}}\cdot \frac{\partial \sigma^2_{j\_ekv}\,|_{\,top}}{\partial t_i} \quad \text{and}$$

$$\frac{\partial \sigma_{j\_ekv}\,|_{\,bot}}{\partial t_i} = \frac{1}{2\sigma_{j\_ekv}\,|_{\,bot}}\cdot \frac{\partial \sigma^2_{j\_ekv}\,|_{\,bot}}{\partial t_i}. \qquad (37)$$

All the presented approaches have been implemented into Matlab's FE software MATFEM developed by the authors.

Example 2

Determine the element stress derivative (eqs. 32a, 32b) with respect to the thickness t_1 and t_2 of the shell structure in Fig. 4.

$$\frac{\partial \mathbf{T}_{j\_t,top}}{\partial t_i} = \delta_{ij}\cdot \begin{bmatrix} 0 & 0 & 0 & 0.5 & -0.25 & 0 \\ 0 & 0 & 0 & -0.25 & 0.5 & 0 \\ 0 & 0 & 0 & 0 & 0 & 1.5 \\ 0.5 & -0.25 & 0 & 0.5\cdot t_j & -0.25\cdot t_j & 0 \\ -0.25 & 0.5 & 0 & -0.25\cdot t_j & 0.5\cdot t_j & 0 \\ 0 & 0 & 1{,}5 & 0 & 0 & 1.5\cdot t_j \end{bmatrix} \qquad (33a)$$

and

$$\frac{\partial \mathbf{T}_{j\_t,bot}}{\partial t_i} = \delta_{ij}\cdot \begin{bmatrix} 0 & 0 & 0 & -0{,}5 & 0{,}25 & 0 \\ 0 & 0 & 0 & 0{,}25 & -0{,}5 & 0 \\ 0 & 0 & 0 & 0 & 0 & -1{,}5 \\ -0{,}5 & 0{,}25 & 0 & 0{,}5\cdot t_j & -0{,}25\cdot t_j & 0 \\ 0{,}25 & -0{,}5 & 0 & -0{,}25\cdot t_j & 0{,}5\cdot t_j & 0 \\ 0 & 0 & -1{,}5 & 0 & 0 & 1{,}5\cdot t_j \end{bmatrix} \qquad (33a)$$

The derivative u with respect to ti may be expressed as

$$\frac{\partial \mathbf{u}_G}{\partial t_i} = \mathbf{K}_G^{-1}\cdot\left(\frac{\partial \mathbf{f}}{\partial t_i} - \frac{\partial \mathbf{K}_G}{\partial t_i}\cdot \mathbf{u}_G\right) \qquad (34)$$

or, in more detail,

$$\frac{\partial \mathbf{u}_G}{\partial t_i} = \mathbf{K}_G^{-1}\cdot\left[\frac{\partial \mathbf{f}}{\partial t_i} - \left(\sum_{j=1}^{n}\mathbf{T}^T_{j\_01}\cdot \mathbf{T}^T_{j\_LG}\cdot \frac{\partial\left(\mathbf{K}_{j\_m} + \mathbf{K}_{j\_b} + \mathbf{K}_{j\_s}\right)}{\partial t_i}\cdot \mathbf{T}_{j\_LG}\cdot \mathbf{T}_{j\_01}\right)\cdot \mathbf{u}_G\right]. \qquad (35)$$

The relation $\frac{\partial \mathbf{f}}{\partial t_i}$ is often zero and the derivative of the all the element components of the stiffness matrix can be realized as follows [6]

$$\frac{\partial\left(\mathbf{K}_{j\_m} + \mathbf{K}_{j\_b} + \mathbf{K}_{j\_s}\right)}{\partial t_i} = \frac{\delta_{ij}}{t_i}\cdot\left(\mathbf{K}_{j\_m} + 3\cdot \mathbf{K}_{j\_b} + \mathbf{K}_{j\_s}\right). \qquad (36)$$

The particular membrane, bending and shear matrices are presented in [1, 7].

Finally, the derivative of the von Mises stress (at the top and at the bottom surfaces) with respect to the element thickness t_i is the following

Let's consider the following input parameters: elasticity modulus E = 3.106 MPa, Poisson's ratio μ = 0.3, thicknesses t_1 = 3 mm and t_2 = 2 mm and force F_Z = 2500 N concentrated into each node of the top curved surface.

Stress gradient values for the chosen elements – analytical vs. numerical calculation — Tab. 2

Nr. of element	Stress gradient with respect t_1		Nr. of element	Stress gradient with respect t_2	
	Analytically	Numerically		Analytically	Numerically
4	180.6925	180.8217	81	72.1432	72.1356
15	178.1929	178.3464	66	56.8617	56.8841
12	172.7673	172.9401	65	56.5136	56.5514
7	172.2105	172.3427	92	54.8065	54.8449
53	170.2041	170.4455	80	52.5394	52.5649

The chosen calculated values of the stress gradients are written in Table 2. The presented analytic stress gradient calculation was confronted with the classical numerical computational approach ($\Delta\sigma_j/\Delta t_i$). A graphic presentation of the stress gradients distribution in each of the elements is in Figs. 5 and 6.

The results document the influence of both parameters on the stresses and the major signification of thickness t_1. This information may be used for the next optimizing process.

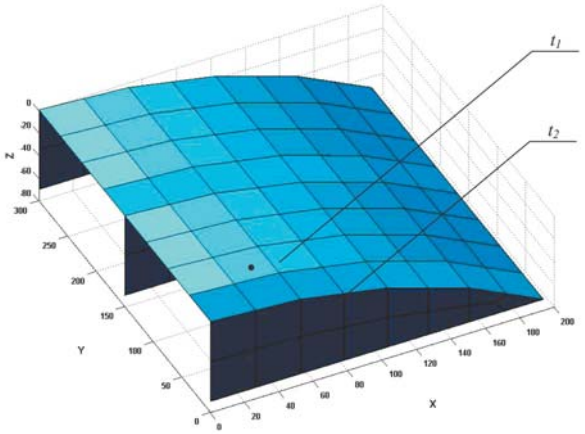

Fig. 4 Half model of the analysed shell structure in MATFEM

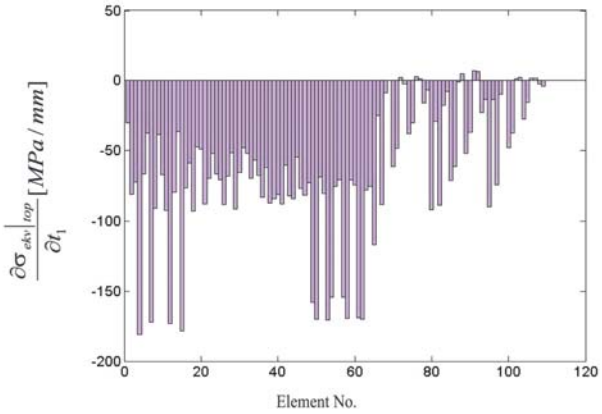

Fig. 5 Stress sensitivity with respect to t_1

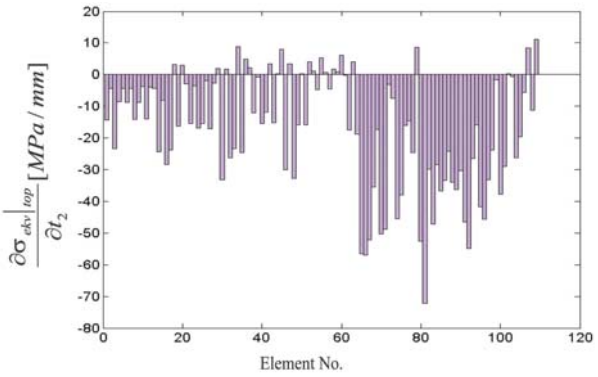

Fig. 6 Stress sensitivity with respect to t_2

4. Conclusion

The presented work deals with the theoretical aspects and numerical realization of the stress sensitivity analysis of the beam and shell finite elements focused on its cross section parameters (the area in the case of the beam element and the thickness in the case of the thin shell element). The whole computational procedure was inbuilt into Matlab's software module MATFEM. Testing examples support the authors' considerations about effectiveness of the proposed method.

Acknowledgements

This work has been supported by VEGA grant No. 1/4099/07 and by the research project AV 4/2044/08.

References

[1] BATHE , K. J.: *Finite Element Procedures.* New Persey, Prentice Hall, 1996.
[2] DEKÝŠ, V., SAPIETOVÁ, A., KOCÚR, R.: *On the reliability estimation of the conveyer mechanism using the Monte Carlo method,* Proc. of COSIM2006, Krynica-Zdroj, 2006, pp. 67–74.
[3] HAFTKA, R. T., GURDAL, Z.: *Elements of Structural Optimization*, Kluwer Academic Publisher, 1992.
[4] KWON, Y. W., BANG, H.: *The Finite Element Method using MATLAB,* CRC Press University of Minnesota, 1996.
[5] MURIN, J.: *Finite Element Method for Bar Constructions and Framed Structures (in Slovak)*, STU, Bratislava 1999.
[6] SAGA, M., VASKO, M., KOCUR, R., TOTH, L., KOHAR, R.: *Application of optimizing algorithms in solid mechanics.* In Slovak, VTS, University of Zilina, 2006.
[7] M. SAGA A , M. VAAKO A, J. JANDACKA, Z. HOLKOVA: *Contribution to stress sensitivity analysis,of the shell finite elements,* Applied and Computational Mechanics, Vol. II, No.1, 2008, pp. 113–122

[8] SEGLA, S., CIUPITU, L., REICH, S.: *Optimization of a spring balancing mechanism for parallelogram robot mechanisms,* 1st International Conference "Optimization of robots and Manipulators OPTIROB 2006", Predeal, Romania, 2006, pp. 69–74.
[9] VAVRO, J.: *Optimization of the design of cross-sectional quantities in transport machines and equipment,* Studia i materially, Zelena Hora, Poland, 1998, pp. 186–194.
[10] ZIENKIEWICZ, O. C.: *The Finite Element Method in Engineering Science,* McGraw, Hill, New York, 1971.

Milan Zmindak – Pavol Novak *

PARTICLES INTERACTIONS IN COMPOSITES REINFORCED BY FIBRE AND SPHERICAL INCLUSIONS

In our contribution we will show a new Method of Continuous Source Functions (MCSF) to modelling of such problems like composites reinforced by finite length fibres with a large aspect ratio and composites reinforced by spherical inclusions. The source functions (forces and dipoles) are continuously distributed along the fibre axis (i. e. outside of the domain, which is the domain of the matrix) and their intensities are modelled by 1D quadratic elements along the axis in order to satisfy continuity conditions between the matrix and fibre. The spherical inclusions are modelled by a triple dipole located in the centre of the particle and the intensities of the dipole can be computed using a small number of collocation points on the particle boundary

Keywords: elastic reinforced composites, meshless method, method of continuous source functions

1. Introduction

Composite materials reinforced by stiff particles or fibres are important materials possessing excellent mechanical and also thermal and electro-magnetic properties. Such composites contain huge number of reinforcing elements with large gradients in all fields in small parts of the matrix (in micro scale) around the reinforcing elements and accurate computational models are important for homogenization of material properties in macro scale (adjustment of local stiffness of such material) and for evaluation of material strength.

Mechanical behaviour of composites under loading is extremely complex and can only be understood if the observed behaviour is interpreted in terms of micro-mechanical or macro-mechanical analyses. The fibres can be in form of cylinders or with hemispheres in the tips. The tips cause large gradient in all displacement, strain and stress fields not only in a close distance to the fibre, but also in a relatively far distance perpendicular to the axis of the fibre. It is very important to accurately satisfy the continuity conditions in the tips of the fibre. Correct simulation of these fields is important for simulation of interaction of fibres and for evaluation of stiffening effect. Mechanical properties and possible failure modes of these composites can be predicted early during the design stage using modelling techniques [1].

A suitable method for solution of the above problems is a multi-region approach that often leads to inaccurate results, particularly, when there is a large difference between the material properties of the matrix and that of the fibre resulting in coefficients in the system matrix differing by orders of magnitude. However, with a relatively large number of fibres in a given problem, this type of approach is not very feasible because a very large amount of computing resources as well as substantial modelling efforts are necessary. It is well known that using a volume element approximation such as FEM, hundreds or thousands of elements are necessary to achieve a required accuracy even for a simple problem.

The classical Eshelby solution [2] was obtained for an elastic isotropic inclusion in an infinite elastic matrix. The treatment of the RVE as an infinite space implies that the inclusion concentration is diluted and, therefore, a direct application of these results to the case of finite inclusion concentration is only approximate. An improved model was suggested by Mori and Tanaka [3]. Their method also assumes the absence of all inhomogenities, but it includes a certain effect of inhomogeneity by taking an average strain in the matrix phase when all the inhomogenities are present. Recently, Sauer [4] solved the elastic field of an idealized, spherical, finite RVE embedded in an infinite, homogeneous, isotropic medium using Boundary Integral Equations (BIE). A solution is found which satisfies the continuity of displacements and traction fields across the RVE/composite interface. However, the model is simplified and does not take into account the interaction of discretely distributed particles in the matrix and calculates the Eshelby tensor from simplified Dirichlet and Neumann boundary conditions.

In our presentation we will use the method of continuous source functions (MCSF) and will show how the Trefftz Radial Basis Functions (TRBF), i. e. RBF satisfying the governing equations (which can be the fundamental solutions, or more general functions, dipoles, dislocations, etc.) can be used to increase the efficiency of simulations. The most efficient methods will be those which will best approximate both domain variables and boundary

* **Milan Zmindak, Pavol Novak**
Department of Applied Mechanics, Slovakia, Faculty of Mechanical Engineering, University of Zilina
Email: Milan.Zmindak@fstroj.uniza.sk

conditions. The TRBF are source functions having their source points outside the domain. Special attention will be given to the application of the TRBF in the form of dipoles to the simulation of composites reinforced by particles and/or short fibres.

Compared to the Method of Fundamental Solutions (MFS) [5, 6] which does not require any integration, the MCSF requires an integration along 1D and 2D element. The integrals are quasi-singular and quasi-hyper-singular and the numerical integration is computationally cumbersome and inefficient. The analytic integration using a symbolic manipulation is a very efficient tool used in the models. A relatively small number (usually fewer than 10) of elements in a fibre is necessary to obtain a good accuracy also by a large aspect ratio (e.g. 1:100).

The proposed method is not fully meshless for these particular models as it requires 1D elements outside the 3D matrix domain, however, the model presents a significant reduction (even by several orders) of the resulting system of equations comparing to FEM, BEM, or other known meshless methods and can be qualified as a Mesh Reducing Method (MRM).

2. Solution method

The boundary integral equation for analysis of elastic domain containing rigid inclusions is used

$$\int_L K(x_s, x_f)\, f(x_s) dx_s = g(x_f) \tag{1}$$

where K is the kernel function for force intensity or dipole intensity along the fibre, g is a boundary condition on the fibre surface. A lower index s denotes the source point where force is acting and f is the field point where the displacement is introduced. Kernel function is represented by kernel functions for displacement and traction components in the fundamental solution (Kelvin´s solution) respectively, which can be found in Appendix A. For fibre reinforced composites the source functions (forces and dipoles) are continuously distributed along the fibre axis (i. e. outside of the domain which is the domain of the matrix) and their intensities are modelled by 1D quadratic elements along the axis in order to satisfy continuity conditions between the matrix and fibre. A 2D distribution of source functions is selected in the parts of the fibres where large gradients appear.

The RBF can be used also for simulation of the interaction between the matrix and particles with a very large aspect ratio such as composites reinforced with short fibres where the aspect ratio can be 1000:1 or even larger. The inter-domain boundary conditions can be simulated by 1D distribution of the TRBF's (source functions) along the fibre axis. When the TRBF's are approximated by polynomials then the problems lead to evaluation of the following integrals

$$\int_a^b \frac{x_s^n (x_s - x_f)^p}{\left(y^2 + x_s - x_f^2\right)^{\frac{m}{2}+r}} dx_s = f(x_f) \tag{2}$$

where x is the coordinate along the fibre axis, the subscripts s and f denote the source and field point and exponents are integer numbers and y is the distance of the field point from the source point. For computational purpose the integral (2) is transformed to

$$\int_{a+x_f}^{b+x_f} \frac{(x - x_f)^n x^p}{\left(y^2 + x^2\right)^{\frac{m}{2}+r}} dx = f(x_f) \tag{3}$$

The numerical integration of such integrals would be computationally very laborious because of the quasi-singularities and quasi-hyper-singularities in the integrals; however, analytic evaluation of the integrals containing the kernel function and polynomial approximation of the unknown function is a very elegant way of numerical evaluation of the integrals, if the axis of the fibre is straight, i.e. the value of y is constant in the integrals above.

If the ideas of the TRBF and MFS are used then a simple and efficient formulation can be developed. In the case of composite material reinforced by spheres or particles with an aspect ratio not very different from 1, a particle can be modelled by a triple dipole located in the centre of the particle and the intensities of the dipole can be computed by using a small number of collocation points on the particle boundary (Fig.1). The method of discrete dipoles is very simple and details can be found in [7].

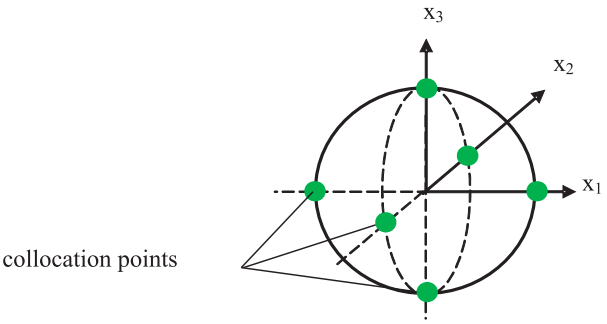

Fig. 1. Spherical inclusion and collocation points

Because of the large aspect ratio, continuity of strains between a matrix and a fibre can be simulated by continuously distributed

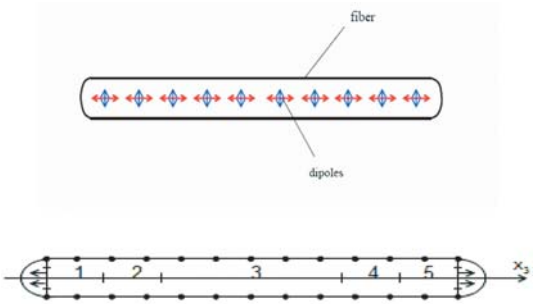

Fig.2 Continuous force/dipole model for the fibre reinforcing element

source functions (forces, dipoles, dislocations, etc. [8, 9] as they are known from the potential theory) along the fibre axis (Fig. 2). The continuous source functions enable to simulate the continuity conditions with much reduced collocation points along the fibre boundary.

3. Some Applications and Results

Example 1: Short- Fibre-Reinforced Composites

First example simulates the interaction of fibres with the matrix and also the interaction of fibres: 1) a patch of non-overlaying rows of fibres as shown in Fig. 3 on the left and 2) a patch of overlaying rows of fibres according to Fig. 3 on the right. In the examples the modulus of elasticity of the matrix was $E = 1000$ and Poisson ratio $\nu = 0.3$. The matrix was reinforced by a patch of straight rigid cylindrical fibres. The length of fibres was $L = 100$ and $L = 1000$ and the radius $R = 1$. The distance between fibres was $\Delta 1 = \Delta 2 = \Delta 3 = 16$ and for longer fibres also $\Delta 3 = 200$ in the fibre direction. The fibres in the patch contain approximately 1 % of the volume of the composite material. The domain is supposed to be loaded by far field stress $\sigma_{33\infty} = 10$ in the direction (x_3), which is also parallel to fibres' axes. The model of the fibre used in these examples contained fewer than 100 unknown parameters (intensities of the source functions) and about 200 collocation points. The problem is solved by the least square (LS) method. The variation of forces for longer fibres is given in Fig. 4.

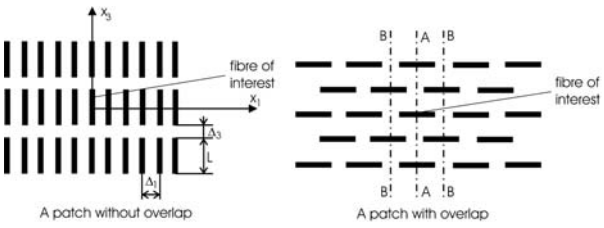

Fig. 3. 3D patches of regularly distributed fibres

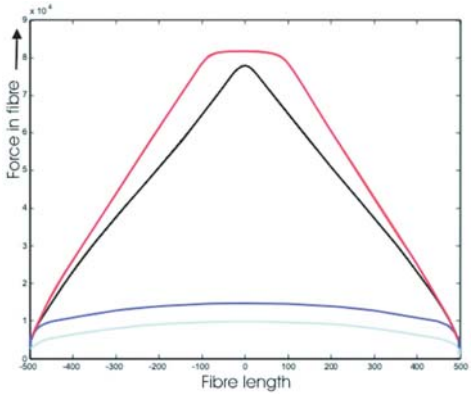

Fig. 4. Forces in fibre cross section with overlap red and black and without overlap cyan and blue by different gap between fibres in longitudinal direction

As the fibres are long and thin, they are much stiffer in the axial direction than in bending and the satisfaction of continuity of displacements, strains and tractions on the surface between the matrix and fibres and corresponding displacements and strains along the fibre would require a very large number of TRBF (source points) to simulate the interaction.

Moreover, in the end parts of a fibre the fields have very large gradients, which increases the difficulties with accuracy and numerical stability of the solution. In our models a continuous distribution of the source points is used for simulation of the interaction. It is possible to use both distributed forces and distributed dipoles along the fibre axis (1D distribution) and oriented in the axis direction in the model. Their role is mainly to satisfy continuity in the fibre axis direction. Continuity in directions perpendicular to the fibre axis is served mainly by the continuous dipoles along the fibre axis, but directed perpendicularly to the fibre axis. Recall that continuously distributed dipoles are derivatives of continuously distributed forces. The distribution is approximated by piecewise quadratic functions with C^0 continuity between the elements. More about the model can be found in [10].

The forces in the fibres are much greater if the fibres overlap then in the fibres without the overlap (Fig. 4) and thus the stiffening effect is considerably influenced by the overlapping. The forces can lead to axial stresses which can exceed the stresses in the matrix by several orders and can cause fracture of the fibres in tension or loss of stability in compression.

Extreme shear forces between the fibre and the matrix can lead to de-bonding of the fibre or to de-cohesion and re-cohesion at the ends and also in the middle of a fibre close to another fibre in materials reinforced with nanotubes, which are typical and very efficient novel reinforcing materials. Note that the large gradients in shear stresses arise not only at the ends of fibres but also in the parts perpendicular to the ends of neighbour fibres and the models are very sensitive to 1D distribution functions along the fibre axis and can cause numerical errors [11].

Example 2: A Rigid Sphere in Elastic Medium

In this example composite material is reinforced by spheres or particles with an aspect ratio not very different from 1. The particle is modelled by a triple dipole located in the centre of the particle and the intensities of the dipole can be computed by using a small number of collocation points on the particle boundary. The interaction of 2 particles modelled by two triple dipoles in their centres and using only 6 collocation points on the particle boundaries in an eigenstrain field is shown in the next figures. Deformation, radial and tangential components of tractions are given as computed from the simplified models for radius of smaller particle equal to one fifth of the radius of a larger one and with the distance between particles equal to one fifth of the radius of the smaller particle (Figs. 5a- d). The undeformed form of particles is red and the green and blue are corresponding fields for a corresponding particle. Intensity of tractions is given by radial distance of the corresponding circle from the undeformed form. Recall

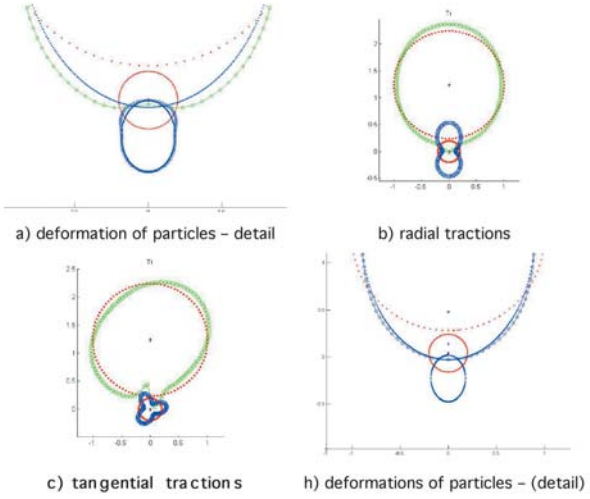

Fig. 5. Interaction of two different size inclusions

that for the deformed form of a spherical particle in the eigenstrain [12] only local parts of deformation and tractions are shown in the figures, i.e. if the particle is rigid the local deformation of sphere should follow the blue lines in the corresponding Figs. 5. The traction components are shown in different scales and tangential components are much smaller than radial ones. It can be seen that the simple models are sufficient for the problems when the size of particles is not very different and particles are not very close to each other. Refined models are required for small parts of models. However, this simple model can be used for iterative improvements of solution with very fast convergence in iterative steps for each very stiff or elastic inclusions. Additional interpolation functions are included in the iterative steps.

4. Conclusion

TRBF are shown to be very efficient interpolation functions, which satisfy governing equations inside the domain but they can also satisfy boundary conditions in some part of the domain boundary. The TRBF can be introduced by the fundamental solution (unit force acting on infinite continuum), its derivatives (dipoles, couples, dislocations) in mechanics, thermal, or other source functions in other field problems. The TRBF correctly simulate the decay of field variables and so they can efficiently model any concentrators in field variables. They can be also source functions acting in other domains (Boussinesq-Cerutti solution for half space which can be used for effective modeling of effect of local loading [13, 14], analytic solution for layered structures, etc.).

It is demonstrated that the TRBF can be used in connection with boundary collocation methods to simulate a microstructure reinforced by particles using ideas similar to MFS with only single triple dipoles located into centres of the particles to simulate the interaction of particles with matrix and with other particles, as well. No meshing and no integration are necessary. The ideas of Fast Multipole Method (FMM) are also possible to formulate using mechanical principles instead of Taylor series expansions by the formulations. The far field interaction is then introduced by resulting dipole taking into account the force and moment equilibrium.

For simulation of a microstructure reinforced with short fibres 1D continuous distribution (it is the TRBF, too) of source functions was developed by the authors. It can reduce the model comparing to other numerical models by many orders. The forces or dipoles can be used for simulation of interdomain continuity in a fibre axis direction and continuous dipoles in perpendicular directions. The models can be further augmented to simulate composites reinforced by imperfect or curved fibres by using a continuous distribution of couples along the fibre axis in order to keep the moment equilibrium of the fibre reinforcing effect. In this way the fibres with a large aspect ratio like carbon nanotubes (CNT) which are very stiff in the fibre axis direction, but much more flexible in bending can be correctly simulated for interaction with the matrix and with other fibres, too. The examples show how important the correct simulation of all interactions is for a global behaviour assessment.

Numerical models can take into account different topologies (size and distribution of particles) of composite, different materials of each particle and can be a part of multiscale computational models. The reinforcing particles can be on the surface only and they can form surface layers. From the computational point of view the models can define the Functionally Graded Material (FGM) from microstructural changes of material properties in the surface layer.

The paper presents the MCSF for composite materials reinforced by stiff fibres. For modelling the interactions by MCFS we used functions dipoles as a source. The boundary conditions on the stiff parts can be defined in the form of rigid body displacements and by strains. Different source functions define different relations between the components of deformation and stress and thus the satisfaction of all boundary conditions is decisive. In some situations different source functions can contribute to a better numerical stability. The source functions are quasi-singular along the fibre boundary. The analytic evaluation of integrals is simple also for a higher order polynomial approximation of the intensities of the source functions.

Acknowledgments

This work was supported by the Slovak Agency APVV (grant APVV-0169-07) and Scientific Grant Agency (grant VEGA-1/0657/09).

Appendix A

This appendix provides the details of kernel functions used in the presented MCSF formulation. The field of displacements in an elastic continuum by a unit force acting in the direction of the axis x_p is given by Kelvin solution

$$U_{pi}^{(F)} = \frac{1}{16\pi G(1-\nu)}\frac{1}{r}\left[(3-4\nu)\delta_{ip} + r_{,i}r_{,p}\right] \qquad \text{(A.1)}$$

where i denotes the x_i coordinate of the displacement, G and v are shear modulus and Poisson's ratio of the material of the matrix (isotropic material is considered here), r is the distance between the source point s where the force is acting with a field point t where the displacement is introduced, i. e.

$$r = \sqrt{r_i r_i},\ r_i = x_i(t) - x_i(s) \tag{A.2}$$

The summation convention over repeated indices acts and

$$r_{,i} = \partial r / \partial x_i(t) = r_i / r \tag{A.3}$$

is the directional derivative of radius vector r. The gradients of displacement fields are corresponding derivatives of the field (1) in the point t

$$U^{(F)}_{pi,j} = -\frac{1}{16\pi G(1-v)r^2}\left[(3-4v)\delta_{pi}r_j - \delta_{pj}r_i - \right. \\ \left. - \delta_{ij}r_p + 3r_i r_j r_p\right] \tag{A.4}$$

Note that the second derivative of the radius vector of n-th power is

$$\left(r^n_{,k}\right)_{i,j} = \frac{n}{r}\left(r^{n-1}_{,k}\delta_{jk} - r_j r^n_{,k}\right) \tag{A.5}$$

The strains are

$$E^{(F)}_{pij} = \frac{1}{2}\left(U^{(F)}_{pi,j} + U^{(F)}_{pj,i}\right) = -\frac{1}{16\pi G(1-v)}\frac{1}{r^2}\cdot \\ \cdot\left[(1-2v)\left(\delta_{pi}r_{,j} + \delta_{pj}r_{,i}\right) - \delta_{ij}r_{,p} + 3r_{,i}r_{,j}r_{,p}\right] \tag{A.6}$$

and the ij stress components of this field are

$$S^{(F)}_{pij} = 2GE^{(F)}_{pij} + \frac{2Gv}{1-2v}\delta_{ij}E^{(F)}_{pkk} = \frac{1}{8\pi(1-v)}\cdot \\ \cdot\frac{1}{r^2}\left[(1-2v)\left(\delta_{ij}r_{,p} - \delta_{jp}r_{,i} - \delta_{ip}r_{,j}\right) + 3r_{,i}r_{,j}r_{,p}\right] \tag{A.7}$$

where δ_{ij} is the Kronecker's delta.

The displacement field of a dipole can be obtained from the displacement field of a force by differentiating it in the direction of the acting force, i.e.

$$U^{(D)}_{pi} = U^{(F)}_{pi,p} = -\frac{1}{16\pi G(1-v)}\frac{1}{r^2}\cdot \\ \cdot\left[3r_{,i}r^2_{,p} - r_{,i} + 2(1-v)r_{,p}\delta_{ip}\right] \tag{A.8}$$

The summation convention does not act over the repeated indices p here and in the following relations, too. Gradients of the displacement field are

$$U^{(D)}_{pi,j} = -\frac{1}{16\pi G(1-v)}\frac{1}{r^3}\cdot \\ \cdot\left[-15r_i r_j r^2_{,p} + 3r_i r_j + 2(1-v)\delta_{ip}\left(\delta_{jp} - 3r_j r_p\right) + \right. \\ \left. + 6r_i r_p \delta_{jp} + \delta_{ip}\left(3r^2_{,p} - 1\right)\right] \tag{A.9}$$

and corresponding strain and stress fields are

$$E^{(D)}_{pij} = \frac{1}{2}\left(U^{(D)}_{pi,j} + U^{(D)}_{pj,i}\right) = \frac{1}{16\pi G(1-v)}\frac{1}{r^3}\cdot \\ \cdot\left[-15r_i r_j r^2_{,p} + 3r_i r_j + 2(1-v)\delta_{ip}\delta_{jp} + \right. \\ \left. + 6v\left(\delta_{ip}r_j r_{,p} + \delta_{jp}r_i r_{,p}\right) + \delta_{ij}\left(3r^2_{,p} - 1\right)\right] \tag{A.10}$$

$$S^{(D)}_{pij} = 2GE^{(F)}_{pij} + \frac{2Gv}{1-2v}\delta_{ij}E^{(D)}_{pkk} = \frac{1}{8\pi(1-v)}\frac{1}{r^3}\cdot \\ \cdot\left[(1-2v)\left(2\delta_{ip}\delta_{jp} + 3r^2_{,p}\delta_{ij} - \delta_{ij}\right) + \right. \\ \left. + 6vr_p\left(r_{,i}\delta_{jp} + r_j\delta_{ip}\right) + 3\left(1 - 5r^2_{,p}\right)r_i r_j\right] \tag{A.11}$$

The displacements (A.1) by a force are weak singular, the displacement gradients, strains and stresses are strong singular. The fields defined by a dipole have one order higher singularity (strong singularity in the displacement field and hyper-singularities in the strain and stress fields). The derivatives in the perpendicular direction to the force define the force couple. The displacement field for the couple is

$$U^{(C)}_{pi} = U^{(F)}_{pi,j} = \frac{1}{16\pi G(1-v)}\frac{1}{r^2}\cdot \\ \cdot\left[3r_{,p}r^2_{,i} - r_{,p} + 2(1-v)r_{,j}\delta_{ip}\right] \tag{A.12}$$

and the corresponding strain and stress fields are

$$E^{(C)}_{pij} = \frac{1}{2}\left(U^{(C)}_{pi,j} + U^{(C)}_{pj,i}\right) = -\frac{1}{16\pi G(1-v)}\frac{1}{r^3}\cdot \\ \cdot\left[-15r_{,p}r_j r^2_{,i} + 3r_{,p}r_j + 2(1-v)\delta_{ip}\delta_{jp} + \right. \\ \left. + 6v\left(\delta_{ip}r_{,i}r_j + \delta_{ij}r_{,i}r_{,p}\right) + \delta_{jp}\left(3r^2_{,i} - 1\right)\right] \tag{A.13}$$

$$S^{(C)}_{pij} = 2GE^{(C)}_{pij} + \frac{2Gv}{1-2v}\delta_{ij}E^{(C)}_{pkk} = \frac{1}{8\pi(1-v)}\frac{1}{r^3}\cdot \\ \cdot\left[(1-2v)\left(2\delta_{ip}\delta_{ij} + 3r^2_{,j}\delta_{jp} - \delta_{jp}\right) + \right. \\ \left. + 6vr_j\left(r_{,j}\delta_{ip} + r_{,p}\delta_{ij}\right) + 3\left(1 - 5r^2_{,i}\right)r_{,p}r_{,j}\right] \tag{A.14}$$

References

[1] KOMPIS, V., ed.: *Composites with Micro-and-nano-Structure,* Computatioonal Modeling and Experiments, Springer Science+Business Media B.V., 2008.

[2] ESHELBY, J. D.: *Elastic Inclusions and Inhomogenities,* In N. I. Sneddon and R. Hill, eds., Progress in Solid Mechanics, Vol. 2, North-Holland, 1961.

[3] MORI, T., TANAKA, K.: *Average Stressing Matrix and Average Elastic Energy of Materials with Misfitting Inclusions,* Acta Metall., 21, 571-574, 1973.
[4] SAUER, R. A., WANG, G., Li, S.: *The Composite Eshelby Tensors and their Application to Homogenization,* Acta Mechanica, Vol. 197, No. 1-2, 2008.
[5] BALAS J., SLADEK J., SLADEK, V.: *Stress Analysis by Boundary Element Methods*, Elsevier, Amsterdam, 1989.
[6] WANG, H., QIN, Q, H.: *A Meshless Method for Generalized Linear and Nonlinear Poisson-type Problems,* Engineering Analysis with Boundary Elements, Vol. 30, No. 6, Elsevier (2006), pp. 515–521.
[7] KOMPIS, V., STIAVNICKY, M., KOMPIS, M., MURCINKOVA, Z., QIN, Q. H.: *Method of Continuous Source Functions for Modeling of Matrix Reinforced by Finite Fibres*, In (Kompis, V., ed.), Composites with Micro- and Nano-structure. Springer Science+Business Media B.V., 2008.
[8] BLOKH, V. I.: *Theory of Elasticity,* University Press, Kharkov, 1964.
[9] KACHANOV, M, SHAFIRO B., TSUKROV, I.: *Handbook of Elasticity Solutions*, Kluver Academic Publishers, 2003.
[10] KOMPIS, V., KOMPIS, M. KAUKIC, M.: *Method of Continuous Dipoles for Modeling of Materials Reinforced by Short Micro-Fibres,* Eng. Anal. with Boundary Elements, 31, pp. 416–424.
[11] KOMPIS, V., STIAVNICKY, M., ZMINDAK, M., MURCINKOVA, Z.: *Trefftz Radial Basis Functions,* In: Proc. of Leuven Symposium on Applied Mechanics in Engineering (LSAME.08), Part I, Proceeding of Trefftz.08, 5th International Workshop on Trefftz Methods, Leuven, 2008.
[12] QU, J., CHERKAOUI, M.: Fundamentals of Micromechanics of Solids. *John Wiley & Sons, Hoboken,* New Jersey, 2006.
[13] KOMPIS, M., STIAVNICKY, M., KOMPIS, M., ZMINDAK, M.: *Trefftz interpolation based multi-domain boundary point method,* Eng. Analysis with Bound. Elem., 29, 391-396, 2005.
[14] MURCINKOVA, Z., KOMPIS, V., STIAVNICKY, M.: *Trefftz Functions for Solution of 3D Problems with Stress Concentration*, In Proc. of Leuven Symposium on Applied Mechanics in Engineering (LSAME.08), Part I, Proc. of Trefftz.08, 5th International Workshop on Trefftz Methods, Leuven, 2008.

Milan Vasko – Milan Saga *

SOLUTION OF MECHANICAL SYSTEMS WITH UNCERTAINTY PARAMETERS USING IFEA

The paper presents a non-traditional computational approach for structural analysis with uncertainties in material, geometry and load parameters. Uncertainties are introduced as bounded possible values - intervals. The main goal is to propose algorithms for interval computations on FEM models suggested by authors. An application of the chosen approaches is presented - the first one, a simple combination of only inf-values or only sup-values; the second one presents full combination of all inf-sup values; the third one uses the optimisation process as a tool for finding out a inf-sup solution and last one is Monte Carlo technique as a comparison tool.

Keywords: uncertain structural parameters, MATLAB, Monte Carlo, interval arithmetic

1. Introduction

In the last years there has been an increased interest in the modeling and analysis of engineering systems under uncertainties. To obtain reliable results for the solution of engineering problems, exact values for the parameters of the model equations should be available. Really, however, those values can often not be provided, and the models usually exhibit a rather high degree of uncertainty. Computational mechanics, for example, entails uncertainties in geometry, material and load parameters as well as in the model itself and in the analysis procedure too. For that reason, the responses, such as displacements, stresses, resonant frequency, or other dynamic characteristics, will usually exhibit any degree of uncertainty. It means that the obtained result using one specific value as a most significant value for uncertain parameter cannot be considered to be representative for the whole spectrum of possible results.

It is generally known that probabilistic modeling and statistical analysis is well-established for modeling of mechanical systems with uncertainties. In addition, a number of non-probabilistic computational techniques have been proposed, e.g. fuzzy set theory [1, 2, 10], interval approach [2, 6], imprecise probabilities [9], etc. The growing interest in these approaches originated from criticism of the credibility of probabilistic approach when input dates are insufficient [10]. It is argued that the new non-probabilistic treatments could be more appropriate in modeling of the vagueness.

The uncertainty is assumed to be unknown but bounded with lower and upper bounds. The uncertainties in the model parameters, model inputs etc. can then be taken into account by interval numbers derived from experimental data or expert knowledge. By this technique, the complete information about the uncertainties in the model may be included and one can demonstrate how these uncertainties are processed through the calculation procedure in MATLAB.

2. Fundamental Principles of Interval Arithmetic

Interval arithmetic was developed by R. E. Moore [5] while studying the propagation and control of truncation and round off error using floating point arithmetic on a digital computer. Moore was able to generalize this work into the arithmetic independent of machine considerations [5, 7].

In this approach, an uncertain number is represented by an interval of real numbers. An interval number [3, 5, 7] is a closed set **R** that includes the possible range of an unknown real number where **R** denotes the set of real numbers. Therefore, a real interval is a set of the form

$$\mathbf{x} = \left[\underline{x}, \overline{x}\right] = \left\{x \in \mathbf{R}: \underline{x} \le x \le \overline{x}\right\},$$

where $\underline{x}$ and $\overline{x}$ are the lower (*infimum*) and upper (*supremum*) bounds of the interval number **x** respectively, and the bounds are elements of **R** with $\underline{x} \le \overline{x}$. Definition of real intervals and operations with intervals could be found in a number of references [2, 3, 6, 7, 10]. Let's define basic properties of interval number that have been inbuilt in INTLAB [8]:

- the *midpoint* of **x**: $\mathrm{mid}(x) = \breve{x} = \frac{1}{2}\left(\underline{x} + \overline{x}\right)$,
- the *radius* of **x**: $rad(\mathbf{x}) = \frac{1}{2}\left(\overline{x} - \underline{x}\right)$,
- the *absolute value* or the *magnitude* of **x**: $|\mathbf{x}| = mag(\mathbf{x}) = \max\left\{|\tilde{x}|: \tilde{x} \in \mathbf{x}\right\}$,

* **Milan Vasko, Milan Saga**
Department of Applied Mechanics, Faculty of Mechanical Engineering, University of Zilina, E-mail: milan.vasko@fstroj.uniza.sk

- the *magnitude* of **x**: $mig(\mathbf{x}) = \min\{|\tilde{x}| : \tilde{x} \in \mathbf{x}\}$.

Given $\mathbf{x}[\underline{x}, \overline{x}]$ and $\mathbf{y} = [\underline{y}, \overline{y}]$, the four elementary operations are defined by

$$\mathbf{x} + \mathbf{y} = \left[\underline{x} + \underline{y}, \overline{x} + \overline{y}\right],$$

$$\mathbf{x} - \mathbf{y} = \left[\underline{x} - \overline{y}, \overline{x} - \underline{y}\right],$$

$$x \times y = \left[\min\left\{\underline{xy}, \underline{x}\overline{y}, \overline{x}\underline{y}, \overline{xy}\right\}, \max\left\{\underline{xy}, \underline{x}\overline{y}, \overline{x}\underline{y}, \overline{xy}\right\}\right],$$

$\mathbf{x} \div \mathbf{y} = \mathbf{x} \times 1/\mathbf{y}$, where $1/\mathbf{x} = \left[1/\overline{x}, 1/\underline{x}\right]$ if $\underline{x} > 0, \overline{x} < 0$.

For the elementary interval operations, division by an interval containing zero is not defined. It is often useful to remove this restriction to give what is called extended interval arithmetic [3]. Extended interval arithmetic leads to the following rules. If $\mathbf{x}[\underline{x}, \overline{x}]$ and $\mathbf{y} = [\underline{y}, \overline{y}]$ with $\underline{y} \le 0 \le \overline{y}$ and $\underline{y} < \overline{y}$, then the rules for division are as follows

$$\mathbf{x}/\mathbf{y} = \begin{Bmatrix} \left[\overline{x}/\underline{y}, \infty\right] & if\ \overline{x} \le 0\ and\ \overline{y} = 0 \\ \left[-\infty, \overline{x}/\overline{y}\right] \cup \left[\overline{x}/\underline{y}, \infty\right] & if\ \overline{x} \le 0\ and\ \underline{y} < 0 < \overline{y} \\ \left[-\infty, \overline{x}/\overline{y}\right] & if\ \overline{x} \le 0\ and\ \underline{y} = 0 \\ \left[-\infty, \infty\right] & if\ \underline{x} < 0 < \overline{x} \\ \left[-\infty, \underline{x}/\underline{y}\right] & if\ \underline{x} \ge 0\ and\ \overline{y} = 0 \\ \left[-\infty, \underline{x}/\underline{y}\right] \cup \left[\underline{x}/\overline{y}, \infty\right] & if\ \underline{x} \ge 0\ and\ \underline{y} < 0 < \overline{y} \\ \left[\underline{x}/\overline{y}, \infty\right] & if\ \underline{x} \ge 0\ and\ \underline{y} = 0 \end{Bmatrix}.$$

For further rules for extended interval arithmetic see [2, 3, 7, 10].

3. Computational Approaches in Interval Matrix Analysis

Considering uncertain parameters in interval form, we'll realize comparison study of the few basic matrix operations:

- solution of the linear equations system (INTLAB function – *verifylnss*),
- solution of the eigenvalue problem (INTLAB function – *verifyeig*).

The alternative way of the interval arithmetic [8] can be the following numerical approaches:

- so called Monte Carlo computational technique,
- Inf-Sup simple analysis (COM1),
- Inf-Sup full analysis (COM2),
- Inf-Sup optimising analysis (OPT).

The comparison was realised through the use of midpoint residual vector $\mathbf{r}_{Midpoint}$ and radius residual vector $\mathbf{r}_{Residual}$ expressed in %, e.g.

$$\mathbf{r}_{Midpoint} = \left|\frac{\mathrm{mid}(\mathbf{y}_{Intlab}) - \mathrm{mid}(\mathbf{y}_{MC})}{\mathrm{mid}(\mathbf{y}_{Intlab})}\right| \cdot 100\%$$
$$\mathbf{r}_{Radius} = \left|\frac{\mathrm{rad}(\mathbf{y}_{Intlab}) - \mathrm{rad}(\mathbf{y}_{MC})}{\mathrm{rad}(\mathbf{y}_{Intlab})}\right| \cdot 100\%$$,

Monte Carlo method (MC) is a time consuming but reliable solution. Various combinations of the uncertain parameter deterministic values are generated and after the subsequent solution in the deterministic sense we obtain a complete set of results processed in an appropriate manner. Infimum and supremum calculation is following

$$\begin{aligned} &\inf(F) = \text{minof all results } F(p_i), \text{ where } i = 1, ..., m \text{ and} \\ &m \approx 5000 \div 100000, \\ &\sup(F) = \text{minof all results } F(p_i), \text{ where } i = 1, ..., m \text{ and} \\ &m \approx 5000 \div 100000. \end{aligned} \quad (2)$$

The second method (COM1), i.e. the solution evaluation in marginal values of interval parameters has its physical meaning for many engineering problems. We consider an approach where the extreme output values are obtained by the application of the extreme parameter values on input. That means that the infimum/supremum is obtained using the deterministic analysis for infimum or supremum of input uncertain parameters. *Inf-Sup* calculation is

$$\begin{aligned} &\inf(F) = \min \text{ of } [F(\underline{p}), F(\overline{p})] \text{ and} \\ &\sup(F) = \max \text{ of } [F(\underline{p}), F(\overline{p})]. \end{aligned} \quad (3)$$

The third approach (COM2), which is also based on the set of deterministic analyses appears as the more suitable one. The marginal interval parameter values are considered again but the infimums and supremums are also combined. The method provides satisfying results and can be marked as reliable, even if there is still a doubt about the existence of the extreme solution for the uncertain parameter inner values. A solution for two interval numbers $p_1 = \langle a_1\ b_1 \rangle$ and $p_2 = \langle a_2\ b_2 \rangle$ may be found in the following computational way

$$\begin{aligned} &\inf(F) = \min \text{ of } [F(a_1\ a_2), F(a_1\ b_2), F(b_1\ a_2), F(b_1\ b_2)] \\ &\text{and} \\ &\sup(F) = \max \text{ of } [F(a_1\ a_2), F(a_1\ b_2), F(b_1\ a_2), F(b_1\ b_2)]. \end{aligned} \quad (4)$$

The last numerical method of the infimum and supremum solution searching using the optimization techniques (OPT) is proposed by the authors as an alternative to the first and to the third method. It should eliminate a big amount of analyses in the first method and also eliminates the problem with the possibility of the infimum and supremum existence inside the interval parameters for the deterministic values. Computational process for the two interval numbers $p_1 = \langle a_1\ b_1 \rangle$ and $p_2 = \langle a_2\ b_2 \rangle$ may be found as follows

$$\begin{aligned} &\inf(F) = F(\mathbf{p}_{OPT}) \text{ i.e. find } \mathbf{p}_{OPT} \text{ so that } F(\mathbf{p}_{OPT}) \to \min. \\ &\text{and} \\ &\sup(F) = F(\mathbf{p}_{OPT}) \text{ i.e. find } \mathbf{p}_{OPT} \text{ so that } F(\mathbf{p}_{OPT}) \to \max. \end{aligned} \quad (5)$$

The authors used also the interval arithmetic principles implemented in INTLAB [8] as another computing tool. However, the overestimate effect mentioned above for the significant uncertainties causes considerable problems and the possibilities of INTLAB using are therefore very restricted. INTLAB using makes sense particularly for simple problems because of the results obtaining speed.

Testing example 1

Let's applied the presented methods into the solution of the following system

$$\begin{bmatrix} \langle 0.1 \rangle & 1 \\ -2 & \langle -1.2 \rangle \end{bmatrix} \cdot \begin{bmatrix} y_1 \\ y_2 \end{bmatrix} = \begin{bmatrix} \langle 0.2 \rangle \\ 0 \end{bmatrix}.$$

The solution is shown in Fig. 1 and used confrontation methods are summarized in Tab. 1.

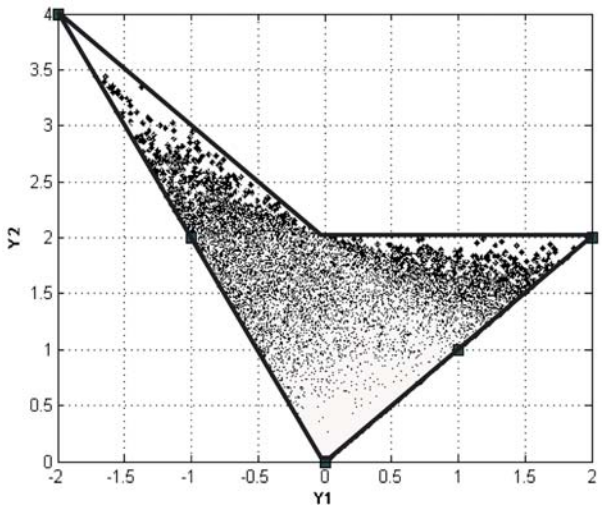

Fig. 1 Results map of interval linear equations system

Results obtained by proposed numerical methods Tab. 1

	Exact solution	1st method MC	2nd method COM1	3rd method COM2	4th method OPT	5th method INT
Y1	<-2 2>	<-1.95 1.94>	<-1 1>	<-2 2>	<-2 0>	<-4.78 4.78>
Y2	<0 4>	<0 3.91>	<0 2>	<0 4>	<0 4>	<-5.1 5.1>

In general, the interval system of equations solving may be a complicated problem (mainly for large dimension, [7]). Good information about the solution set is obtained using the Monte Carlo method. The other methods determine only the marginal values with bigger or smaller inaccuracies. The 1st and the 3rd used methods are particularly suitable for the equations systems solving according to the experiences of the authors. In case of the fourth method application (the optimization method) there is a problem with formulation of the appropriate test function which would properly describe searching of multiple inf or sup solutions. INTLAB usage appears to be unsuitable because the parameter uncertainty is rather strong.

Testing example 2

Let's compare proposal interval computational methods to solve the following eigenvalues problem

a) with a small signification of the parameters uncertainty, e.g.

$$\left(\begin{bmatrix} \langle 19400\ 19500 \rangle & -\langle 9400\ 9450 \rangle \\ -\langle 9400\ 9450 \rangle & \langle 9400\ 9450 \rangle \end{bmatrix} - \lambda_i \cdot \right.$$
$$\left. \cdot \begin{bmatrix} \langle 20\ 20.1 \rangle & 0 \\ 0 & \langle 18\ 18,1 \rangle \end{bmatrix} \right) \cdot \begin{bmatrix} v_1 \\ v_2 \end{bmatrix}_i = \begin{bmatrix} 0 \\ 0 \end{bmatrix}$$

b) with a larger signification of the parameters uncertainty, e.g.

$$\left(\begin{bmatrix} \langle 19400\ 21400 \rangle & -\langle 9400\ 10400 \rangle \\ -\langle 9400\ 10400 \rangle & \langle 9400\ 10400 \rangle \end{bmatrix} - \lambda_i \cdot \right.$$
$$\left. \cdot \begin{bmatrix} \langle 20\ 25 \rangle & 0 \\ 0 & \langle 18\ 22 \rangle \end{bmatrix} \right) \cdot \begin{bmatrix} v_1 \\ v_2 \end{bmatrix}_i = \begin{bmatrix} 0 \\ 0 \end{bmatrix}$$

Inf-sup results were compiled into tab. 2. Graphic presentation of the results is shown in Fig. 2.

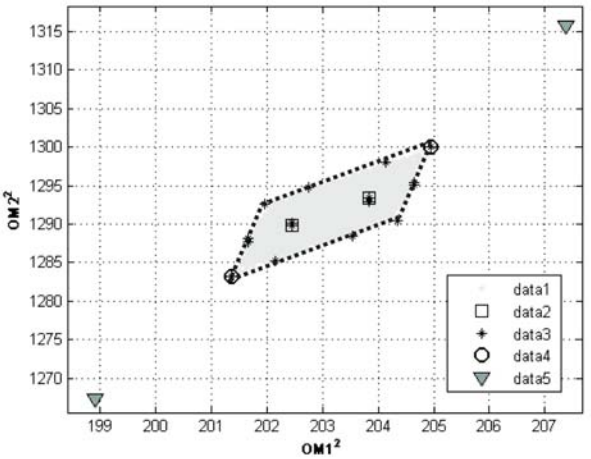

Fig. 2 Solution of the set eigenvalues with small uncertainties

data1 – Monte Carlo analysis
data2 – COM1, evaluation in marginal values (only inf or only sup)
data3 – COM2, evaluation for all marginal values-all combinations
data4 – OPT, inf and sup searching using optimizing technique application
data5 – direct application of the interval arithmetic using INTLAB
---- – boundary of the all possible solutions set

The solution of an eigenvalues problem as a frequent task of solid mechanics has demonstrated facilities of particular approaches. The Monte Carlo method usually gives good information about the solution set. Other methods determine only marginal values. For the eigenvalues analysis of the systems with interval parame-

ters the authors recommend according to their experiences to use particularly the 1st, 3rd and 4th method. All of them give satisfying results but especially the 3rd and 4th ones appear to be the most suitable. From the effectiveness perspective the third method can be considered as the best even if there is a risk of losing the inner interval number solutions. The usage of the second and the fifth method (INTLAB) is determined by the uncertainty importance (the interval size). As it is presented, all the methods are acceptable in case of a minor uncertainty (solution A).

4. Interval finite elements analysis (IFEA)

It is common knowledge that the finite element method (FEM) [4, 6, 10] is a very popular tool for complicated structural analysis. The ability to predict the behavior of a structure under static or dynamic loads is not only of great scientific value, it is also very useful from an economical point of view. A reliable FE analysis could reduce the need for prototype production and therefore significantly reduce the associated design validation cost.

It is sometimes very difficult to define a reliable FE model for realistic mechanical structures when a number of its physical properties are uncertain. Particularly, in the case of FE analysis, the mechanical properties of the used materials are very hard to predict, and therefore an important source of uncertainty. Reliable validation can only be based on an analysis which takes into account all uncertainties that could cause this variability. It is the aim of this part to incorporate most important uncertainties in FE analysis.

According to character of the uncertainty we can define a structural uncertainty (geometrical and material parameters) and uncertainty in load (external forces, etc.). The structural uncertainty parameters are usually written into vector $[\mathbf{x}] = [\underline{\mathbf{x}}, \overline{\mathbf{x}}]$ and the interval static (time independent) FE analysis may be formulated as follows

$$\mathbf{K}([\mathbf{x}])\cdot\mathbf{u} = \mathbf{f}([\mathbf{x}]) \text{ or } \left[\underline{\mathbf{K}}, \overline{\mathbf{K}}\right]\cdot\left[\underline{\mathbf{u}}, \overline{\mathbf{u}}\right] = \left[\underline{\mathbf{f}}, \overline{\mathbf{f}}\right],$$

where $\underline{\mathbf{K}}$, $\overline{\mathbf{K}}$ are the infimum and supremum matrices of the stiffness matrix $\mathbf{K}$, $\mathbf{u}$, $\overline{\mathbf{u}}$ are the infimum and supremum vectors of the displacements vector $[\mathbf{u}]$, $\underline{\mathbf{f}}$, $\overline{\mathbf{f}}$ are the infimum and supremum vectors of the loading vector $\mathbf{f}$. Considering a dynamic conservative system, the interval modal and spectral matrices can be obtained using the solution of

$$\left[\mathbf{K}(\mathbf{x}) - \lambda_j\cdot\mathbf{M}(\mathbf{x})\right]\cdot\mathbf{v}_j = 0 \text{ or}$$

$$\left(\left[\underline{\mathbf{K}}, \overline{\mathbf{K}}\right] - \left[\underline{\lambda_j}, \overline{\lambda_j}\right]\cdot\left[\underline{\mathbf{M}}, \overline{\mathbf{M}}\right]\right)\cdot\left[\underline{v_j}, \overline{v_j}\right] = 0,$$

where $\underline{\lambda_j}$, $\overline{\lambda_j}$ and $\underline{v_j}$, $\overline{v_j}$ are the j-th eigenvalue with a corresponding eigenvector $\underline{\mathbf{K}}$, $\overline{\mathbf{K}}$, $\underline{\mathbf{M}}$, $\overline{\mathbf{M}}$ are naturally the infimum and supremum of the mass and stiffness matrices. The application of classical interval arithmetic for FE analysis is very limited. Its "overestimating" grows with a problem size (dimension of system matrices) and really has no physical foundation. Therefore, it is effective to apply the previous numerical methods.

The application of the Monte Carlo method in IFEA may be realized as follows

Static analysis

1. step: generation of the random matrix (uniform distribution)
$\mathbf{X}_{MC} = [x_i, \ldots, x_m], \quad (m \approx 5000 \div 100000)$
2. step: solution of
$\mathbf{U}_{MC} = \left[\mathbf{K}(x_1)^{-1}\cdot\mathbf{f}(x_1), \ldots, \mathbf{K}(x_m)^{-1}\cdot\mathbf{f}(x_m)\right]$

3. step:
- infimum calculation $\underline{u_i} = \inf(i^{th}\ row\ of\ \mathbf{U}_{MC}) \rightarrow \underline{\mathbf{u}}$,
- supremum calculation $\overline{u_i} = \sup(i^{th}\ row\ of\ \mathbf{U}_{MC}) \rightarrow \overline{\mathbf{u}}$.

Eigenvalues analysis

1. step: generation of the random matrix (uniform distribution)
$\mathbf{X}_{MC} = [x_i, \ldots, x_m], \quad (m \approx 5000 \div 100000)$
2. step: solution of
$\lambda_{j\_MC} \rightarrow \left[\mathbf{K}(x_j) - \lambda_{j\_MC}\cdot\mathbf{M}(x_j)\right]\cdot\mathbf{v}_j = 0\, for\ j = 1, \ldots, m$

3. step:
- infimum calculation of the i-th eigenvalue
$\underline{\lambda_i} = \inf(i^{th}\ row\ of\ \lambda_{MC})$,
- supremum calculation of the i-th eigenvalue
$\overline{\lambda_i} = \sup(i^{th}\ row\ of\ \lambda_{MC})$.

In the case of implementation of COM1 numerical approach to IFEA is as follows

Static analysis

- infimum calculation $\underline{\mathbf{u}} = \mathbf{K}(\underline{\mathbf{x}})^{-1}\cdot\mathbf{f}(\underline{\mathbf{x}})$
- supremum calculation $\overline{\mathbf{u}} = \mathbf{K}(\overline{\mathbf{x}})^{-1}\cdot\mathbf{f}(\overline{\mathbf{x}})$.

Results obtained by proposed numerical methods — Tab. 2

		1st method	2nd method	3rd method	4th method	5th method
A	λ_1	<201 203>	<202.3 202.5>	<201 203>	<201 203>	<199 206>
	λ_2	<1284 1296>	<1289 1290>	<1283 1296>	<1283 1296>	<1268 1312>
B	λ_1	<167 220>	<181 202>	<164 223>	<164 223>	<95 287>
	λ_2	<1059 1415>	<1147 1290>	<1039 1425>	<1038 1425>	<600 1827>

Eigenvalues analysis

– infimum calculation

$$\underline{\boldsymbol{\lambda}} \rightarrow \left[\mathbf{K}(\underline{\mathbf{x}}) - \underline{\boldsymbol{\lambda}} \cdot \mathbf{M}(\underline{\mathbf{x}})\right] \cdot \underline{\mathbf{v}} = 0$$

– supremum calculation

$$\overline{\boldsymbol{\lambda}} \rightarrow \left[\mathbf{K}(\overline{\mathbf{x}}) - \overline{\boldsymbol{\lambda}} \cdot \mathbf{M}(\overline{\mathbf{x}})\right] \cdot \overline{\mathbf{v}} = 0$$

COM1 doesn't give correct results every time. Using COM2 we can obtain more correct results. Its computational process for IFEA is

Static analysis

1. step: calculation of realizations matrix X_2, i.e. 2^n inf-sup combinations, (n – number of uncertain system parameters), $\mathbf{X}_{COM2} = [\mathbf{x}_1, \ldots, \mathbf{x}_m], (m = 2^n)$
2. step: solution of $\mathbf{U}_{COM2} = \left[\mathbf{K}(\mathbf{x}_1)^{-1} \cdot \mathbf{f}(\mathbf{x}_1), \ldots, \mathbf{K}(\mathbf{x}_m) \cdot \mathbf{f}(\mathbf{x}_m)\right]$
3. step:

– infimum calculation $\underline{\mathbf{u}_i} = \inf\left(i^{th} \text{ row of } \mathbf{U}_{MC}\right) \rightarrow \underline{\mathbf{u}}$,

– supremum calculation $\overline{\mathbf{u}_i} = \sup\left(i^{th} \textit{ row of } \mathbf{U}_{MC}\right) \rightarrow \overline{\mathbf{u}}$.

Eigenvalues analysis

1. step: calculation of realizations matrix X_2, i.e. 2^n inf-sup combinations, (n – number of uncertain system parameters), $\mathbf{X}_{COM2} = [\mathbf{x}_1, \ldots, \mathbf{x}_m], (m = 2^n)$
2. step: solution of $\boldsymbol{\lambda}_{j\_COM2} \rightarrow \left[\mathbf{K}(\mathbf{x}_j) - \boldsymbol{\lambda}_{j\_COM2} \cdot \mathbf{M}(\mathbf{x}_j)\right] \cdot \mathbf{v}_j = 0 \quad \text{for } j = 1, \ldots, m$
3. step:

– infimum calculation of the i-th eigenvalue $\underline{\lambda_i} = \inf\left(i^{th} \text{ row of } \boldsymbol{\lambda}_{COM2}\right)$,

– supremum calculation of the i-th eigenvalue $\overline{\lambda_i} = \sup\left(i^{th} \textit{ row of } \boldsymbol{\lambda}_{COM2}\right)$.

Generally, the infimum or supremum are not found in only bound points (COM1, COM2) but also in inner domain of the solution set (OPT). To find inf-sup solution using the OPT approach means to solve the optimizing problem described as follows

Static analysis

– infimum calculation $\underline{u_i}(\mathbf{x}_{OPT}) \rightarrow$ minimize value i^{th} member of $\left[\mathbf{K}(\mathbf{x})^{-1} \cdot \mathbf{f}(\mathbf{x})\right]$

– supremum calculation $\overline{u_i}(\mathbf{x}_{OPT}) \rightarrow$ maximize value i^{th} member of $\left[\mathbf{K}(\mathbf{x})^{-1} \cdot \mathbf{f}(\mathbf{x})\right]$.

Eigenvalues analysis

– infimum calculation of the *i-th* eigenvalue $\underline{\lambda_i}(\mathbf{x}_{OPT}) \rightarrow$ minimize value of λ_i for eq. $\left[\mathbf{K}(\mathbf{x})^{-1} - \lambda_i \cdot \mathbf{M}(\mathbf{x})\right] \cdot \mathbf{v}_i = 0$,

– supremum calculation of the *i-th* eigenvalue $\overline{\lambda_i}(\mathbf{x}_{OPT}) \rightarrow$ minimize value of λ_i for eq. $\left[\mathbf{K}(\mathbf{x})^{-1} - \lambda_i \cdot \mathbf{M}(\mathbf{x})\right] \cdot \mathbf{v}_i = 0$,.

It should be noted that the searching process can be realized by a comparison of an optimizing method (e.g. Nelder-Mead simplex algorithm) or by using a genetic algorithm as a robust tool of global optimization.

Testing example 3 – Stress interval analysis of the truss structure

For the following research purpose on the interval finite element model computing, the truss structure shown in Fig. 3 was analyzed, where the geometry of the structure is presented. The truss structure was loaded by uncertain forces F1 and F2. The certain model parameters are defined as follows

- element mass density $\rho = 2700 \text{ kg} \cdot \text{m}^{-3}$,
- nodal concentrated mass (nodes 33, 34, 35, 36) $m = 50$ kg.

Stress interval analysis of the truss structure

Let's assume the following uncertain model parameters:

- Young's modulus $E = \langle 0.95 \;\; 1.05 \rangle \cdot 2 \cdot 10^{11}$ Pa,
- cross section areas $A_1 = \langle 0.95 \;\; 1.05 \rangle \cdot 569 \text{ mm}^2$, $A_2 = \langle 0.95 \;\; 1.05 \rangle \cdot 691 \text{ mm}^2$, $A_3 = \langle 0.95 \;\; 1.05 \rangle \cdot 1550 \text{ mm}^2$,
- loading forces F_1 and F_1 $F = \langle 0.9 \;\; 1.1 \rangle \cdot \begin{Bmatrix} 35000 \\ 50000 \end{Bmatrix} N$.

The input uncertain parameters in the vector form will be defined for the further analyses as follows

$$\mathbf{x} = [E, A_1, A_2, A_3, F_1, F_2] .$$

The purpose of this study will be to compare the efficiency and exactness of the proposed methods MC, COM1, COM2 and OPT. The results of the MC analysis will be considered as reference values and will be used for the construction of the solution map. In the case of MC method, 5000 random inputs were generated; they were evaluated and properly processed to inf-sup solutions.

The maximal stress values calculated by the particular methods for the truss loaded by maximal stress (truss no. 15) achieved the following values:

$$\langle \sigma_{15} \rangle = \begin{matrix} \langle -343 \;\; -255 \rangle \;\; (\text{MC}) \\ \langle -343 \;\; -255 \rangle \;\; (\text{COM1}) \\ \langle -343 \;\; -255 \rangle \;\; (\text{OPT}) \\ \langle -343 \;\; -255 \rangle \;\; (\text{COM2}) \end{matrix}$$

The results are obtained from the final arrangement of the solution set applying the searching algorithm for the infimum and supremum as follows:

$$\inf = \min\left(\max\left|\sigma(\mathbf{x})\right|\right),$$

$$\sup = \max\left(\max\left|\sigma(\mathbf{x})\right|\right).$$

If the COM1, COM2 and OPT methods are compared with the MC method, it can be observed that:

- the COM1 method is less appropriate and is not recommended for this kind of analyses,
- the OPT method provides comparable, in some cases even better results than the MC method and what is very important, it does not need so many analyses as the MC method,

- the disadvantage of MC and OPT methods is a problem with finding a solution in the solution map corners,
- the COM2 method does not necessarily have to give exact results, but from the perspective of the number of performed analyses, it is more effective than the MC or OPT methods and it can "find" the solutions in the solution map corners,
- the previous considerations lead to the recommendation to combine COM2 and MC or OPT methods.

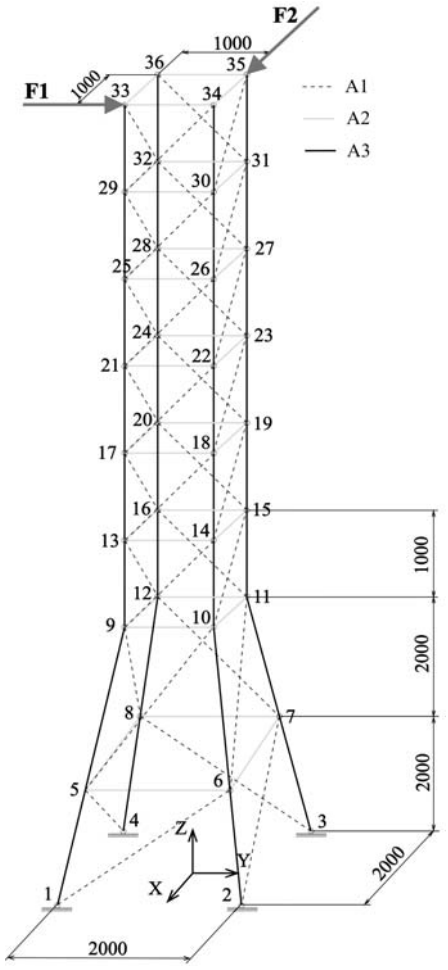

Fig. 3 Analyzed truss structure

Errors in midpoints of the stress in critical element No. 15 — Tab. 3

Stress	MC	COM1		OPT		COM2	
	Reference midpoint	Midpoint	Error [%]	Midpoint	Error [%]	Midpoint	Error [%]
σ_{15} [MPa]	-299	-299.5	0.17	-299.5	0.17	-298.5	0.17

Errors in radiuses of the stress in critical element No. 15 — Tab. 4

Stress	MC	COM1		OPT		COM2	
	Reference midpoint	Radius	Error [%]	Radius	Error [%]	Radius	Error [%]
σ_{15} [MPa]	44	14.5	67	34.5	21.6	44.5	1.1
Application possibility	good	bad		limited		good	

Testing example 4 – Interval eigenvalue solving of fourdrinier structures

For the following research purposes on the interval finite element model computing, the frame structure shown on the Fig. 4 was analyzed. The certain material parameters are defined as follows element mass density $\rho = 2700\ \mathrm{kg} \cdot \mathrm{m}^{-3}$ and Young's modulus $E = 2 \cdot 10^{11}$ Pa.

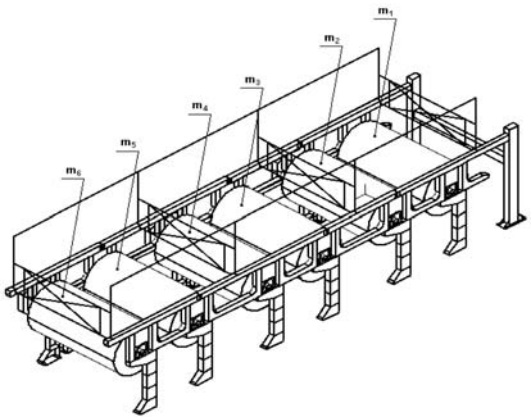

Fig. 4 Analyzed fourdrinier structure

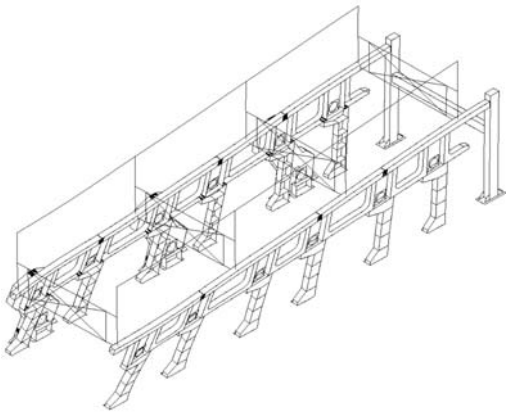

Fig. 5 Modal shape for natural freq. f_1 = 3.69 Hz

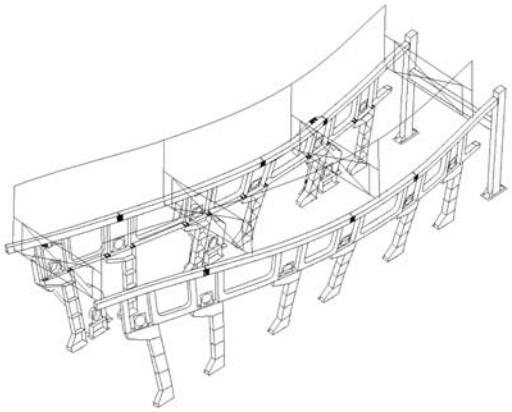

Fig. 6 Modal shape for natural freq. f_2 = 4.17 Hz

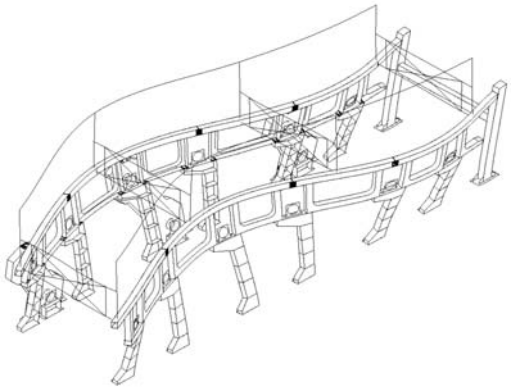

Fig. 7 Modal shape for natural freq. f_3 = 5.56 Hz

The purpose of this study is to compare the efficiency and exactness of the proposed methods MC, COM1, COM2 and OPT. The results of the MC analysis are considered as the reference values and are used for the construction of the solution map. The interval modal and spectral analysis of the identical structure was realized assuming the following uncertain model parameters (mass of cylinders, Fig. 4):

$\mathbf{x} = [m_1, m_2, m_3, m_4, m_5, m_6]$, where $m_{1\div6} \in \langle 0, 2200 \rangle$ [Pa].

The solution will now consider only the analyses of the first three interval natural frequencies f_1, f_2 and f_3 (See Figs. 5, 6, 7). In the case of MC method, 2000 random inputs were generated, evaluated and properly processed to inf-sup solutions

$\inf = \min(f_1(\mathbf{x}))$, $\sup = \min(f_2(\mathbf{x}))$.

The interval solution results are summarized in Tabs. 5, 6, and 7.

Errors in midpoints of natural frequencies Tab. 6

Freq. no.	MC	COM1		OPT		COM2	
	Reference midpoint	Midpoint	Error [%]	Midpoint	Error [%]	Midpoint	Error [%]
f_1 [Hz]	3.41045	3.4250	0.427	3.42185	0.334	3.4249	0.424
f_2 [Hz]	3.8521	3.8835	0.815	3.8395	0.327	3.88355	0.816
f_3 [Hz]	5.1571	5.165	0.153	5.0065	2.92	5.165	0.153

Errors in radiuses of natural frequencies Tab. 7

Freq. no.	MC	COM1		OPT		COM2	
	Reference midpoint	Radius	Error [%]	Radius	Error [%]	Radius	Error [%]
f_1 [Hz]	0.21575	0.253	17.265	0.25015	15.944	0.2532	17.358
f_2 [Hz]	0.2295	0.2895	26.144	0.2459	7.146	0.28995	26.340
f_3 [Hz]	0.3405	0.396	16.300	0.238	30.103	0.3965	16.446

The graphical representation for the all computational approaches is shown in Fig. 8. This figure presents a map of the input data set for each of the methods. The "iterative" map with the infimum and supremum of the first two natural frequencies obtained using the suggested methods is shown in Fig. 9. Due to the effectiveness of the COM2 and OPT methods a short comparison of their iteration history was done. Figs. 10 and 11 present iteration history of the cylinder masses and Figs. 12 and 13 map the iteration process of the natural frequencies f_1, f_2.

Results of natural frequencies Tab. 5

Freq. no.	MC	COM1	OPT	COM2
f_1 [Hz]	⟨3.1947 3.6262⟩	⟨3.1720 3.6780⟩	⟨3.1717 3.6720⟩	⟨3.1717 3.6781⟩
f_2 [Hz]	⟨3.6226 4.0816⟩	⟨3.5940 4.1730⟩	⟨3.5936 4.0854⟩	⟨3.5936 4.1735⟩
f_3 [Hz]	⟨4.8166 5.4976⟩	⟨4.7690 5.5610⟩	⟨4.7685 5.2445⟩	⟨4.7685 5.5615⟩

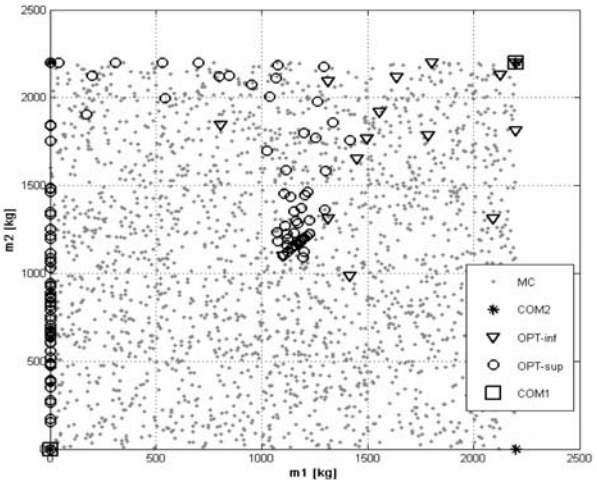

Fig. 8 Mapping of the generated input data for applied methods

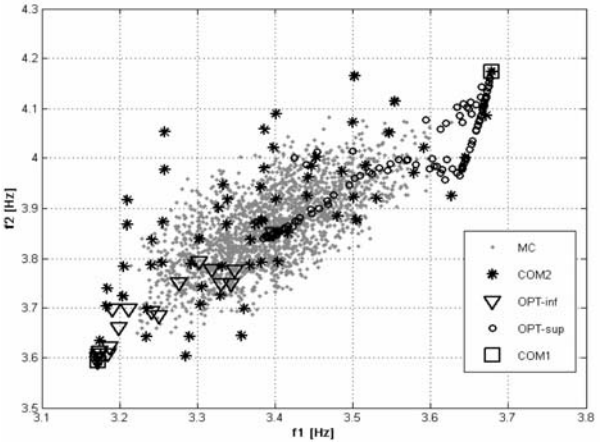

Fig. 9 Mapping of the solution history for 1st and 2nd natural frequences

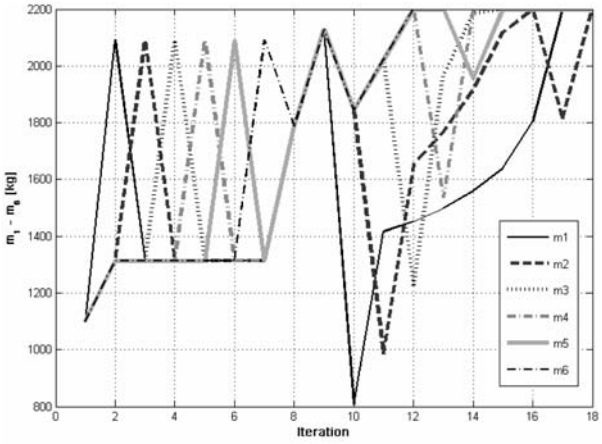

Fig. 10 History of the iteration process for cylinder masses - COM2

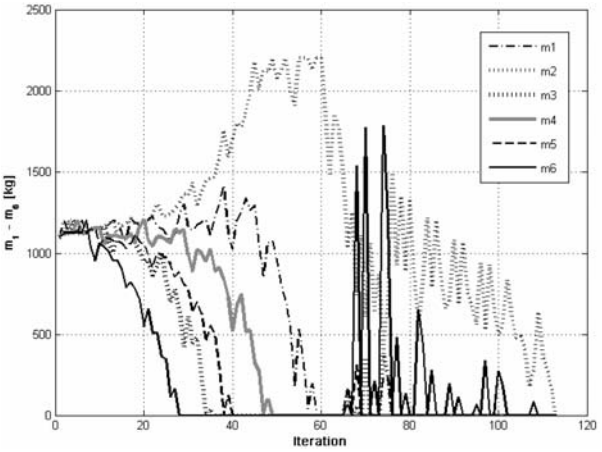

Fig. 11 History of the iteration process for cylinder masses - OPT

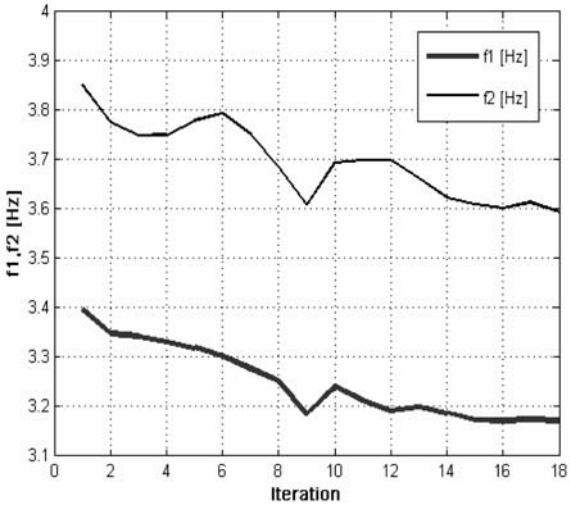

Fig. 12 History of the iteration process for natural frequences f_1, f_2 - COM2

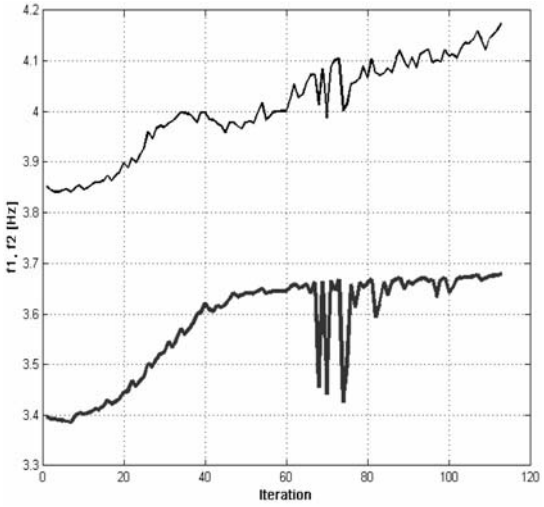

Fig. 13 History of the iteration process for natural frequences f_1, f_2 - OPT

On the basis of the results obtained from the interval estimations of the FEM models spectral properties it is possible to conclude:

- the appropriateness of OPT algorithm application, which mainly due to the simplicity of the criteria function for the infimum or supremum analysis gives excellent results, in some cases even better than the MC method,
- the previous fact relates to the application of genetic searching algorithms, whose biggest advantage is their universality and particularly searching for global extremes,
- the inappropriateness of the COM1 method is demonstrated again because it shows a considerable deflection against the other methods,
- the COM2 method has a limited use but it can be suitable in combination with the OPT method because of "locating" of the solution map corner solutions.

5. Conclusion

The paper presents methods and their applications in an interval structural analysis. The interval arithmetic provides a new possibility of the appraisal of quality and reliability of analyzed objects. Due to this numerical approach we can more authentically analyze mechanical, technological, service and economic properties of investigated structures.

The interval finite element method is a new tool for engineering problems with uncertain – inexact parameters. In the paper we investigated possibilities of the stress-strain and modal-spectral solution of finite element models with interval loading, interval geometry (interval cross section areas of the truss structure) and also interval material properties. We analyzed the interval stress response and interval natural frequency of the testing FE model.

It should be noted that the presented approaches are appropriate for linear models, the non-linearity can raise problems with solution stability and its convergence. The centre of our interest was mainly a comparison of the suggested numerical algorithms and their effectiveness evaluation.

Acknowledgements

This work has been supported by AV grant No. 4/2044/08 and VEGA grant No. 1/4099/07.

References

[1] DEKYS, V., SAPIETOVA, A., KOCUR, R.: *On the reliability estimation of the conveyer mechanism using the Monte Carlo method,* Proc. of COSIM2006, Krynica – Zdroj, 2006, pp. 67–74.

[2] ELISHAKOFF, I., DUAN, D.: *Application of Mathematical Theory of Interval Analysis to Uncertain Vibrations,* Proc. of NOISECON'94, Ft. Lauderdale, Florida, pp. 519–524, 1994.

[3] FORSSEN, P.: *Interval methods I.*, electronic text: http://www.tdb.uu.se/kurs/optim-mn1/ht01/lectures/lec14_2.pdf

[4] KULPA, Z., POWNUK, A., SKALNA, I.: *Analysis of linear mechanical structures with uncertainties by means of interval methods,* Computer Assisted Mechanics and Engineering Sciences, 1998, Vol. 5, Poland, pp. 443–477.

[5] MOORE R., E.: *Interval Analysis.* Prentice Hall, Englewood Cliffs, New Jersey, 1966.

[6] MUHANNA, R., L., MULLEN, R. L.: *Sharp enclosure for material uncertainty in solid and structural mechanics – interval based approach,* 8th ASCE Spec. Conference on Probabilistic Mechanics and Structural Reliability, 2000, electronic text: http://ecivwww.cwru.edu/civil/rlm/P331.pdf

[7] NEUMAIER, A: *Interval Methods for Systems of Equations.* Cambridge University Press, Cambridge, 1990.

[8] RUMP, S., M.: *Intlab,* electronic text: http://www.ti3.tu-harburg.de/~rump/intlab/

[9] SEG_A, S., CIUPITU, L., REICH, S.: *Optimization of a spring balancing mechanism for parallelogram robot mechanisms.* In: 1st International Conference "Optimization of robots and Manipulators OPTIROB 2006". Predeal, Romania, 2006, pp. 69–74.

[10] ZHANG, H.: *Nondeterministic Linear Static Finite Element Analysis: An Interval Approach,* School of Civil and Environmental Engineering, Georgia Institute of Technology, 2005.

E. Toporcer – V. Hlavna – A. Kovalcik *

GASEOUS EMISSIONS OF A COMBINED COGENERATION UNIT

Problem of harmful gaseous emissions is solved in the paper in two ways. Firstly it is the design of a mathematical model of flow and combustion in a combustion chamber of an engine, which is a component of a combined cogeneration unit with a proposal of solutions enabling the decrease in amount of harmful gaseous emissions. Secondly it is the verification of the solutions through the computation by means of mathematical models considering these solutions.

1. Introduction

Cogeneration units operating as a part of energetic units of industry complexes adapt their operational mode to their needs [2]. Consequencies arising from that fact are often the increased environment loads through the increased formation of harmful gaseous emissions.

The problem of harmful gaseous emissions is solved in the paper in two ways. In the first place it is a proposal of the mathematical model of flow and combustion in an internal combustion engine, which is a part of a combined cogeneration unit with a proposal of solutions enabling the decrease in the amount of harmful gaseous emissions. Secondly, it is the verification of the mentioned solutions through the computation by means of mathematical models. Preparation of the CAD data is done in the CAD software CATIA 5, the mesh preparation in the preprocessor Gambit and the calculation itself and visualisation of results are done in the professional CFD (Computational Fluid Dynamics) software Fluent.

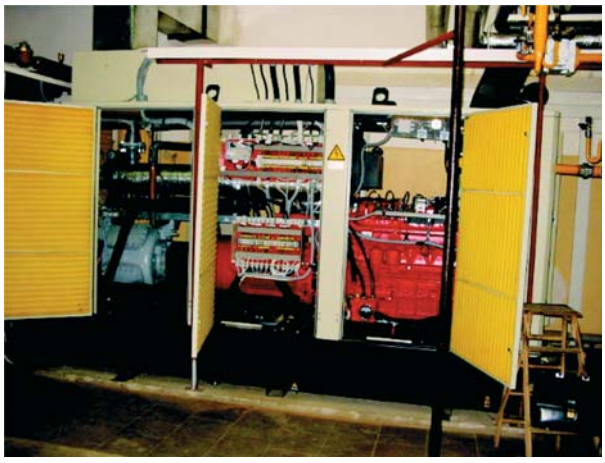

Fig. 1 Combined cogeneration unit

The experimental part of the paper deals with the measurement of harmful gaseous emissions of the combined cogeneration unit (see Fig. 1) operating in the technological process of a food processing plant.

2. NO_X emissions produced by the combined cogeneration unit

The combined cogeneration unit consists of a heat pump compressor, generator and natural gas fuelled combustion engine – Fig. 1. It operates in the energetic system of industry complex as the one of electric power sources and low-, central- and high potential heat sources.

The scheme of the measurement system is shown in Fig. 2. One part of the data is evaluated and recorded by the control system of the combined cogeneration unit as a subsystem of the controlling of the entire energetic system and the other one by the measurement device TESTO 300M. The probe of this analyzer takes an exhaust sample behind the heat exchanger for the exhaust gases cooling. The engine is running at the speed constant value of 1500 min^{-1}.

The comparison of the amount of NO_x emissions corresponding to the different operational modes characterised by the electric generator watt power value and connected or disconnected compressor of the heat pump (HP) (input 17 kW) is shown in Fig. 3. In the figure it can be seen that the measured combined cogeneration unit is optimised for production of minimum harmful gaseous

* **E. Toporcer, V. Hlavna, A. Kovalcik**
Department of Automotive Technology, Faculty of Mechanical Engineering, University of Zilina, Slovakia,
E-mail: emil.toporcer@fstroj.uniza.sk

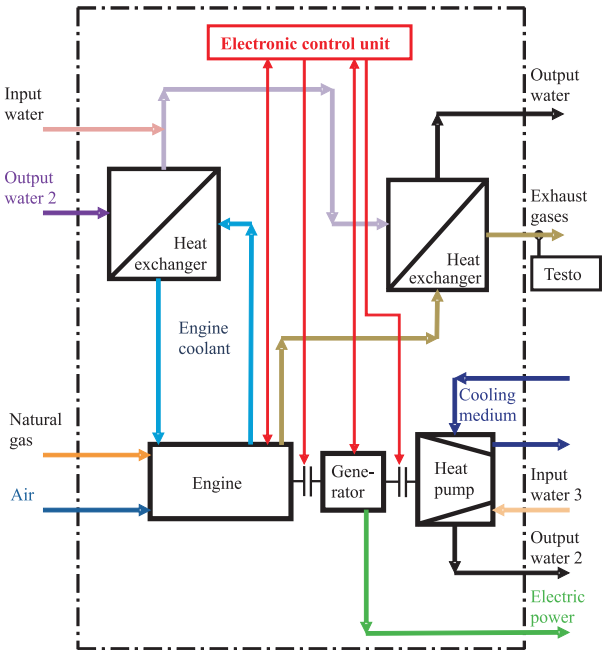

Fig. 2 Scheme of the measurement system

emissions in the main operational mode characterized by the electric generator watt power value of 36 kW and attached compressor of heat pump [7].

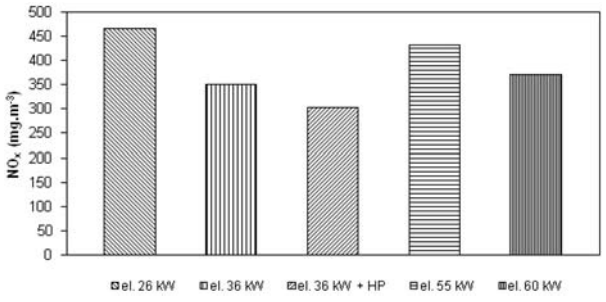

Fig. 3. NO_x emissions produced by the combined cogeneration unit operating at different modes

The cogeneration unit also works at other operational modes on the ground of adapting its running to the needs of the energetic complex, whose component it is. Consequently, the environment load is higher than it is in the case of running only at the main operational mode. From the experiments it results that the combined cogeneration unit meets the exhaust-emission regulations.

3. Mathematical modelling of flow and combustion

The continuity relation for one component α of the flowing medium at a chemical reaction has the following form:

$$\frac{\partial \rho_\alpha}{\partial t} + \nabla \cdot (\rho_\alpha \vec{u}) = \nabla \cdot \left[\rho D \nabla \left(\frac{\rho_\alpha}{\rho} \right) \right] + (\dot{\rho}_\alpha)_c , \quad (1)$$

where:
ρ_α – partial density of the component α,
D – diffusion coefficient,
$(\rho_\alpha)_c$ – speed of the change of the partial density of the component α by the chemical reactions influence, whereby

$$\rho = \sum_\alpha \rho_\alpha . \quad (2)$$

Momentum equation:

$$\frac{\partial \rho \vec{u}}{\partial t} + \nabla \cdot (\rho \vec{u}\,\vec{u}) = -\nabla p + \nabla \cdot \left(\mu \hat{\tau} + \lambda \hat{I} \nabla \cdot \vec{u} \right), \quad (3)$$

where:
μ – viscous coefficient,
λ – viscous coefficient,
$\hat{\tau}$ – viscous stress tensor,
$\hat{I}$ – unit tensor.

Energy equation:

$$\frac{\partial \rho I}{\partial t} + \nabla \cdot (\rho I \vec{u}) + p \nabla \cdot \vec{u} = \nabla \cdot K \nabla T + \frac{\mu}{2} \hat{\tau} : \hat{\tau} + \lambda (\nabla \cdot \vec{u})^2 + \dot{q}_c , \quad (4)$$

where:
I – specific internal energy,
K – mixture heat conductivity,
T – temperature,
$\dot{q}_c$ – heat release speed due to chemical reactions.

Continuity, momentum and energy equations in the case of moving mesh (u_g – mesh speed) have the form:

$$\frac{d}{dt} \int_V \rho_\alpha dV - \int_S \rho_\alpha (\vec{u}_g - \vec{u}) \cdot \vec{n} dS = \int_S \left(\frac{\rho D \vec{\nabla} \rho_\alpha}{\rho} \right) \cdot \vec{n} dS + \int_V (\dot{\rho}_\alpha)_c dV , \quad (5)$$

$$\frac{d}{dt} \int_V \rho \vec{u} dV - \int_S \rho \vec{u} (\vec{u}_g - \vec{u}) \cdot \vec{n} dS = \int_S p \vec{n} dS + \int_S \left(\mu \hat{\tau} + \lambda \hat{I} \vec{\nabla} \cdot \vec{u} \right) \cdot \vec{n} dS , \quad (6)$$

$$\frac{d}{dt} \int_V \rho I dV - \int_S \rho I (\vec{u}_g - \vec{u}) \cdot \vec{n} dS + \int_V p \vec{\nabla} \cdot \vec{u} dV = \int_S (K \vec{\nabla} T) \cdot \vec{n} dS + \int_V \left(\frac{\mu}{2} \hat{\tau} : \hat{\tau} + \lambda (\vec{\nabla} \cdot \vec{u})^2 + \dot{q}_c \right) dV , \quad (7)$$

where:
V – volume,
$\vec{n}$ – surface S normal vector.

In the professional CAD software CATIA V5 the space geometrical model corresponding to the geometry of the examined engine combustion chamber is created with regard to the needs resulting from the following use of simulation software Fluent 4.

As the calculation is done for the deforming mesh, it is needed to create geometrical models corresponding to single partial meshes, from which the resulting mesh is then created or between which it is then interpolated. Partial models are created for the combustion chamber shape from 340° crankangle up to 490° crankangle with the step of 10° crankangle. In term of the combustion monitoring it is sufficient to monitor the time sequence up to 410° crankangle, but in terms of flow monitoring the longer time sequence is simulated. Only one half of the combustion chamber is calculated because of the decrease in the demand on the used hardware. The computational mesh with defined boundary conditions is shown in Figure 4. The mesh corresponds to the value of 340° crankangle. Particular meshes have all the same definition of boundary conditions and mesh topology.

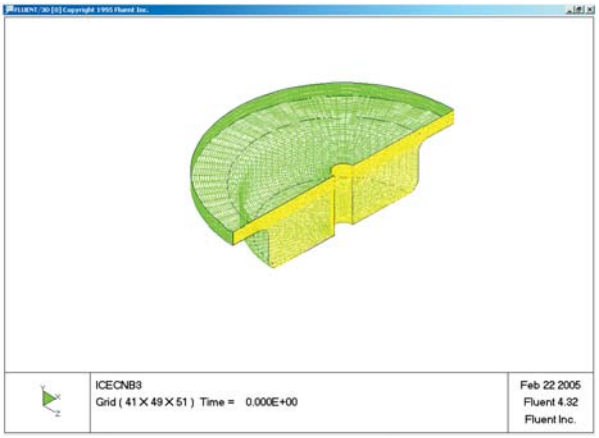

Fig. 4 Computational mesh with boundary conditions for the value of 340 °crankangle (green colour - wall, yellow colour - symmetry area)

From the combustion point of view the flame is calculated as kinetic in the turbulent mode and the problem is solved as unsteady. The mathematical model considers methane oxidation (through CO), dissociation of CO_2, N_2, O_2 and NO formation, altogether 7 equations:

$$2CH_4 + 3O_2 \rightarrow 2CO + 4H_2O$$
$$2CO + O_2 \rightarrow 2CO_2$$
$$2CO_2 \rightarrow 2CO + O_2$$
$$N_2 \rightarrow N + N$$
$$O_2 \rightarrow O + O$$
$$O_2 + N \rightarrow NO + O$$
$$N_2 + O \rightarrow NO + N.$$

Fig. 5 shows the progress of methane oxidation after the first time step. It is apparent that the combustion process started at the combustion chamber border instead of the combustion chamber centre, hence in the place of numerical initation. Gradually the flame spreads into the combustion space. There is only little methane in the combustion space after the fourth time step. The process of oxygen concentration decrease corresponds to the process of methane decrease.

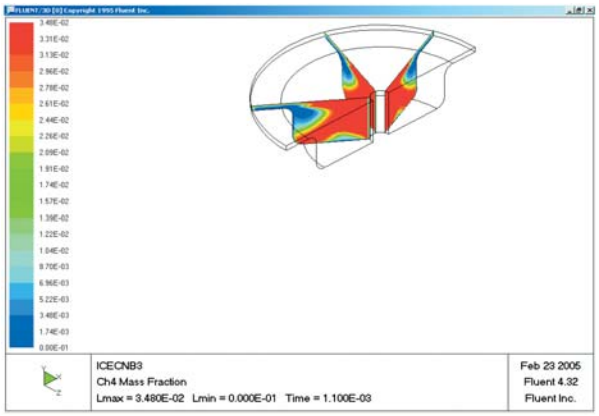

Fig. 5 Mass fraction of CH_4 in the time t = 0.0011 s

Figs. 6, 7, 8 and 9 illustrate the progress of NO concentration through the simulation.

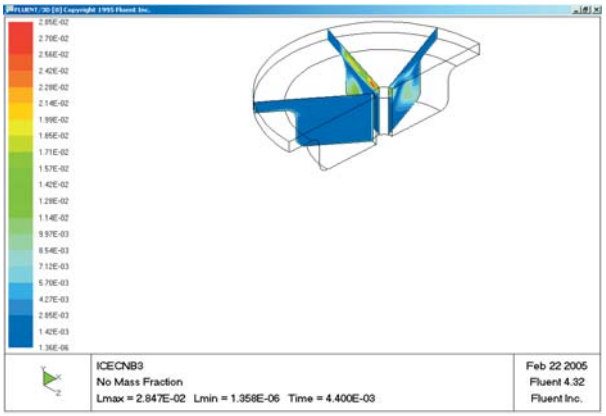

Fig. 6 Mass fraction of NO in the time t = 0.0044 s

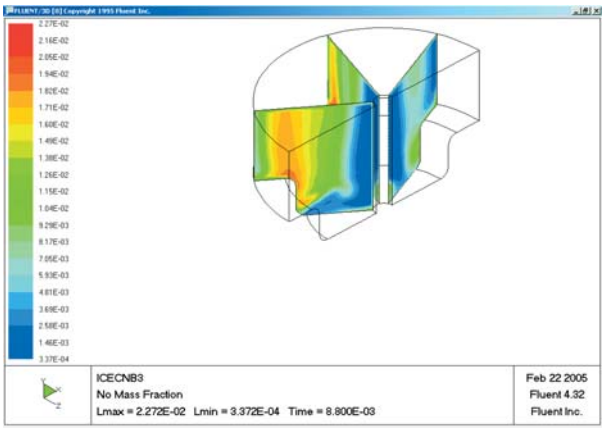

Fig. 7 Mass fraction of NO in the time t = 0.0088 s

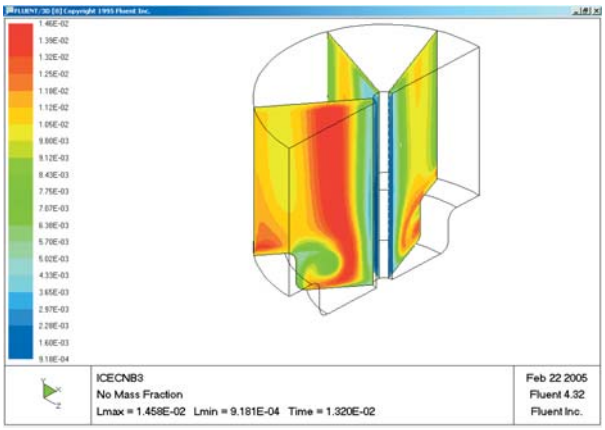

Fig. 8 Mass fraction of NO in the time t = 0.0132 s

Fig. 9 illustrates NO concentration in the last time step.

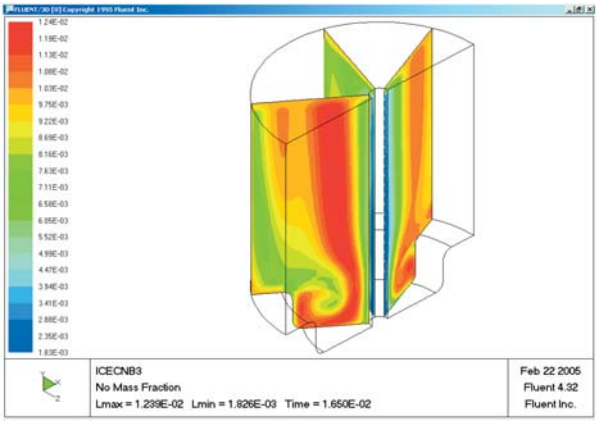

Fig. 9 Mass fraction of NO in the time t = 0.0165 s

Influence of the flow induced by the piston movement on the flow in the combustion chamber gradually increases. The highest values of flow velocity are obtained in the area of maximum change in the computational domain diameter.

The CO and NO concentrations differ from real values because of the inaccurate values used in the reactions definitions.

The experimentally found value of O_2 concentration in the exhaust gases for the main operational mode is 8.2 % vol., through the simulation found value is 3.9 % vol.

The experimentally found value of CO_2 concentration for the main operational mode is 7.3 % vol., through the simulation the calculated value is 11.7 % vol.

The value of calculated maximum combustion temperature is 2629 K.

A more accurate model can be obtained by the precision of boundary conditions, for example considering the influence of heat transfer into the combustion chamber walls, using more suitable reactions, more accurate definition of chemical reactions (activation energy, preexponential factor), the temperature dependent specific heat etc.

In relation to the differences between the simulation and experimental results it is to be noted that the calculated values are considered inside the combustion chamber for the value of 490° crankangle, i.e. the expansion stroke so far not finished (because of the capacity of used hardware) and the experimental values are evaluated by the probe placed after the exhaust exchanger.

3. Solutions proposal

For the decrease in NOx concentration being the most critical harmful pollutant, two ways were used and verified by a simulation:

1. the combustion temperature decrease through the intercooler of compressed air (decrease in the temperature mixture of about 20 °C),
2. the combustion temperature decrease through the intercooler of compressed air (decrease in the temperature mixture of about 20 °C) and simultaneously through the recirculation of 20 % of exhaust gases.

The combustion temperature decrease through the intercooler results in the maximal combustion temperature of 2484 K (about 145 K lower than in the previous calculation) achieved in the third time step similarly as in the previous calculation, i.e. in the time of 0.0033 s after the initiation. The assumption of the maximum combustion temperature decrease through the intercooler is verified. NO concentration for the whole combustion space is about 12.6 % lower than in the case without the intercooler.

The combustion temperature decrease through the intercooler and simultaneously the recirculation of 20 % of exhaust gases results in the maximum combustion temperature of 2485 K (about 1 K higher than in the previous calculation – with an intercooler) again achieved in the third time step similarly as in the previous calculation, i.e. in the time of 0.0033 s after the initiation. NO concentration for the whole combustion chamber is about 76.9 % lower than in the case without the intercooler.

4. Conclusion

For the cogeneration units operating as a part of advanced energy unit there is a need to adjust their current operational mode to the mode required by cooperated or superior devices. This can result in higher environment loads [5]. The used mathematical model of a harmful gaseous emissions formation has the potential to optimize the whole energetic unit from the ecological point of view.

References

[1] A. ELSAFTY and A. J. AI – DAINI: *A parametric study of vapor absorption air – conditioning system soe,* Coventry University, Coventry, 2003

[2] HLAVNA, V. et al.: *A non-conventional energetic unit,* EDIS, University of Zilina, 2008

[3] CHALAMONSKI, M.: *Analysis of thermal centre failuring,* Eksploatacja i niezawodnosc, Nr. 4(36)/2007, ISSN 1507-2711

[4] KONDEPUD, D.: *Modern thermodynamics,* John Wiley and Sons, 1998

[5] SOJCAK, D.: *A combustion engine with a non-conventional cooling circuit*, SjF, University of Zilina, 2006

[6] ŞENCAN, A., YAKUT, A., DIKMEN, E.: *New model for determining the thermodynamic properties of libr-h2o solution,* G.U. Journal of Science 17(1):101-110 – 2004, ISSN 1303-9709

[7] TOPORCER, E.: *Ecological problems of a gas engine in a cogeneration,* SjF, University of Zilina, 2007

[8] YASUO TAKAGI, TADASHI NAKAMARU, YOSHIHIKO NISHITANI: *An absorbtion chiller models for HVACSIM,* Toshiba Corporation, Fuchu City Toshiba Japan, Sanko kucho, Nagoya Japan, 2004.

Lubos Kucera – Michal Lulac – Ladislav Jurak – Frantisek Brumercik *

HYDROMECHANICAL AUTOMATIC TRANSMISSION

This contribution describes some tests of hydromechanical infinitely variable transmission (IVT) on a test stand. Further, there is described a truck with installed IVT and tests of this IVT at real conditions. There is also shown a control system of the IVT.

1. Introduction

Some parts of research activity at the Department of design and machine elements are oriented on gears, gearboxes, elements of gears and also on hydraulic gear based on torque converter and hydrostatic gear in parallel and combined connection, where the power flow is split to two or more branches. There was a test stand designed for the whole transmission contained combustion engine, the front-end and tandem gearbox and other parts.

The laboratory was already used for hydromechanical gearboxes tests before, e. g. for the new Zetor tractor gearbox with Powershuttle and Powershift and the IVT 150 gearbox for special mobile machines, SUV vehicles and trucks. The experimental tests of IVT 150 were made to describe different working modes with manual electronic regulation without any automatic control system. The deal of this regulation was to achieve the maximally efficiency of the transmission.

2. IVT Principle and Test Stand Measurement

The basic principle of the IVT 150 transmission is the usage of the torque converter in the parallel connection with differential hydrostatic gear with differential at the output (Fig. 1).

This principle allows to design a product that has satisfactory efficiency at the whole drive mode scope. The idea was to develop the gearbox through an innovative approach regarding the actual knowledge base [1].

After the kinematic scheme definition and documentation preparation, the first prototype was built. The IVT placed on the test stand is pictured in Fig. 2.

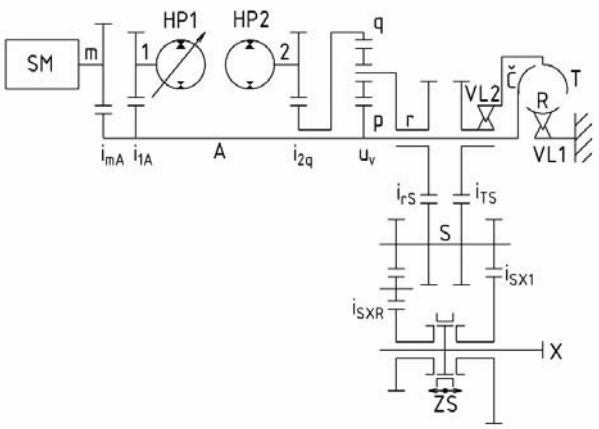

Fig. 1. IVT - Kinematic scheme of the transmission

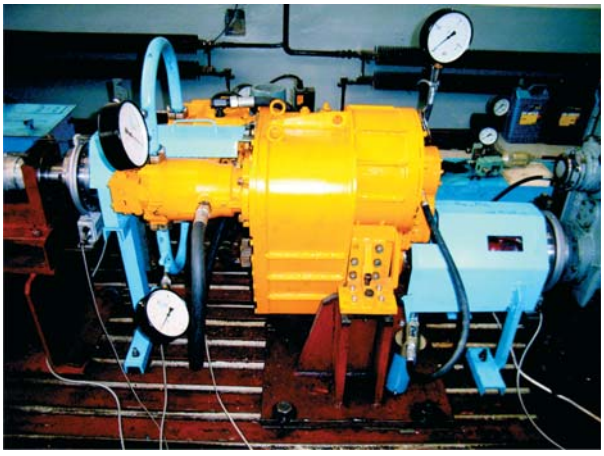

Fig. 2. Gearbox at the test stand

* **Lubos Kucera, Michal Lukac, Ladislav Jurak, Frantisek Brumercik**
Department of Design and Machine Elements, Faculty of Mechanical Engineering, University of Zilina, Slovakia,
E-mail: lubos.kucera@fstroj.uniza.sk

By vehicle acceleration from zero velocity, the maximum power is transmitted by the torque converter and small power is transmitted by the hydrostatic gear. This applies to gear ratio $i_{AX} = (\infty;5)$ if

$$i_{AX} = n_{CE}/n_{OUT}, \quad (1)$$

where
n_{CE} – RPM of the combustion engine
n_{OUT} – RPM of the output shaft of IVT 150.

While $i_{AX} = (5; 1.28)$, maximum power is transmitted by differential hydrostatic gear, the output shaft of the torque converter across freewheel does not transmit any power. The control system has to work especially at these two modes so the efficiency of the transmission gets the highest value.

The results from these measurements defined some possibilities how to control the gear ratio of the hydrostatic gear. This hydrostatic gear is operated by the electrohydraulic servovalve type MOOG. Electric current in the valve is directly proportional to the gear ratio (Fig.3).

Fig. 3 also represents the relation between the gear ratio and the current from 0 to 100 mA in regard to the displacement of the hydrostatic pump (HP1) regulation plate from −1 to +1 at maximum transmission efficiency.

This regulation curve is the base for the first design of a control system for gear change. This transmission control system needs the rpm sensor of the engine and the output shaft and the position sensor of the fuel rod. It needs neither a pressure sensor at hydrostatic gear nor a torque sensor.

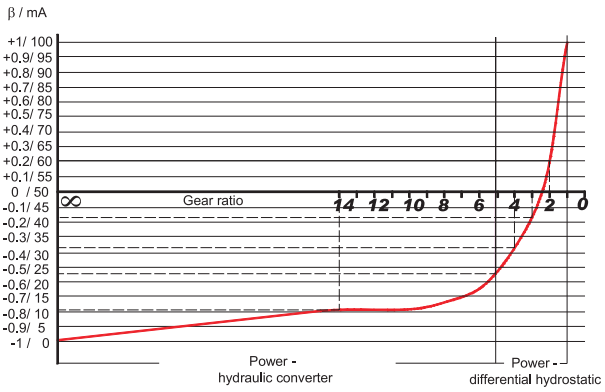

Fig. 3 Regulation curve and the current – gear ratio relation of the IVT

3. Test Truck

Installing the IVT 150 to a suitable vehicle was one of the alternatives of the transmission test at real conditions. The input shaft of the IVT 150 needs to turn counterclockwise, maximum width of the variator is 700 mm and max. length is 960 mm. For these parameters, there was suitable an old vehicle – the Praga S5T truck, model year 1969. Its engine shaft is turning counterclockwise and the gear ratio of the fourth speed in the 4 – step manually Praga gearbox is −0,98 (according to the ratio of the test stand front-end gearbox).

The frame of the vehicle contains the Praga T912 engine. The engine parameters can be successfully simulated by the CFD analysis to obtain data for the mathematical simulation model based on Matlab Simulink platform [2]. Original is also the clutch and the 4-step gear-box working on the fourth gear only. The IVT 150 prototype was installed to the vehicle frame replacing the original propeller shaft. This solution represents the cheapest possibility how to test the IVT 150 in a vehicle with different control systems at real conditions.

Fig. 4 represents the frame of the Praga truck with the new IVT gearbox installed and Fig.5 gives the view of the overhauled truck after the first drive.

Fig. 4. The IVT 150 installed to the truck frame

Fig.5. Praga S5T - IVT test truck after the first drive

4. IVT Control system

The transmission control system contains a laptop, power electronic equipment, rpm sensors, position sensor of the fuel rod, oil temperature sensors, pressure sensors and sensor of the regulated hydraulic pump plate displacement. Data from the sensors and other parameters are recorded during the drive to the control computer. Fig. 6 represents the scheme of the control system working in the real time and developed in the Matlab Simulink Realtime toolbox.

By the first drive the truck diagnostic data recording was done. In Fig. 7 there is a data log, where:

- the red color represents RPM of the engine (scale 1:1),
- the green color represents RPM of the output shaft (scale 1:1),
- the brown color represents gear ratio i_{AX} (scale 100:1)
- the blue color represents position β of the hydraulic pump regulation plate (scale 1000:1).

The results show the continuously gear change, resp. the continuously acceleration of the vehicle by different RPMs of the combustion engine dependent on the fuel rod placement.

ACKNOWLEDGEMENT

This contribution is supported by the following projects:

- Intelligent control systems of combined power flow variable differential transmissions – VEGA 1/0577/08
- Energy balance of differential power transmissions – VEGA 1/0779/08
- Hydromechanical "IVT 150" – Infinitely Variable Transmission development and production for SUV and mobile working machines until 150 kW – AV 4/0031/07.
- Research of kinematic a dynamic properties of runflat tyres and platform vehicle parts using the simulation – VEGA 1/3208/06

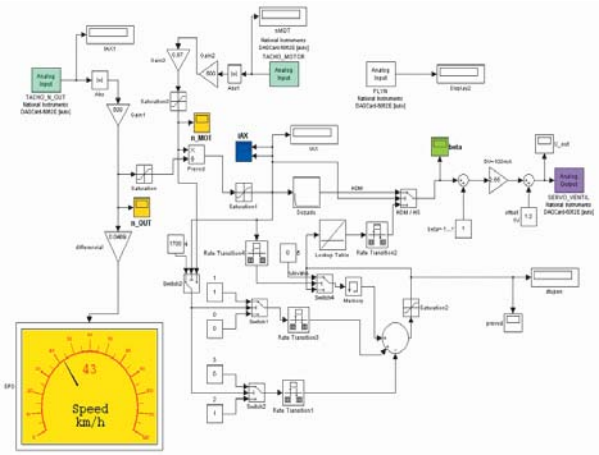

Fig. 6. View on the control panel

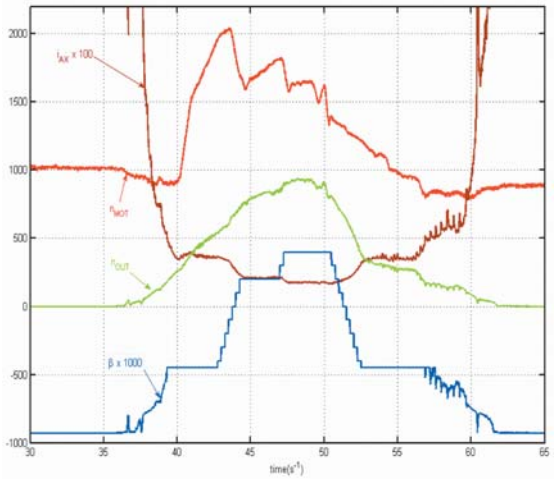

Fig. 7 Data log of the truck test

References

[1] MASIN, I. – SEVCIK, L.: *Innovation Engineering Methods. Product Innovation, Planning and Design (in Czech)*, Institute of technology and management, Liberec 2006, p. 184, ISBN 80-903533-0-4.

[2] SOJCAK, D.: *Stirling Engine and a Simulation Possibility of its Basic Parameters by CFD*, FIK – Stirling 2007, 1-st collective volume, Zilina, ISBN 978-80-8070-788-0

Bojan Cene *

STRAY CURRENTS ON DIRECT – CURRENT RAILWAYS IN SLOVENIA

DC stray currents are currents which do not flow through designed conductors but along the path of least resistance. These currents are very harmful to various metallic structures and lead to corrosion in the long term. The most significant sources of DC stray currents in Slovenia can be found in electrified railways using the direct current system of 3000 V. Not all the return current can flow back to the rectifier substation through the rails but a high percentage of this current is dispersed in the earth, depending on conductive arteries. In some cases, these stray currents even cross a very winding railway line.

The Slovenian Railways have electrified a substantial part of their railway lines using the direct current system of 3000 V. The complete 3000 V direct current overhead line system in Slovenia is being fed by 18 rectifier substations (ENP).

Key words: DC stray currents, electric traction, rails, rectifier stations, road metal, locomotives

1. Introduction

DC stray currents in the earth cause damage to metal structures. The possible sources of these currents in the earth are the following installations:

1. DC operated railways where rails are used as return conductors,
2. earthed DC installations with an operated circuit, earthed in several points.

Such installations are:

- overhead trolleybus networks with one pole earthed in several points or with one pole more than once connected to the return conductor of the tram network (rails),
- DC networks and DC industrial installations,
- DC telecommunication networks,
- Installations for protection against corrosion.

Installations, buried in the earth which are imperilled by DC stray currents, are:

1. metal pipelines,
2. metal cisterns,
3. metal constructions and concrete reinforcement
4 armoured cables,
5. earthings of power and telecommunication installations.

Electrified railways, operating in DC system of 3000 V where the total current flows through the return conductor (rail) are at present the main source of DC stray currents in Slovenia.

Return currents amount up to 2400 A depending on the number of consumers (electric locomotives).

2. Calculation of stray currents on DC railways of 3000 V

In electric traction of 3000 V the traction vehicle receives its power supply from the rectifier substation through the overhead contact system (contact line). The circuit is closed through the electric locomotive and the rails back to ENP as shown in Fig. 1.

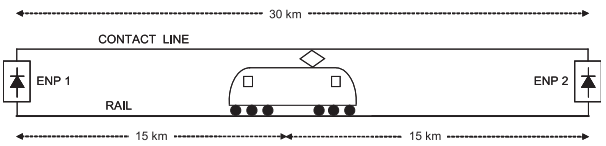

Fig. 1 Operating circuit of the electric traction vehicle

All ENP of Slovenian Railways operate in parallel, which means a two-way supply of the traction vehicle, which can be seen in Fig. 1. Consequently, the return current flows through the return rail back to ENP in both directions, to ENP 1 and to ENP 2. As the locomotive approaches ENP 2, the load of ENP 1 decreases. When the electric traction vehicle is very close to ENP 2, a minimal return current is still flowing in the direction of ENP 1.

One-way supply of the electric traction vehicle on Slovenian railways exists only at the exit of our electric traction system to the neighbouring countries, which use single-phase AC systems of electric traction (Austria and Croatia), and during accidental outages of ENP or during maintenance works.

Rails are laid over wooden or concrete sleepers on the road metal and represent at the same time the earthing electrode of the

* **Bojan Cene**
Ministry for Traffic, Ljubljana, Slovenija
E-mail: bojan.cene@gmail.com

operational circuit of electric traction of the DC system of 3000 V, which can be seen in Fig. 2.

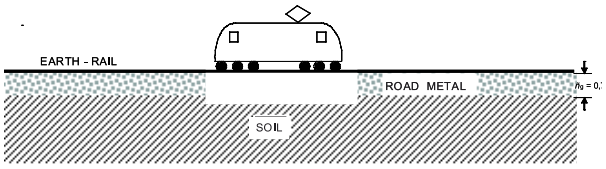

Fig. 2 Earthing of the operational circuit of electric traction

As can be seen in the figure, the rails are placed on a road metal, which is on average 0.7 m high. The road metal is spread on soil. This means the earthing electrode lies on non-homogeneous soil, whereby the road metal has a higher specific ohmic resistance than the soil. In that case, the earthing resistance of the total earthing system is calculated according to equation [1]:

$$R_o = \frac{\rho_g \cdot h_g}{D^2 \cdot \frac{\pi}{4}} + \frac{\rho_z}{2 \cdot D} \quad (\Omega) \tag{1}$$

where:
R_o is the earthing resistance of the rail in Ω,
ρ_g is the specific resistance of crushed stone in Ωm,
h_g is the height of road metal in m,
D is the diameter of earthing electrode in m,
ρ_z is the specific earth resistance in Ωm.

The earth electrode – rails, which represents a strip-type earth conductor, consist of two or more strips – the rails. Since the distance between the two strips – the rails is smaller than 5 % of the length of rails, the following equation is valid for calculating the diameter of the equivalent plate [1]:

$$D = 1.13 \cdot \sqrt{S} \quad (\text{m}) \tag{2}$$

S is the surface of earth electrode – rails, in m^2

The surface of the earth electrode – rails is calculated according to the following equation [2]:

$$S = a \cdot (n \cdot b) \quad (\text{m}^2) \tag{3}$$

where:
n is the number of rails (2 rails for a single track line),
a length of rails in m
b width of rail base = 0.125 m

Specific resistance of earthing electrode – rails per unit of length is calculated according to the following equation [3]:

$$R_t = \frac{\rho_t \cdot L}{2 \cdot m \cdot A} \quad (\Omega) \tag{4}$$

where:
ρ_t is the specific resistance of rails = 0.20 $\Omega\text{mm}^2/\text{m}$,
R_t is the specific resistance of earthing electrode – rails per unit of length in Ω/km,
L is the length of earthing electrode – rails in m
m is the number of tracks,
A is the cross-section of one rail = 6250 mm^2.

From the known specific resistance of the earth electrode – the rails, and from the known earthing resistance of the rails, the amount of stray currents outside the return conductor – the rails, can be calculated according to the following equation [3]:

$$I_b = I_t \cdot \left(\frac{R_t}{R_t + R_o} \right) \quad (\%) \tag{5}$$

where:
I_b is stray current in %
I_t is the current in the rails in %

Let us take an example of a single track line where the electric traction vehicle is located in the middle of the section between both ENP (Fig. 1). In this case, the same amount of return current is flowing towards ENP 1 and towards ENP 2, which means that both ENP are equally loaded.

Suppose there is a very well maintained road metal with a specific resistance of 5000 Ωm, which is laid on clay with a specific resistance of 50 Ωm. The calculation gives the following results:

- the surface of the earthing electrode – the rails of a single line track is 7500 m^2,
- the diameter of the equivalent circular earthing electrode is 98 m,
- the specific resistance of rails over a distance of 30km is 0.48 Ω/30km,
- earthing resistance of the earthing electrode – the rails is 0.7 Ω,
- the amount of stray currents is 41 %

It can be seen from the result that from the total current load of the electric traction vehicle, 59 % of the current flows through the rails and 41 % of the current is dispersed into the earth and then returns to the ENP along the paths of highest conductivity (pipelines, ...).

However, the amount of 41 % is divided into two parts, one flowing towards ENP 1 and the other part towards ENP 2, which means that in the direction of one ENP there flows a stray current of only around 20 % of the total current. The loading current of the new 6 MW locomotive amounts to around 2000 A at full load, which means that in the directions of both ENP, 200 A of current is dissipated in the ground. But it is clear that this partition of stray currents is possible only at the moment when both ENP carry the same load. The more we are approaching ENP 2 the less current is flowing to ENP 1. As a consequence, ENP to which the electric traction vehicle is nearer is heavier loaded. But due to the shorter distance the amount of stray currents is lower. Less and less current is flowing towards the more distant ENP. The amount of stray currents is increasing but this amount is very small with regard to the minimal current in the rails.

Hence it follows that the highest stray currents arise in the system of Slovenian railways, when the electric traction vehicle operates in the middle of the railway section between two ENP.

In the case of a double-track railway line having the same parameters of both the road metal and the basic earth as in a single-track line there are 38 % of stray currents outside the rails. Due to a greater number of rails in a double-track line the percentage of stray currents is lower.

Therefore, the actual amount of stray currents depends on the distance between the electric traction vehicle from the ENP and properties of the road metal and the earth.

Fig. 3 shows the amount of stray currents for a single-track and a double-track electrified railway line with a specific resistance of the road metal of 5000 Ωm and a specific resistance of the earth of 50 Ωm.

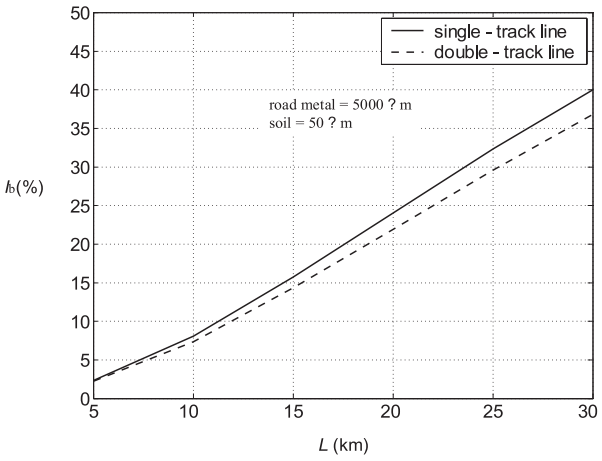

Fig. 3 The amount of stray currents in a direct current railway line at 3000 V with a specific crushed stone resistance of 5000 Ωm and a specific earth resistance of 50 Ωm

It can be seen from Fig. 3 that with a growing distance between the electric traction vehicle and ENP the percentage of stray currents flowing through the road metal and the earth is increasing. At a distance of 20 km from ENP, the percentage of stray currents amounts to around 24 % on a single-track line and to around 22 % on a double-track line.

Fig. 4 shows the percentage of stray currents which is owing to higher earth resistance of 100 Ωm significantly lower and amounts to around 19 % in a single-track line at a distance of 20 km from ENP, and to around 17 % in a double-track line.

Figures 5 and 6 show the percentage of stray currents for earth of high specific resistance. In this case, the amount of stray currents is minimal.

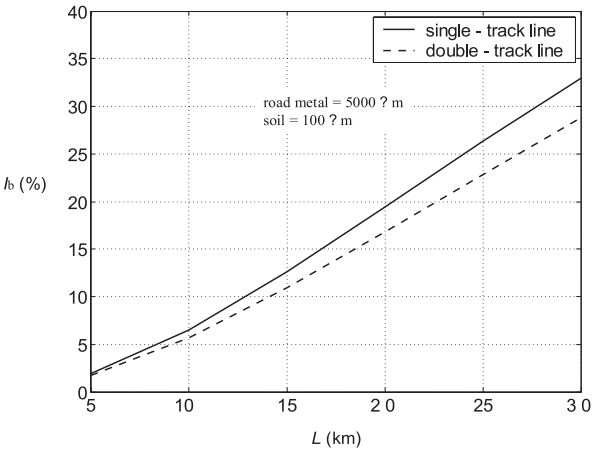

Fig. 4 The amount of stray currents in direct current railway at 3000 V with specific ballast resistance of 5000 Ωm and specific earth resistance of 100 Ωm

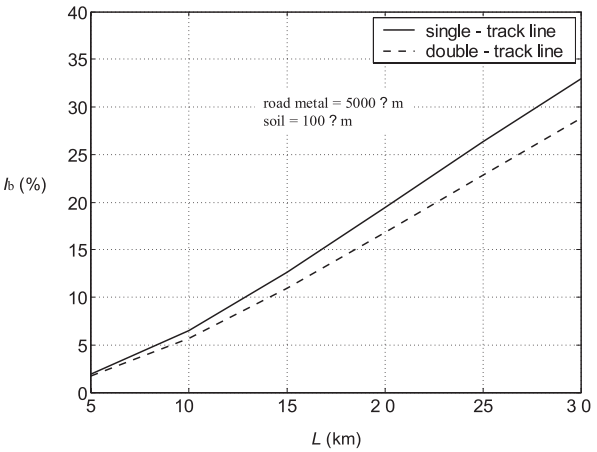

Fig. 5 The amount of stray currents in direct current railway at 3000 V with specific crushed stone resistance of 5000 Ωm and specific ground resistance of 500 Ωm

3. Calculation of stray currents in direct current railway of 3000V with the aid of the telegraphic equation

The amount of stray currents in direct current railways can also be calculated according to the following equation [4]:

$$I_b = I \cdot \left[1 - \sqrt{1 - th \cdot \left(\frac{\alpha \cdot L_t}{2}\right)}\right] \quad (\%) \qquad (6)$$

where:

I_b is the maximal value of stray currents in %,
I is 100 % = the total current (current in the rail + stray current),
th is tan hyperbolic,
L_t is the distance between the traction vehicle and ENP (km),
α is suppression factor of earth electrode – rails (km^{-1})

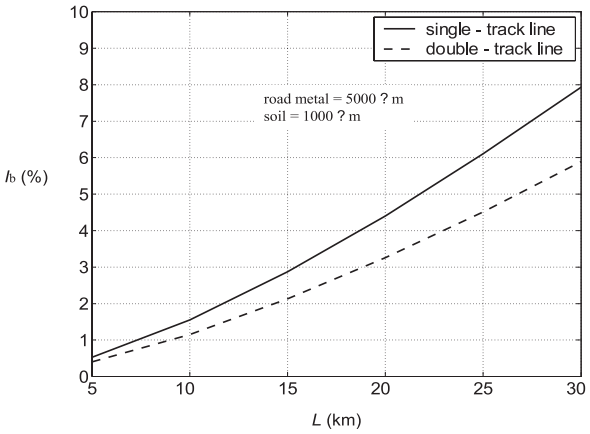

Fig. 6 The amount of stray currents in direct current railway at 3000 V with specific crushed stone resistance of 5000 Ωm and specific earth resistance of 1000 Ωm

The equation for the suppression factor in direct current is derived from the following equation used for the constant of propagation of travelling waves in direct current [5]:

$$\underline{\gamma} = \alpha + j\beta = \sqrt{(R + j\omega L)\cdot(G + j\omega C)} \qquad (7)$$

where:
γ is propagation constant,
β is rotation constant,
L is inductivity,
C is capacity.

As there is no frequency in direct current, all the elements, except for resistance and conductivity, are omitted in the equation above. Thus, we arrive at the equation for the suppression factor of the straight-lined earthing electrode – the rails:

$$\alpha = \sqrt{G \cdot R_t} \ (\mathrm{km}^{-1}) \qquad (8)$$

where:
G is the transversal conductance of the railway in S/km.

The transversal conductance of the railway is usually in the range from 0.1 S/km and 5 S/km [3]. The cleaner the road metal and the smaller conductivity of the basic earth are, the lower the transversal conductance is. If there are very soiled and chemical-soaked substratum and the basic earth of good conductivity, then the transversal conductance can be higher than 5 S/km. Let us consider the case of a single-track electrified railway where the electric traction vehicle is positioned at the middle of the railway section between two ENP (Fig. 1). Due to the fact that the return current is closed from the traction vehicle towards each ENP, the total length of the earthing electrode – the rails is 30km. First of all, we have to calculate the suppression factor of the straight-lined earthing electrode – the rails according to equation 8, where it is supposed that the conductance of tracks is 0.1 S/km and the resistance of rails is 0.016Ω/km:

$$\alpha = \sqrt{0.1 \cdot 0.48} = 0.04 \ \mathrm{km}^{-1}$$

The percentage of stray currents in the earth is calculated according to equation 6:

$$I_b = 100 \cdot \left(1 - \sqrt{1 - th \cdot \frac{0.04 \cdot 30}{2}}\right) = 53.7\,\%$$

The result indicates that 53.7 % of the return current flows back to the ENP through the earth and not through the rails instead. Since the supply of the traction vehicle is from two sides, one half of these currents is divided between both ENP.

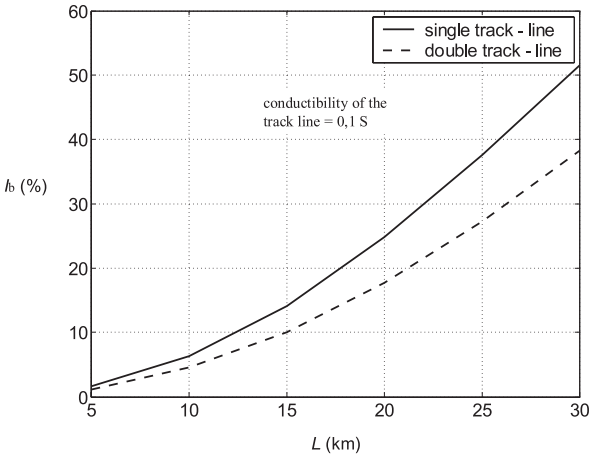

Fig. 7 The amount of stray currents in DC railway at 3000 V and the railway track conductivity of 0.1 S

It can be seen in Fig. 7 that for the railway conductivity of 0.1 S at a distance of 20 km from the ENP on a single track railway, around 25 % of the stray currents will flow outside the rails, and around 18 % on a double track railway line.

4. Simulation of stray currents in the Simulink program

By means of the Matlab-Simulink program a very accurate simulation of DC stray currents can be carried out for a DC railway line using the following parameters [2]:

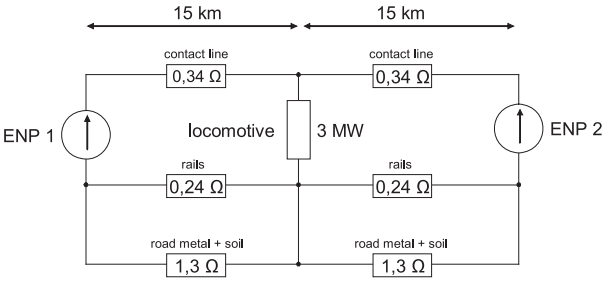

Fig. 8 Substitutional resistance model of single-track railway line

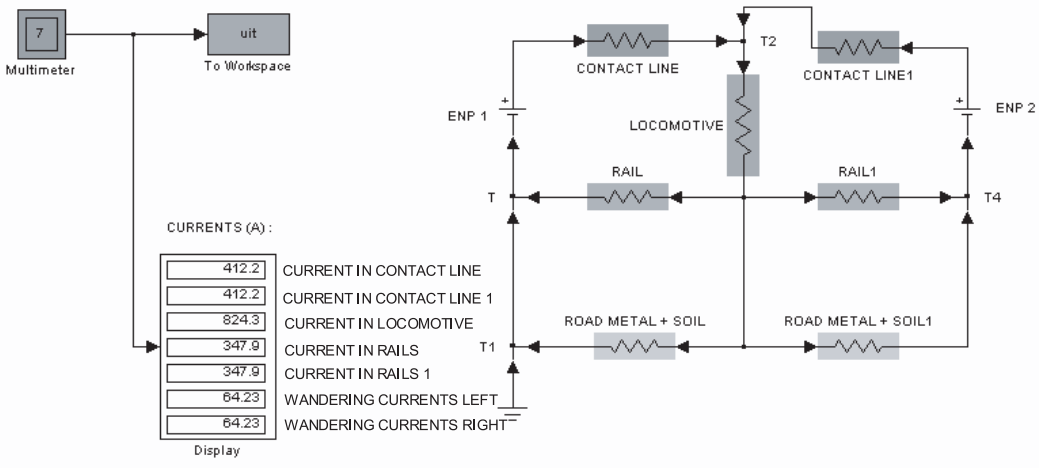

Fig. 9 Simulation scheme of stray currents on a DC railway in Simulink

- the distance between two ENP is 30 km,
- the electric traction vehicle is positioned in the middle of the line section between both ENP,
- the power rating of the electric traction vehicle is 3 MW,
- the specific earth resistance is 50 Ωm,
- the railway is a single-track line.

The substitutional resistance model of the single-track railway line based on calculations from Chapter 2, is shown in Fig. 8 [2]:

After performing the simulation the shown results are obtained on the simulation scheme in Fig. 9 [2]:

The total load current of the traction vehicle is 824.3 A. The current of 347.9 A returns to ENP 1 and ENP 2 through rails, and 64.23 A through road metal and the earth. Total stray currents to ENP 1 and ENP 2 amount to around 20 % over a distance of 15 km, which means 40% for the total distance of 30 km.

5. Conclusion

The paper presents an analysis of DC stray currents in direct current railways in Slovenia in three different ways. It is obvious that the results match considerably well. In addition to calculations and simulations, the measurements of DC stray currents are also possible:

- current measurements and
- measurements of the potential

However, owing to the dynamics of the electric traction, the measurements yield completely unreliable results. The loading current of the electric locomotive is varying at any given moment, depending on the profile of the track, the speed, etc. But on the other hand, the measurements represent a considerable cost, and owing to this fact, the measurements of this kind have never been carried out in Slovenia.

As a final result, the calculation is thoroughly satisfying for the analysis of stray currents in direct current railways. Due to varying values of ohmic resistances of earth and road metal over a long distance, the calculations can never produce exact results. However, these calculations are very useful for the design of electrified railways employing direct current system of 3000 V. The mutual distance between two rectifier stations in new installations should be no more than 15 km, which results in a considerable decrease in stray currents. The average distance between rectifier stations is 30 km in Slovenia now. Therefore, the Slovenian railways represent the greatest threat to different metal structures in the country.

References

[1] KOCH, W.: *Grounds of Electrical Sevices under Tension above 1 kV - number 2 (in German),* Verlag Julius Springer, Berlin-Gottingen-Heidelberg, 1955.
[2] CENE, B.: *Modernization of Electric Traction on Slovene Railways (in Slovene)* Master's work, Fakulteta za elektotehniko Maribor, 2004.
[3] CURK, F.: *Problems of One-way Shaking Currents - I. part (in Slovene)*, Elektroinstitut Milan Vidmar, Ref. st. 594, Ljubljana, 1973.
[4] CENE, B.: *Stray Currents on One-way Railway 3000 V (in Slovene)*, Individually research work, Fakulteta za elektotehniko Maribor, 2004.
[5] VORSIC, J., PIHLER, J.: *Technology of High Tension (in Slovene)*, Fakulteta za elektotehniko Maribor, 1997.

Tomas Lack – Juraj Gerlici *

RAILWAY WHEEL AND RAIL ROUGHNESS ANALYSIS

The paper deals with the railway wheel unroundness (out-of-round) analysis and with the rail head roughness analysis. Roughness of the running surfaces is the predominant source of noise of rail bound transport systems today. Reliable measurements of the roughness of rails and wheels are crucial for noise reduction purposes. In the past, the main purpose of measurements was the understanding of corrugation growth and rolling noise generation. Meanwhile, quantitative descriptions have gained considerable importance.

Key words: out-of-round, rail roughness, butterfly method, one-third octave analysis

1. Introduction

In general, wherever the rolling of one body surface over another body surface occurs, there the noise is generated. In the case when the surfaces of bodies which are in contact are smooth enough or if the rolling is slow enough, the level of the noise may be so low as if the rolling were noiseless. The noise which is conducted through the air is not caused only by rolling. Rolling members and the track surface on which the rolling occurs cause vibrations different from those which are responsible for the noise which is led through the air. They might be expressed in two ways. On one side are vibrations and noise in a vehicle supported by rotating members (wheels). This noise may be a component of a big part of vibrations which go through suspensions and construction of the vehicle and occur in the vehicle body as a repeatedly emitted noise. This increases the noise coming more directly through the air. On the other hand, the vibrations, which are generated on the track surface, on which the wheels roll, might be transmitted into and through the construction and the subsoil which support them.

2. Noise and vibration sources

The accompanying phenomenon of whichever transport system operation is noise and vibrations. The railway operation is not an exception. The generated noise very often reaches such a level of parameters which is not possible, from the point of view of surroundings in which the railway is situated, to be ignored or its negative influence cannot be underestimated. The main parameters which have the influence on the noise level are the following ones [3]:

The temperature of the rail may change in accordance to the air temperature as a result of thermal radiation it may have an influence on the temperature of subsoil and on the stiffness and damping of subsoil.

Parameters which have influence on the noise level Tab. 1

Rail type	Distance of internal wheels faces
Static stiffness of the subsoil	Track gauge
Quotient of subsoil damping	**Wheels tread surface roughness**
Sleepers type	**Roughness of not corrugated rail head surface**
Distance of sleepers	Velocity of a train
Gravel ballast stiffness	Wheel force
Quotient of the gravel ballast damping	Air temperature

The European norm prEN ISO 3095 [5] specifies conditions for the obtaining of results which are to be described and compared. The results concern the level and spectrum of noise which is emitted by all kinds of vehicles which operate on tracks or other types of rigid track with the exception of track maintenance machines in operation.

The results might be used for the characteristics of noise emitted by these vehicles during type and inspections tests and for the comparison of noise emissions of various vehicle types on specific parts of a track.

In accordance to the presented issues in the following text, the emphasis will be placed on the wheel un-roundness and rail unevenness. The noise which occurs as a result of rolling (and others processes) is characterised with the help of its level and spectrum.

* **Tomas Lack, Juraj Gerlici**
Faculty of Mechanical Engineering. University of Zilina, Zilina, Slovakia, E-mail: tomas.lack@fstroj.uniza.sk

The noise level caused by the rolling: in general there are two known parameters which have a direct influence on the noise level when rolling:
- faster process of rolling, higher level of noise,
- more rough surface in contact, higher level of noise.

In the case of railway wheel rolling over the rail, the influence of surface roughness of bodies in contact is mainly expressed.

3. Roughness of the rail head surface

The most prominent cause of higher roughness is a corrugated or waved track, which was created in the longitudinal direction during the railway operation.

The influenced place on the rail is very often irregular, its length may change from several tens of millimetres up to hundreds of millimetres and the maximum depth of the groove reaches tens of microns.

When the surface of the rail is smooth (where the depth of the groove is smaller than 10 microns), roughness of surfaces participates only in a small extent in the overall level of noise, which is determined mainly by the type of vehicles in operation. When the level of wrinkles is very low, the surrounding noise (measured in a distance of 25 m from the track) of vehicles which are braked by the block brake [5] is higher than vehicles which are braked by the disc brake at about 10 dB.

The level of noise when increasing the level of wrinkles for disc brakes increases faster than for the vehicles with block brakes. When the wrinkles of track reach a certain value from the point of view of noise level, there is no difference between separate types of vehicles. So far there have not been efforts for the quantification of critical wrinkles. Wrinkles occur in many different forms and so far it has not been stated which form or which forms participate in the noise increase and to which extent.

Roughness is the root mean square value (RMS) of the rail running tread change size in the direction of the movement (longitudinal level) measured along the rail, expressed in μm.

Level of the roughness is the level in dB determined by the following equation:

$$L_r = 20 \cdot \log\left(\frac{r}{r_0}\right)^2 \quad \text{dB} \qquad (1)$$

where:
L_r is the level of the roughness,
r is root mean square roughness amplitude,
$r_0 = 1\mu m$ is reference roughness.

When measuring the vehicle or train noise, the conditions which from the point of view of the rail head surface and vehicle wheels have to be met, offer an acceptable influenced final image of the complete evaluation of the vehicle noise. These conditions lay in the values quantification of rail head surface unevenness (and wheels) and in specification of limit values under which the measurement of noise is acceptable. (Notice: For conventional vehicles, the measurements should be performed on a gravel bed with wooden or concrete sleepers, the track should be dry and not frozen, well maintained, the level gradient at the track shall be 1:100 at the most in radii R = min 3000 m for the velocity up to 120 km/h and R = min 5000 m for the velocity higher than 120 km/h, in the measured section welded (without transitional sections), and without visible surface defects (material accumulation (and a hole in material) which got between the wheel and rail during the operation and so on).

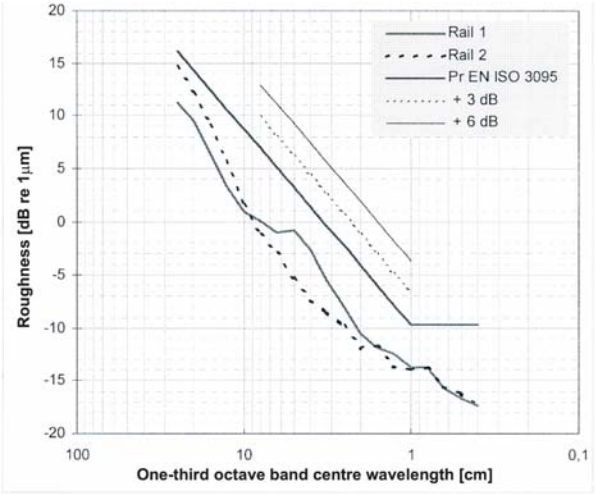

Fig. 1 The example of limit values of the rail surface roughness for high speed trains [1]

The quality of the rail head should be taken as accepted for measurements in the case when the surface roughness level of the tested track evaluated by the one third octave filter lays within the determined borders (Fig. 1).

Dynamic characteristics of the track have an important influence on the track contribution to the overall noise. Phenomena with the biggest influence on the noise are listed in Tab. 1. A real track may be characterised by measurements at static conditions on an unloaded track:
- vertical and horizontal railhead impedance (contains pad stiffness and damping),
- vertical and horizontal spatial decrease (includes the influence of subsoil and fasteners).

The impedance and decay are determined with the help of feedback measurement in the frequency domain 100 Hz – 8000 Hz. Notice: In order to determine a noise level range arising from the roughness the TWINS (Track Wheel Interaction Noise Software) programme is available at UIC [5]. As its input the programme used the diameter +/− 1 of the standard roughness deviation. Because the noise from a smooth wheel is very sensitive to the changes of rail roughness, the predictions were done for the wheel

which is braked by a disc brake and for the train velocity of 144 km/h.

The results of this analysis were utilised to determine the roughness influence on various noise levels from rolling so that it would be possible to elaborate recommendations for the roughness range which would be possible to be used as a standard for measurements processing.

Finally the results were elaborated into the recommendations for maximum roughness borders (limits) which define the track of "good quality" [5].

The results may be represented in one third octave belt with the roughness level of rail (in dB and reference of 1 μm) as a function of a wavelength (cm).

4. Unroundness of the wheel

The second member of the couple, which has an influence on the noise generation when rolling, is the railway wheel. The surface unevenness might be defined as a roughness deviation (differences between a real wheel radius and the ideal radius). It is possible to evaluate the unroundness in the plane of contact circles (seventy millimetres from the inner side of the wheel) or in plains which are parallel with it. In order to process the analysis, a numerical elaboration of measured data is necessary. The Fast Fourier Transformation (FFT) is the base of such an elaboration. We will mention the calculation procedure with the help of discrete Fourier Transformation (DFT) [4].

The measurement of wheel radius is done for separate angles of wheel semi-rolling α. The Fourier analysis is applied on the set of measured data till we obtain the $R(\alpha)$ function.

$$R(\alpha) = \sum_{k=0}^{L}\left[a_k \cdot \cos(k \cdot \alpha) + b_k \cdot \sin(k \cdot \alpha)\right],$$

$k = 0, 1, 2, \ldots L$ (2)

$$L = \frac{m}{2} \quad \text{interpolation} \tag{3}$$

$$L < \frac{m}{2} \quad \text{approximation} \tag{4}$$

$$a_0 = \frac{1}{m+1} \cdot \sum_{s=0}^{m} R(\alpha_s) \tag{5}$$

$$b_0 = 0 \tag{6}$$

$$a_k = \frac{2}{m+1} \cdot \sum_{s=0}^{m} R(\alpha_s) \cdot \cos(k \cdot \alpha_s) \tag{7}$$

$$b_k = \frac{2}{m+1} \cdot \sum_{s=0}^{m} R(\alpha_s) \cdot \sin(k \cdot \alpha_s) \tag{8}$$

$$\upsilon_k = arctg\frac{a_k}{b_k},\ s = 0, 1, \ldots, m \quad k = 1, 2, \ldots, L \tag{9}$$

The coefficients of the order represent separate harmonic parts of oscillation. For practical reasons we use the Fast Fourier Transformation (FFT), which is crucially faster.

The Fast Fourier Transformation – FFT is another way of Fourier Transformation calculation. The algorithm of evaluation has the computation time:

Computation time = $k_{FFT} N \log_2 N$, which is in comparison with the computation time of DFT

Computation time = $k_{DFT} N^2$ crucially shorter.

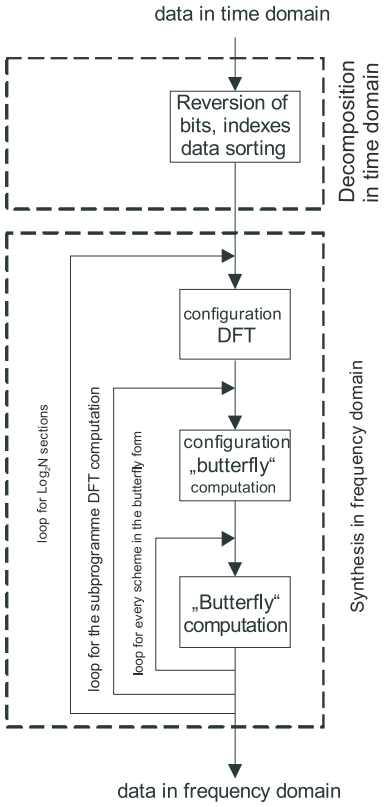

Fig. 2 Flowchart FFT

The flowchart depicts three essential steps: (1) to decompose N points in time domain into N signals out of which contains one point, (2) to find the signals spectrum of each point and (3) to make a synthesis of N frequency spectra into one frequency spectrum. The condition is that N must be a square of two.

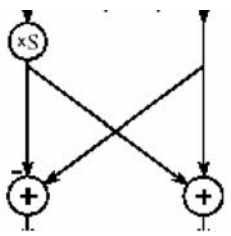

Fig.3 "Butterfly method computation of FFT"

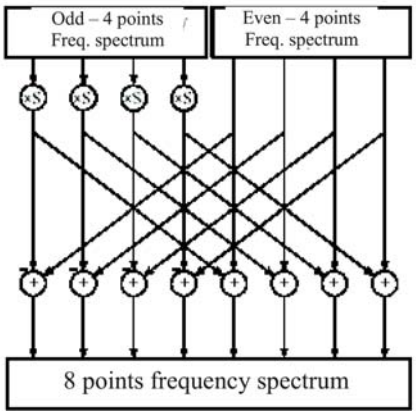

Fig. 4 The FFT synthesis flow chart

The basic calculation element in FFT which takes two complex points and converts them into two different complex points is depicted in Fig.3. This basic block diagram is called "Butterfly calculation", because of its image which reminds of butterfly wings. The flowchart of FFT synthesis depicts a method of combination of two four-point frequency spectra into one eight-point frequency spectrum. The symbol of operation "**xS**" means that the signal is multiplied by the sinus function with a suitably chosen frequency.

This example shows the procedure for N = 8 points. The signal depiction in the frequency domain allows us to have an idea about the measured signal features in the frequency domain. This depiction allows to configure numerical filters in the right way and to utilize only requested parts of the measured signal. At the same time it allows to discover some unwanted parts of the signal which may be caused by faulty condition of a part of the measurement system.

5. Evaluation of wheel unroundness

The base for the wheel unroundness evaluation is the knowledge of instant values of wheel radii dependence on the wheel semi-revolution angle.

In Fig.5 the dependency of the instant value of the wheel radius in the range of angle extent from 0 to 2π radian is depicted.

Amplitudes of separate harmonic parts characterise the geometrical shape of the measured wheel. The zero harmonic part represents the mean radius of the wheel. The first harmonic part determines eccentricity, the second one determines oval shape, the third one the degree of triangle shape, the fourth one the degree of rectangle, the fifth one the degree of pentangle and n-th one the degree of n-tangle.

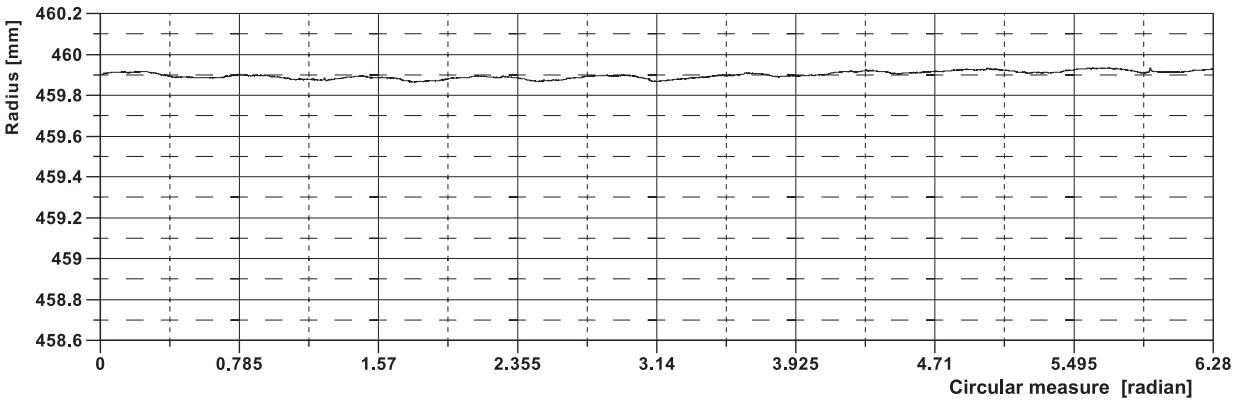

Fig. 5 Graph of wheel radii values

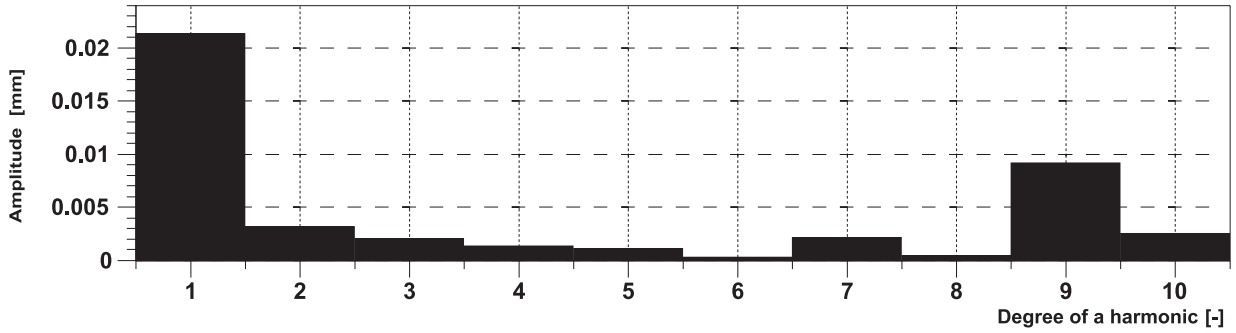

Fig. 6 Amplitude values of separate harmonic parts 1÷10 diagram

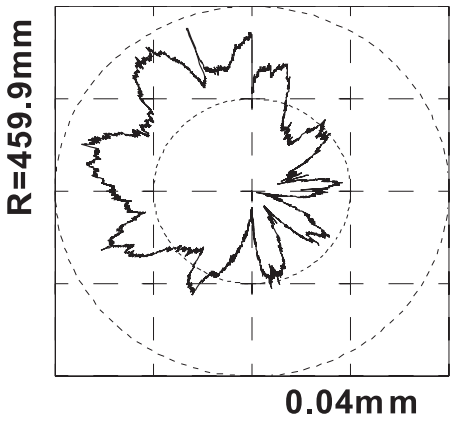

Fig. 7 Wheel radii values in the polar diagram

The ideal but hardly reachable state would occur when all parts except the zero one would be zero.

In Fig.7 the dependency of the instant value of the wheel radius in the range of angle extent from 0 to 2π radian in polar diagram is depicted.

The mean wheel radius (the amplitude of the zero harmonic) represents the inner circle in the diagram. In this case it corresponds to the wheel with an average value of radius of 459.9 mm. Another determining parameter of the graph is the outer circle with a double radius of the inner circle. In this case, the distance between the radii is 0.004 mm.

One third octave analysis

The one third octave analysis is based on the Fast Fourier Transformation.

The algorithm of discrete or fast Fourier transformation is applied on the set of measured values. The sum of amplitudes in the range of the tierce is performed for individual parts of the signal. The frequency spectrum is divided into individual tierce on the base of marginal values.

Numerical borders divide the frequency range into octaves. The frequency range which represents octave is divided into tierces. In the framework of the octave third the sum of power spectra densities (PSD) is processed and the result is added to the representative of the octave third.

When evaluating the data in the form of graph, we depict the dependence of the sum PSD from the frequency in the decade, or logarithmic axis, or the amplitudes from the wavelength in the decade or logarithmic axis.

The wheels parameters are evaluated in one wheelset, taking into consideration the position of the wheels in the bogie (left side, right side), wheelset in the bogie, bogie in the vehicle, type of the wheels, mileage of the vehicle, the way of braking of the vehicle, material of brake blocks or brake plates and so on.

The marginal values of tierces and octaves Tab. 2

Middle freq.	Tierce			Octave		
fm [Hz]	f0-fu [Hz]	F0 [Hz]	fu [Hz]	F0-fu [Hz]	F0 [Hz]	Fu [Hz]
20	5	22	18	22	45	22
25	6	28	22			
31.5	7	35	28			
40	9	45	36	45	89	45
50	12	56	45			
63	15	71	56			
80	19	90	71	88	177	88
100	23	112	89			
125	29	140	111			
160	37	180	143	177	354	177
200	46	224	178			
250	58	281	223			
315	73	354	281	354	707	354
400	93	449	356			
500	116	561	445			
630	146	707	561	707	1411	707
800	185	898	713			
1000	232	1122	891			
1250	289	1403	1114	1411	2828	1411
1600	371	1796	1425			
2000	463	2245	1782			
2500	579	2806	2227	2828	5657	2828
3150	729	3536	2806			
4000	926	4490	3564			
5000	1158	5612	4454	5657	11314	5657
6300	1459	7072	5613			
8000	1835	8980	7127			
10000	2316	11225	8909	11314	22627	11314
12500	2895	14031	11136			
16000	3705	17959	14254			

The calculation of the relation between the frequency and wavelength dependency is processed according to the relation:

$$\lambda = \frac{V}{f \cdot 3.6} \cdot 100 \qquad (11)$$

λ is wavelength (cm)
V is velocity (km/h)
f is frequency (Hz)

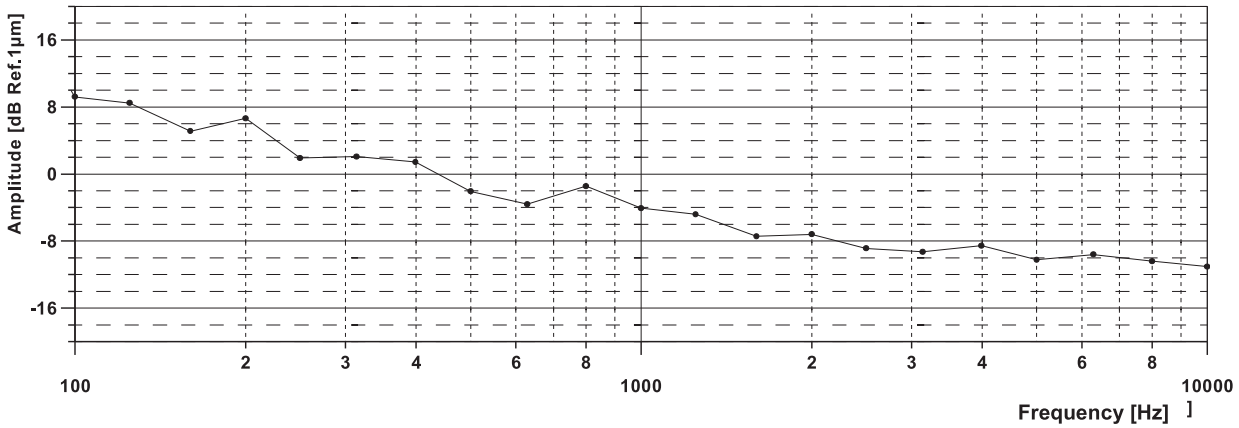

Fig. 8 One-third octave spectrum for unroundness of the wheel, amplitude on a frequency dependency and log. x-axis (V = 80km/h)

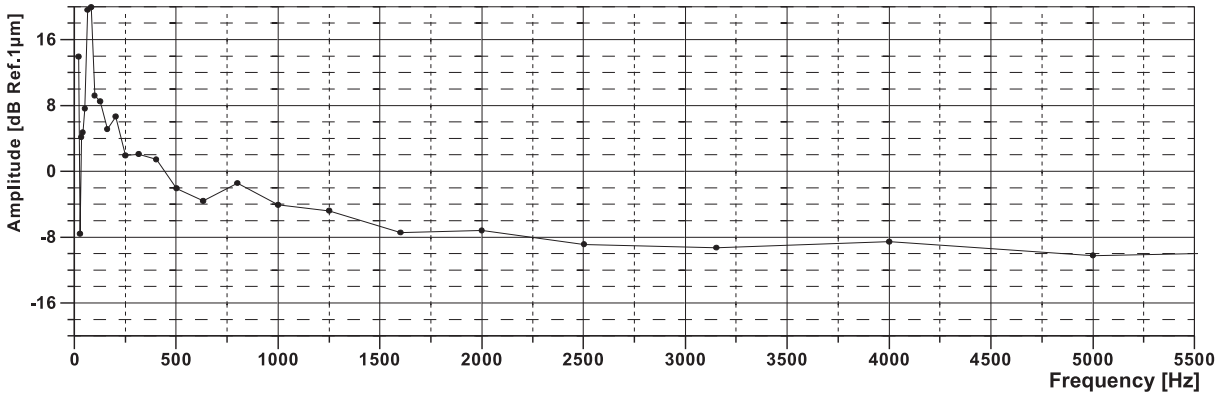

Fig. 9 One-third octave spectrum for unroundness of the wheel, frequency dependency (V = 80km/h)

One third octave spectrum

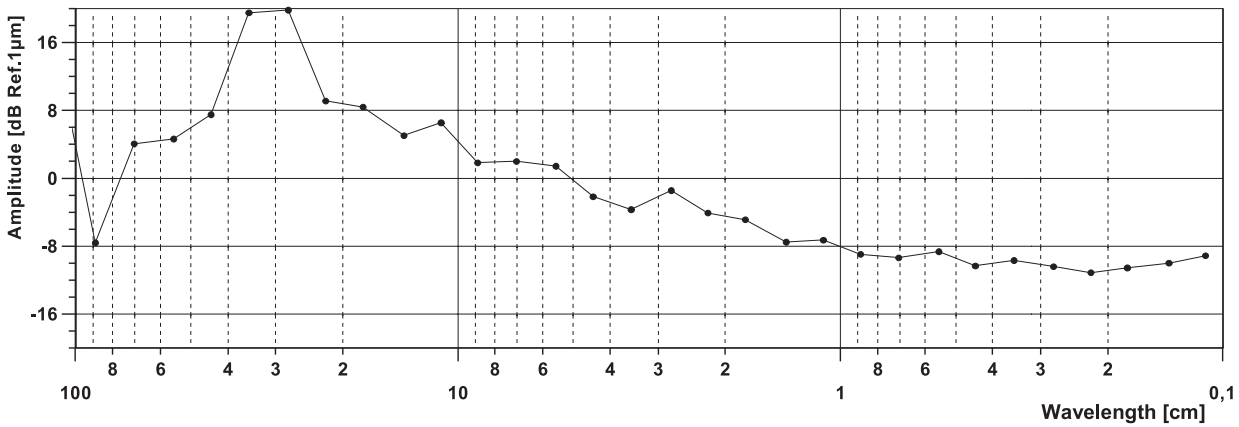

Fig. 10 The one-third octave spectrum for unroundness of the wheel, amplitude on a wavelength dependency (V = 80km/h)

Power spectrum

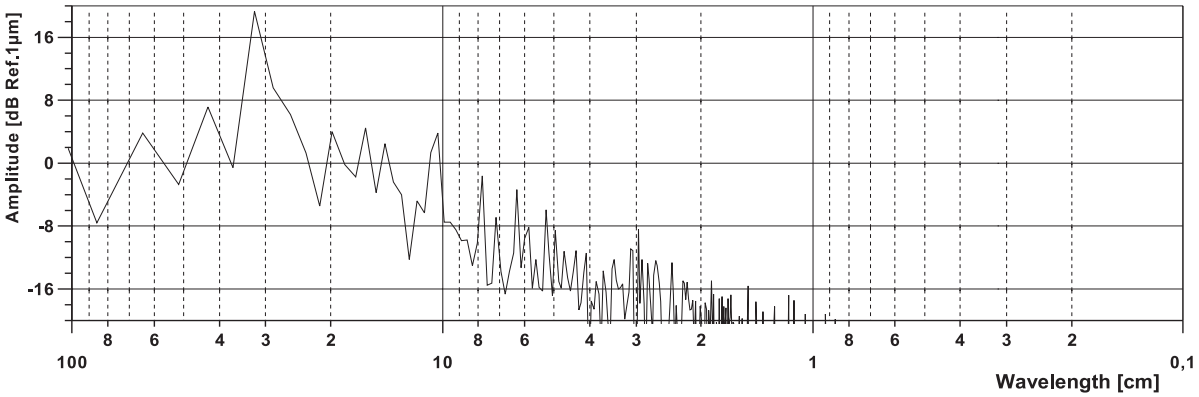

Fig. 11 Power spectrum for unroundness of the wheel, amplitude on a wavelength dependency and log. x-axis (V = 80km/h)

Amplitude spectrum

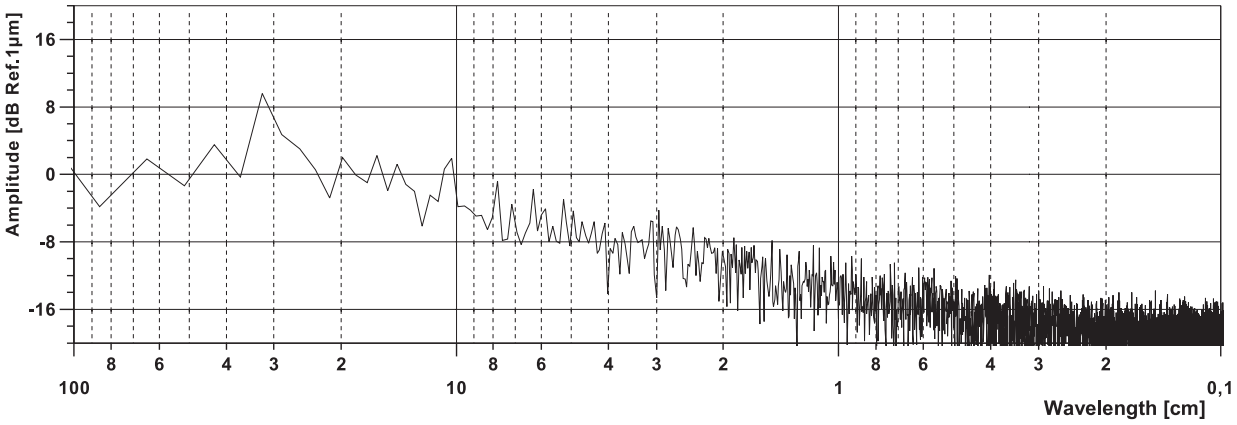

Fig. 12 Amplitude spectrum for unroundness of the wheel, amplitude on a wavelength dependency and log. x-axis

In the figures from 10 to 12 are depicted various dependencies. These graphs can be useful for an unroundness evaluation. There are the one-third octave spectrum for unroundness of the wheel – amplitude on a wavelength dependency, the power spectrum for unroundness of the wheel – amplitude on a wavelength dependency and log. x-axis and amplitude spectrum for unroundness of the wheel – amplitude on a wavelength dependency and log. x-axis.

6. Conclusion

The imperfection of railway wheel roundness and rail surface roughness cause the generation of vibrations which act not only in the closest distance from the source – wheel/rail contact and the noise is their consequence, but they spread via the rail into track and via the wheel into the vehicle where they act directly as noise and excite vehicle parts which then create noise and moreover, the overall noise increases as a result of the effect of rebounded outside noise from barriers which are in the way of spreading. Out of these issues we analysed chosen issues which are connected with the railway wheel un-roundness and their evaluation on the base of statistical data processing on which Fourier transformation with the help of one third octave analysis was applied.

7. Acknowledgement

The work was supported by the Scientific Grant Agency of the Ministry of Education of the Slovak Republic and the Slovak Academy of Sciences in Project No. 1/4119/07: “Investigation of Dynamic Properties of a Vehicle”.

References

[1] ERRI B 169/RP 18, *Überprüfung des akustischen Verhaltens von neuen Radbauformen.* Pr. 4.1, f1/3, 2003
[2] GERLICI, J.: *The Contact of a Railway Wheelset and a Track (in Slovak),* Habilitation Work, pp. 159, fig. 195. Faculty of Mechanical Engineering University of Žilina, 2004.
[3] JACOBSON, B., KALKER, J. J.: *Rolling Contact Phenomena,* CISM Courses and Lectures No. 411. Int. Centre for Mechanical Sciences, ISBN- 3-211-83332-3 Springer-Verlag Wien, New York. CISM, Udine, 2000.
[4] LACK, T.: *The Dynamic Properties Analysis of Vehicles from the Point of View of Ride Comfort (in Slovak)*, Habilitation Work, pp. 176, fig. 178, Faculty of Mechanical Engineering University of Zilina, 2007.
[5] prEN ISO 3095, *Final Draft 11/2002, Railway Applications - Acoustics - Measurement of Noise Emitted by Railbound Vehicles* (ISO/DIS 3095:2001), Brussel 2001.

Juraj Gerlici – Tomas Lack *

ITERATIVE METHOD FOR RAILWAY WHEEL PROFILE DESIGN

The presented article deals with the methods for the railway wheel profile development on the base of the intended shape of wheelset/track contact geometric characteristics. The article deals with two methods. In short the profiles creation method through arcs radii profile variation is mentioned. The main emphasis is directed to the "Iterative method for a railway wheel profile design". This method is explained in a more detailed way in the article. The base for the creation of new profiles with the help of the first method is an interactive attitude based on the modification of the original shape which is defined by section of a railway wheel profile, with interconnected and exactly defined arcs radii. It is possible to change them according to shape needs of the final geometrical characteristics. The base of the iterative method, which is of the highest importance in this article, is to develop a new profile under given conditions – a prescribed shape of the contact points distribution and the shape of delta-r function. The newly developed wheel profile in the couple with given rail profile will have requested chosen characteristic shapes.

Key words: railway wheel profile, profile development, iterative method

1. Introduction

Today there is an extremely up to date need for security of vehicles interoperability in its greatest extent in order to use in reality one of the most important advantages of railway transport – economic transport of a huge volume of goods over long distances and comfortable transport of passengers. Track forces are of the highest relevance from the point of view of safe vehicle operation on the track. The wheel/rail geometry is one of the main parameters influencing track forces and vehicles dynamics.

In the article we will deal with methods for the railway wheel profile development on the base of the intended shape of wheelset/track geometric characteristics. In short the profiles creation method through arcs radii profile variation is mentioned, the main emphasis is directed to the "Iterative method for a railway wheel tread profile design". This method is in detail explained in this article.

2. The wheel profile development on the base of a geometric characteristics shape

Wheelset and rail geometric characteristics help to specify the geometric binding of a wheelset and rail. With their help it is possible to assess relatively quickly some parameters of the binding which help to estimate how a vehicle or, better to say, a wheelset can behave in real operation.

Under geometric characteristics we understand the following: contact points distribution between a wheel and rail at a lateral

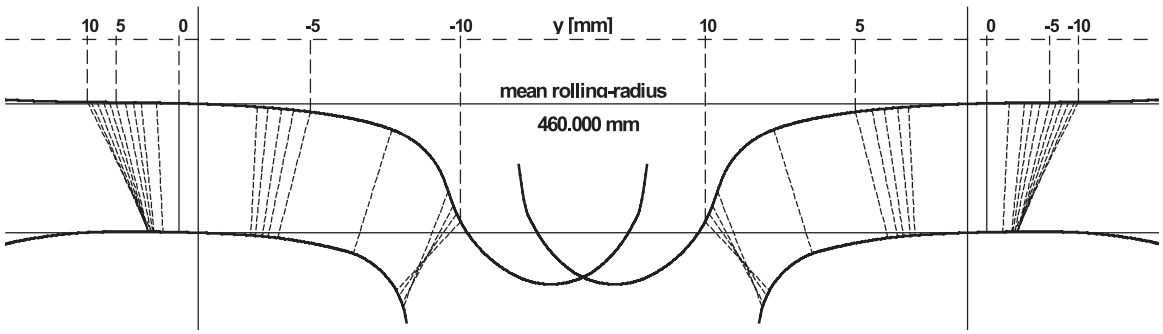

Fig.1 Contact points at S1002/UIC60/1:40/1435 combination (Common situation)

* **Juraj Gerlici, Tomas Lack**
Faculty of Mechanical Engineering. University of Zilina, Slovakia, E-mail: juraj.gerlici@fstroj.uniza.sk

movement of wheels profiles of a wheelset over the rail heads profiles, see Fig. 1, Delta r function, Tangent Gamma function, Equivalent conicity function and Radial steering index.

The basic presupposition for the characteristics evaluation is detailed knowledge of a wheel and rail profiles geometric shape.

It is not possible to state a generally "optimum" profile for all types of tracks and railway wheels. The main reason is that in operation there are tracks with various gauges, various rail heads profiles on which vehicles with various railway wheels profiles move. Vehicles move at various speeds, with various wheel forces, they transport various goods and on top of it we require various kinematics behavior. That is why it is very difficult to state unambiguous criteria which could be defined and compared when taking into account all vehicles.

We choose geometric characteristics of a railway wheelset and rail and we will state our intended wheel profile on the base of their specific shape.

Both of the mentioned methods: "Profiles creation method through arcs radii profile variation" and "Iterative method for railway wheel tread profile design" have the same aim, to develop the wheel profile on the base of a requested shape of selected contact geometric characteristics, but each of them use different input parameters, work on different core procedures.

3. Criteria for the search of a requested profile

We stated the following conditions as criteria for optimizing the process:

- ***fluent distribution of contact points on the wheel and rail surface,***
- ***delta–r function shape*** without jump change of the course,
- *requested equivalent conicity,*
- *exclusion of two- point- contact*

The difference function course shape (delta-r) without jumps indicates a continual increase in lateral forces in the wheel and rail contact point without kick bounces and additional dynamic exciting of the vehicle mechanical system. This phenomenon is shown in the value of safety against derailment.

The size of an instant equivalent conicity value is connected with the size of wavelength of periodic oscillation movement which a wheelset performs. A low conicity value presupposes a higher wavelength value. The sufficient wavelength size is extremely important for a high speed railway operation. The size of equivalent conicity is projected into the stability of vehicle movement and riding comfort of passengers.

The determining value of equivalent conicity is stated at the movement amplitude of 3 mm. The contact points distribution across the profile has a crucial influence on wearing (resistance against wearing) of a wheel and material and, at the same time, the geometric stability of their profiles. From the nature of the way of geometrical characteristic evaluation it is clear that it is not possible to suggest profile geometry directly on the base of a contact points position setting. Various authors have applied various procedures where a continual profile shape modification on the base of a geometric characteristic is the starting point.

4. Profiles creation method through arcs radii profile variation

We used the method of arcs radii profiles variation for the creation of new profiles which meet the given criteria. This method was presented in detail in [1].

The base of the activity is an interactive attitude based on the modification of the original shape defined by parts of the railway wheel profile interlinked with exactly defined arcs radii which it may be changed according to the need to the final geometric characteristics shape.

The basic procedure is as follows:

1. We have the profile of the rail of UIC 60 1:40.
2. We have a requested shape of geometric characteristics: it is low equivalent conicity ≤ of 0.05 in the given case.
3. We choose a "suitable" wheel profile: we will choose the up to now used profile of S1002.
4. We perform numerical division of the whole existing wheel profile in order to obtain simple geometric parts.
5. We create the radii function $R(y)$ (in dependence on the lateral wheel profile coordinate).

   The radii function R depends on the lateral movement y, z is a vertical profile coordinate.

$$R = R(y) \tag{1}$$

$$z'' = \frac{\left[1 + (z')^2\right]^{\frac{3}{2}}}{R(y)} \tag{2}$$

6. We set the starting conditions in the equation $y_0 = 0$, $z_0 = 0$, $z'_0 = tg$ profile tangent slope. The initial condition secure that the beginning of the profile coordinate system is placed in a horizontal direction into the plane of a nominal wheel radii circle and the profile crosses the beginning. The first z'_0 coordinate derivation determines the tangent value of the profile tangent slope in the point $[y_0, z_0]$. The profile is created by the solution of the differential function (2) continually from the point $[y_0, z_0]$ to the left side and then from the point $[y_0, z_0]$ to the right side.
7. In the given example, it is the first derivation = tangent value in the starting point = 0.05.
8. We change the selected radius (from the original S1002 profile radii) and compute the equation (2).
9. When the new profile is derived, the geometric characteristics are evaluated and the results are assessed. If the results meet

our expectations, the profile is accepted, if the results do not fulfill our expectations, the selected radius (radii) is (are) changed and computations have to continue. In this case, there is a need for knowledge and for experience and skills in the radius selection and radius value for the determination of the change.

The Nyström method was used for the solution of the differential function (2) arising from the relationship for curvature. Its application for the solution of the function (2) is in relationship with the starting conditions defined in point Nr. 6.

Results of application of the method of arcs radii profile variation

Wheel profiles (NEWRAD_I) which correspond to our needs thanks to their properties were created on the base of the chosen input parameters at defined optimizing criteria.

5. Iterative method

The other method based on different presuppositions than the first presented method which can be used for the new railway wheel tread profile design is the "Iterative method". This method can help us reach our aim to have the wheel profile with requested properties according to the given conditions based on the requested shapes of geometric characteristics.

1. We set the functions which describe the rail profiles: f_{kp}, f_{kl}.
2. We set the f_x function for x-contact points on rail coordinates prescriptions in dependency on the lateral wheelset movement y_w.
3. We set the f_{dr} function for the requested Δr function characteristics prescription in dependency on the lateral wheelset movement y_w.
4. $y_w = y_{w\,\min}$, $i = 0$ the index i and a lateral shift of a wheelset initiation.

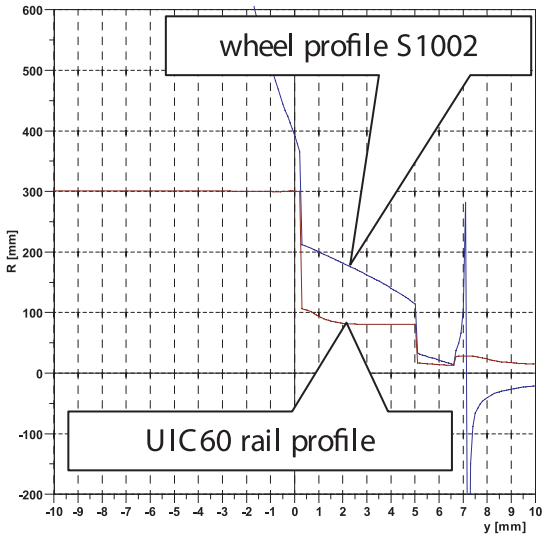

Fig. 2 Profiles radii S1002 and UIC60 at contact points

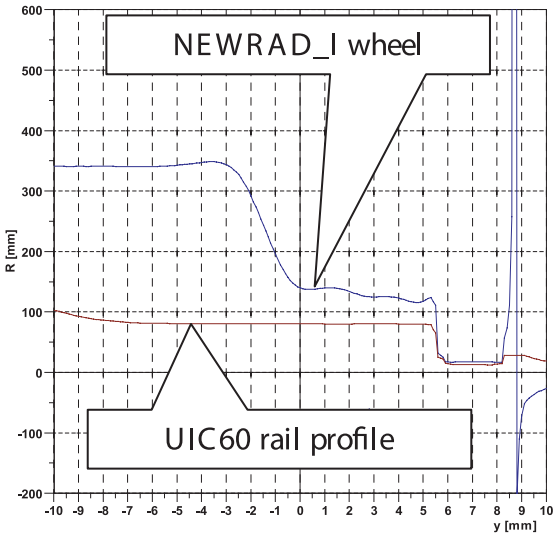

Fig. 3 Profiles radii NEWRAD and UIC60 at contact points

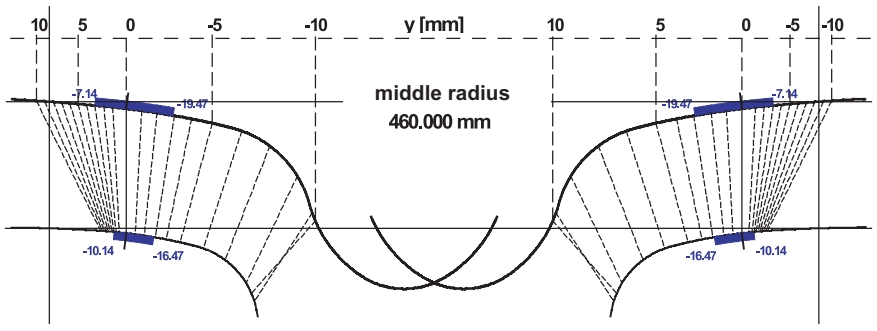

Fig.4 Contact points at profiles combination NEWRAD_I/UIC60/1:40/1435 with marking of contact points interval at a wheelset lateral movement in a rail with amplitude of 3 mm

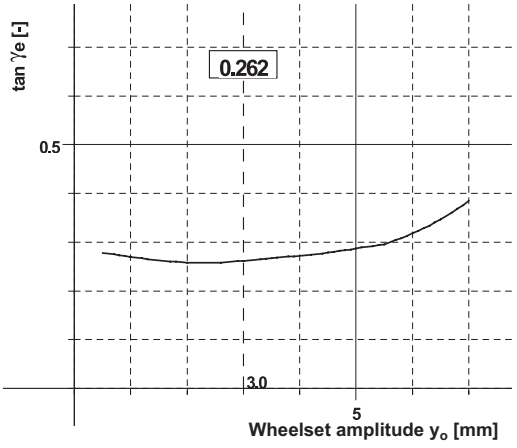

Fig. 5 Equivalent conicity function for the profiles couples NEWARDI/UIC60/I:40/920/1435

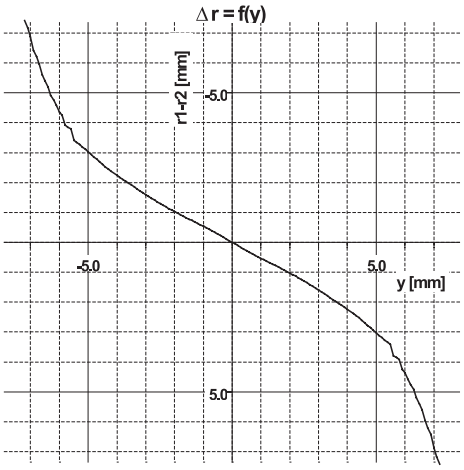

Fig. 6 Delta r function for the profiles combination NEWARDI/UIC60/I:40/1435

5. $x_p = f_x(-y_w) + y_w$
   $x_l = f_x(y_w) - y_w$
   $y_p = f_{kp}(x_p)$
   $y_l = f_{kl}(x_l)$
   the contact points on the rail coordinates calculation.
6. $d = y_l - y_p - f_{dr}(y_w)$ the d parameter calculation.
7. $x_{rp}[i] = f_x(-y_w)$
   $y_{rp}[i] = -y_p - \frac{d}{2}$
   $x_{rl}[i] = f_x(y_w)$
   $y_{rl}[i] = -y_l + \frac{d}{2}$
   wheel profiles points calculation.
8. $y_w = y_w + \Delta y_w$
   $i = i + 1$
   wheelset lateral shift increasing y_w for an increment Δy_w and the index i increasing.
9. If $y_w < y_{w\,\max}$ go to the Nr. 4.
10. Smoothing of the developed wheel profiles with the help of the spline smoothing.
11. The functions courses computation. The functions characterize the rail/wheel contact.
12. The judgment of the Δr, tan γ, tan γ_e. characteristics courses
13. If the result is acceptable, the wheel profiles are created and whole process is finished.
14. We modify the f_x function course for contact points on the rail x-coordinate prescription in dependence on the wheelset lateral shift y_w and we modify the function f_{dr} for the prescription of the requested Δr characteristic course in dependence on the wheelset lateral shift y_w.
15. Return to point Nr. 3.

Where:

y_w – is a wheelset lateral movement
$y_{w\,\min}$ – starting lateral movement of a wheelset
$y_{w\,\max}$ – ending lateral movement of a wheelset
$f_{kp}(x)$ – right rail profile describing function
$f_{kl}(x)$ – left rail profile describing function
$f_x(y_w)$ – the function determining the x-coordinates of the contact points on the rail
$f_{dr}(y_w)$ – prescription function for requested shape of Δr function
x_p – x- contact point coordinate at the right rail
x_l – x- contact point coordinate at the left rail
y_p – y- contact point coordinate at the right rail
y_l – y- contact point coordinate at the left rail
d – difference of y-th coordinates
i – index of the point of a profile
$x_{rp}[i]$ – x- axis coordinate of i-th point of the right wheel profile

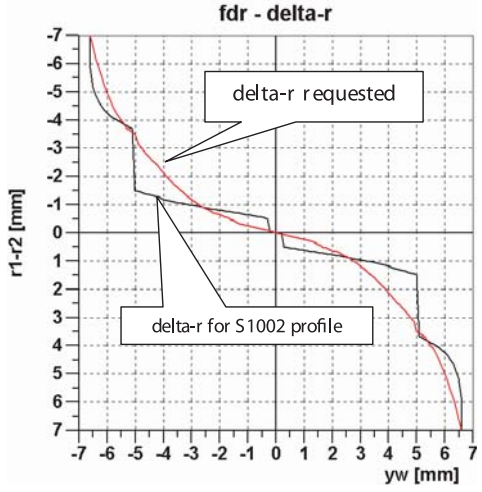

Fig. 7 Delta-r function for S1002 wheel profile and requested shape of delta-r for a new developed profile NEWRAD depiction

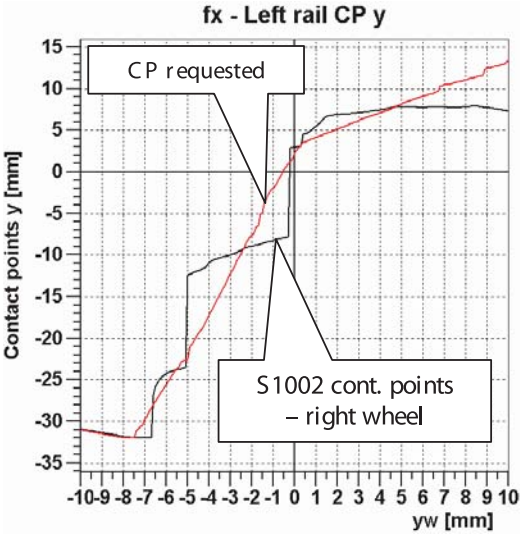

Fig.8 Contact points function for S1002 wheel profile and requested shape of contact points placement function (fx) for a new developed profile NEWRAD depiction; left wheel profile/UIC60

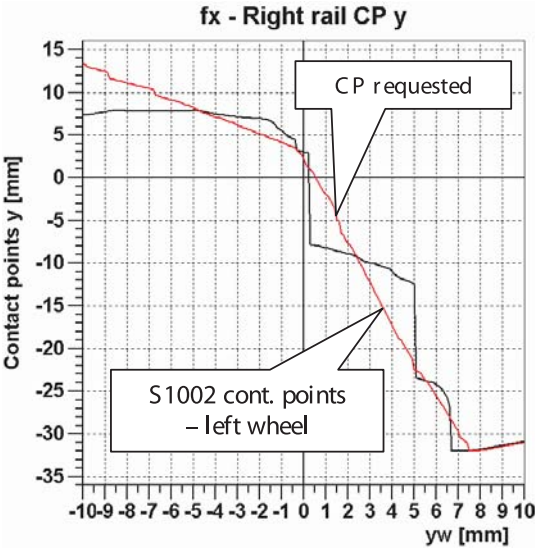

Fig. 9 Contact points function for S1002 wheel profile and requested shape of contact points placement function (fx) for a new developed profile NEWRAD depiction; right wheel profile/UIC60

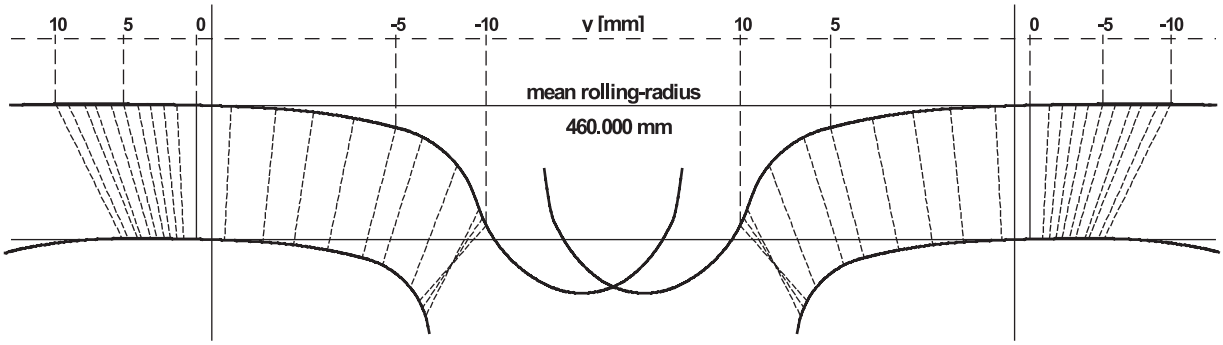

Fig.10 Contact points at profiles combination NEWRAD/UIC60/1:40/1435

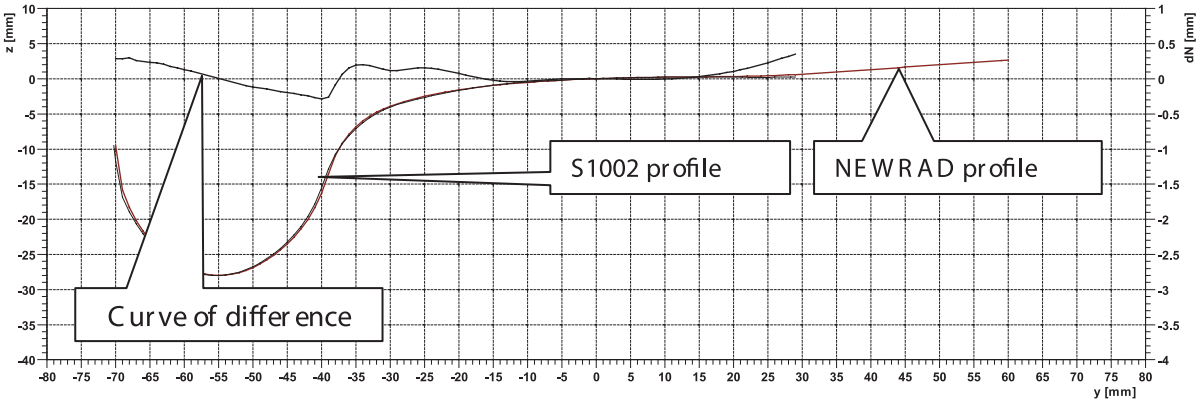

Fig. 11 Course of the difference curve between theoretical wheel profile of S1002 and NEW designed profile NEWRAD with regard to a lateral profile coordinate yw

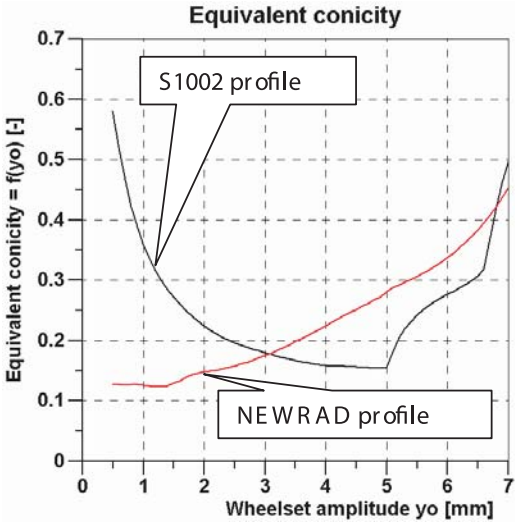

Fig. 12 Equivalent conicity function for profiles combination NEWRAD and S1002/UIC60/1:40/1435

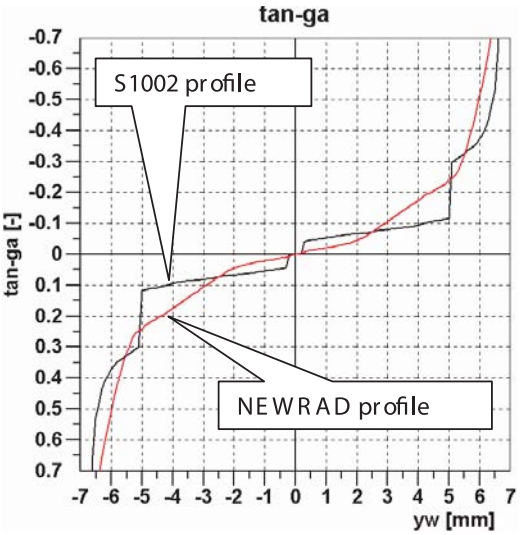

Fig. 13 Tangent gamma function for profiles combination NEWRAD and S1002/UIC60/1:40/1435

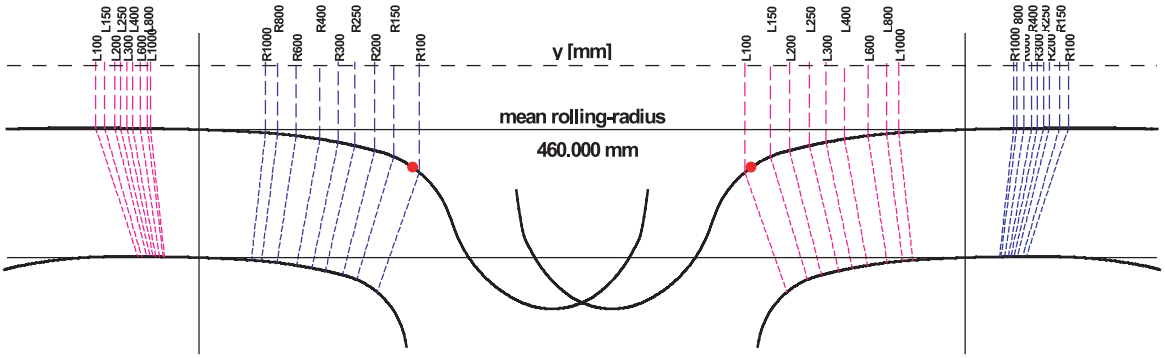

Fig.14 Contact points function with marked radii for a kinematic movement through a track curve for the rail profile UIC60 and wheel profile NEWRAD

Left arc NEWRAD		Left arc S1002	
Radius [m]	yw [mm]	Radius [m]	yw [mm]
L100	6.5847	L100	6.615
L150	5.847	L150	6.275
L200	4.983	L200	5.09
L250	4.581	L250	5.058
L300	4.147	L300	5.037
L400	3.622	L400	5.011
L600	2.964	L600	3.904
L800	2.524	L800	2.443
L1000	2.19	L1000	1.358

Tab.1 Radii for a kinematic movement through a track curve

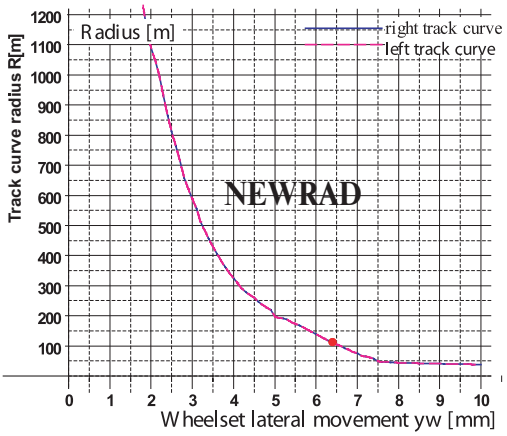

Fig. 15 Graphic expression of the dependency of radii for a kinematic movement through a track curve on the wheelset lateral movement

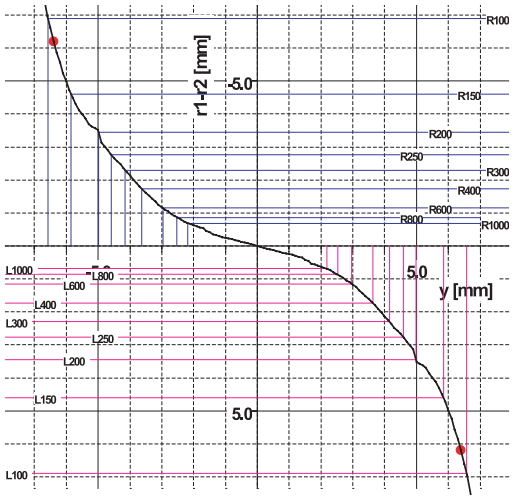

Fig. 16 Delta r function with marked radii for a kinematic movement through a track curve for the rail profile UIC60 and wheel profile NEWRAD

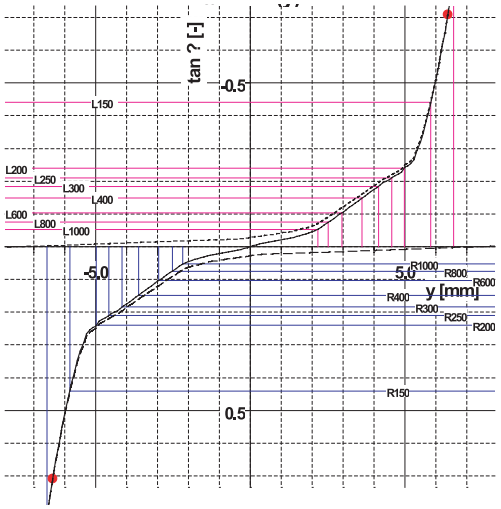

Fig. 17 Tangent Gamma function with marked radii for a kinematic movement through a track curve for the rail profile UIC60 and wheel profile NEWRAD

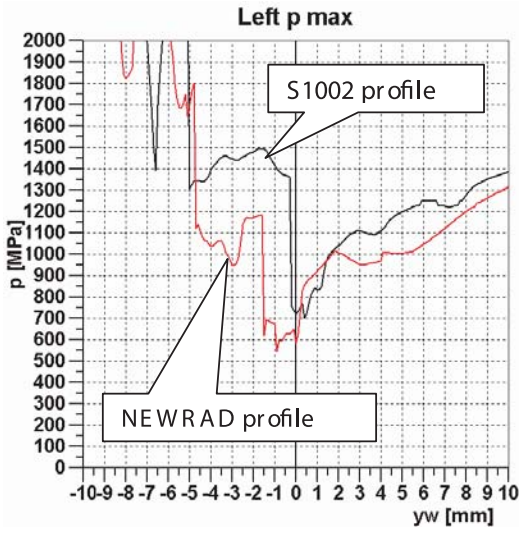

Fig. 18 Normal stresses evaluation (by Hertz) for S1002 wheel profile and NEWRAD profile; UIC60/1:40/100.000N, left wheel

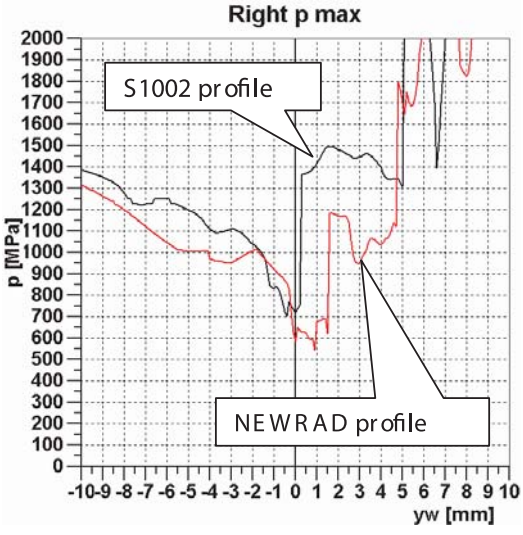

Fig. 19 Normal stresses evaluation (by Hertz) for S1002 wheel profile and NEWRAD profile; UIC60/1:40/100.000N, right wheel

$y_{rp}[i]$ – y- axis coordinate of i-th point of the right wheel profile
$x_{rl}[i]$ – x-axis coordinate of i-th point of the left wheel profile
$y_{rl}[i]$ – y-axis coordinate of i-th point of the left wheel profile

It is evident from Figs. 14, 15, 16 that a wheel equipped with a NEWRAD wheel profile can move in a kinematic way through the rail arc radii in a fluent continuous way. This happens at the given configuration already from zero to seven mm of lateral displacement. It is not possible when combining the wheel profile S1002 and the profile UIC60. Fig. 10 illustrates the regular distance of contact points. Fig.18 and Fig. 19 show the stress distribution. NEWRAD shows lower maximum values of the normal stress evaluated by the Hertz method.

6. Conclusion

The presented article deals with the methods for the railway wheel profile development on the base of the intended shape of wheelset/track contact geometric characteristics. In short, the profiles creation method through arcs radii profile variation [1] see Fig. 4 was mentioned. The result wheel profile is named NEW-

RAD_I. The base for the creation of new profiles with the help of the first method is an interactive attitude based on the modification of "the original shape which is defined by a section of a railway wheel profile", with interconnected and exactly defined arcs radii. It is possible to change them according to shape needs of the final geometrical characteristics in Fig. 5 and Fig. 6. The main emphasis is directed to the "Iterative method for railway wheel tread profile design". This method is in detail explained in this article. The base of the mainly presented iterative method is to develop a new profile under the given conditions – a prescribed shape of the contact points distribution and shape of delta r function. The new developed wheel profile together with the given rail profile will have requested characteristics. This method can be used after modification for a design of rail profile in accordance with the wheel profile. It is evident from Fig. 14, 15 and 16 that a wheel equipped with the NEWRAD wheel profile can move in a kinematic way through the rail arc radii in a fluent continuous way. This happens at the given configuration from zero to seven mm of a lateral displacement. This is not possible when the wheel profile S1002 and the profile UIC60 are combined. In Fig. 10 there is a regular distance of the contact points. Fig. 18 and Fig. 19 show the stress distribution. NEWRAD shows lower maximum values of the normal stress evaluated by the Hertz method.

7. Acknowledgement

The work was supported by the Scientific Grant Agency of the Ministry of Education of the Slovak Republic and the Slovak Academy of Sciences in project No. 1/4119/07: "Investigation of a dynamical properties of a vehicle".

References

[1] GERLICI, J., LACK, T.: *Synthesis of Railway Wheel and Rail Head Profiles via the Usage of Arcs Radii Profile Variation,* XVII Konferencja naukova Pojazdy szynowe. Pp. 63-78. Zam.536-06, Oficyna Wydawnictwa Politechniky Warszawskej, Warszawa 2006.

[2] GERLICI, J., LACK, T. et al: *Transport Means Properties Analysis – Vol. I*, Monograph, p. 214, ISBN 80-8070-408-2, EDIS, University of Zilina, 2005.

[3] LACK, T., GERLICI, J.: *Contact Area and Normal Stress Determination on Railway Wheel/Rail Contact,* Communications – Scientific Letters of the University of Zilina, 2/2005, ISSN 1335-4205, EDIS, , 2005, pp. 38–45.

[4] LACK, T., GERLICI, J.: *Profiles synthesis through radii variation of arcs profile (in Slovak),* Current problems in Rail Vehicles, ISBN 80-7194-780-6, DFJP UP, DP Ceska Trebova, 2005, pp. 115–135.

[5] UIC Code 519: *Method for Determining the Equivalent Conicity*, Draft of January 2003 Original version, 2003.

[6] UIC-Kodex 510-2 VE: *Wagen. Bedingungen fur die Verwendung von Radern verschiedener Durchmesser in Laufwerken unterschiedlicher Bauart,* 2002.

Slavomir Hrcek – Vaclav Kraus – Robert Kohar – Stefan Medvecky – Pavol Lehocky *

CONSTRUCTION OF A BEARING TESTING APPARATUS TO ASSESS LIFETIME OF LARGE-SCALE BEARINGS

This article discusses steps towards the design, construction and production of a device used for lifetime assessment of large-scale bearings. The machine is reviewed as a mechatronic entity, comprised of three parts - mechanical, electro technical and hydraulic. The mechanical part was designed with the help of modern CAD/CAE/PDM design systems along with device parts modeling and strength analysis of highly stressed device parts. The electrotechnical part consists of a driving unit - containing the frequency transducer and an asynchronous motor; the PLC-driven operating part together with a touchscreen interface and a monitoring part which includes a datalogging device to record measurement results and interface with a PC.

1. Introduction

Electricity from renewable power sources plays an important part in today's world. One such example is energy obtained from wind power. Wind energy has evolved quickly since the seventies during the oil crisis and still continues. Wind energy accounts for 2 % of all energy produced in Europe, while in Germany almost 5 % and in Denmark 20% of all energy is produced from wind. More than 80% of all wind turbines are produced by European companies, which is evident in the high number of installations (approximately 85% of all installations are located in Europe). [1]

Most common wind generators are tri-blade type with a vertical axis. Most turbines are capable of changing the orientation of the blade part based on wind direction. Large wind turbines usually generate tri-phase alternating current, which is then run through a transformer located nearby or directly on the turbine structure. Electricity is then transported similar to other power sources. [1]

One of the largest producers of wind turbines is a company called Vestas [2] that produces wind generators for power range between 850 kW to 3 MW. Wind generators are usually installed into fields, located either on land or sea. The latter is important when considering more efficient wind turbines at locations such as sea shelve. Wind turbines have an average lifetime of 20 to 25 years. [1]

One of the main parts of wind generators is the rotor, upon which is placed the propeller. The rotor is placed in the stator part of the generator on two barrel bearings. Based on the power of the wind generator, the bearings used can have an outer diameter of two meters or more. PSL a.s. Povazska Bystrica [3] produces the mentioned bearing types. The bearing manufacturer must guarantee a bearing lifetime of at least 20 years. The bearing lifetime is based on accelerated lifetime tests. These tests require appropriate testing methodology and testing apparatus used to measure the lifetime of the bearings. The need for lifetime testing of these dimensionally-atypical bearings, exceeding the dimensions of standard bearing types, has led to a joint venture between the University of Zilina and manufacturer PSL a.s. Povazska Bystrica whose aim was to construct a testing apparatus aimed at evaluating the lifetime of bearings produced by the manufacturer.

2. Testing apparatus design

The testing apparatus design was based on a study aimed at testing special cone-shaped bearings with a maximum diameter of 1300 mm, conducted by the manufacturer PSL a.s. The aim of the study was to design a testing apparatus capable of determining the following parameters: Rating life *Lhv* and Basic dynamic carrying-capacity *Cr* in a relatively short time, approximately three months from the start of the test. The object of the study were special cone-shaped bearings with a maximum outer diameter $\phi = 1300$ mm. The study also outlined testing methodology and definitions of parameters which respected the following requirements: Dynamic carrying-capacity of the said bearings Cr, Rating life *Li* 10^6 rev., rotational frequency 20 to 30 min^{-1}, purely axial loading of the bearings and a testing interval not longer than 3 to 4 months.

With respect to the mentioned parameters, the methodology determined the maximum bearing load force with maximum dynamic carrying-capacity (*Cr*) 4000 kN in the axial direction. The whole testing apparatus was rated according to this loading force.

The study took into account two types of force exerted onto the bearing. The first consisted in mechanical calculation of the

* **Slavomir Hrcek, Vaclav Kraus, Robert Kohar, Stefan Medvecky[1], Pavol Lehocky[2]**
[1] Faculty of Mechanical Engineering, University of Zilina, Slovakia, E-mail: slavomir.hrcek@fstroj.uniza.sk
[2] Faculty of Electrical Engineering, University of Zilina, Slovakia

axial force be means of diaphragm springs. The second consisted in calculation by means of a hydraulic cylinder. Both alternatives were considered, however it was agreed that the mechanical calculation had numerous disadvantages. Load force setting would also be problematic, reaching values around 4000 kN. Also load force monitoring would be very coarse because considering the fact that when using plate springs the force is not directly proportional to the deformation. Calibration of such force would also be complicated and expensive. For these reasons it was agreed not to use this method.

Instead, the second method based on hydraulic load force calculation with a double acting hydraulic cylinder was used. The study considered the use of a single hydraulic cylinder which would determine the force exactly in the axis of the mounted bearing. This configuration would require a massive support which would intercept the reactive force from the loading force, requiring the use of massive profiles when constructing the support and additional technical complexity when welding and problematic fixation on the ground. Because the location of the hydraulic cylinder and support would be in the axis of the tested bearing, manipulation with the bearing and fastening accessories into test state would require a crane (the weight of the said bearings exceeds hundreds of kilograms) or a loading device placed in the testing hall.

For this reason the hydraulic method was modified and the testing apparatus itself consisted of four smaller hydraulic cylinders placed outside the axis of the tested bearings.

3. Mechanical part

Modern CAD, CAE and PDM/PLM applications were used when constructing the mechanical parts of the testing apparatus. Pro/ENGINEER was used to construct individual components of the testing apparatus.

The basic idea behind the design of the testing apparatus was to place the tested bearing between two plates pressed against each other by means of four hydraulic cylinders. This arrangement is advantageous due to the fact that it is a closed system and no reactive force is transferred outside this system. The bearing is placed between these two plates and attached onto the clutch of an electromotor with gear which provides the bearing movement.

The lower plate has a square profile with a width of 140 mm. The bottom part contains the electromotor with gear, the four hydraulic cylinders are placed in the corners and the upper part contains the fastening accessories for the tested bearing. Strength analysis in CAE system Ansys/Workbench showed that the base plate ends would bend under the force exerted by the hydraulic cylinders. To overcome this problem, ring-shaped stiffeners were placed near the hydraulic cylinders, which were then welded to the bottom part of the plate, lowering the total deformation to an acceptable level. The diameters of the cylinders were optimized thanks to the interconnection between Pro/ENGINEER and Ansys/Workbench, defining optimization with the main goal of finding acceptable strain levels by means of variation of the diameter of the additive rings.

The upper plate was originally designed as massive weldment of the plate and four cross-placed ribs, containing openings to place pivots through the eyes of hydraulic cylinders. However, from a technological point of view, this concept was disadvantageous because of the complexity when welding the upper plate and the resulting finishing of the functional areas would be uneconomical in view of the budget allocated for the testing apparatus. To this end, the construction of the upper place was modified and an assembly system was used. This change required modification of the plate, which was also optimized in Ansys/Workbench using the finite elements method with criterion of allowable strain.

Because of time restrictions and the loading method used, the testing apparatus was designed in such a way so as to allow the concurrent testing of two bearings of the same type oriented against each other. A fastening apparatus was designed to place the bearings into the testing apparatus. The inner rings of bearing were fitted to the central shaft, which was connected to the output axle of the gear via a clutch with involute splining. This arrangement allowed for the shifting of the axle with inner rings in the axial direction. This shift is caused by the pressing of tested bearings in the axial direction. The outer rings of the bearings are placed in

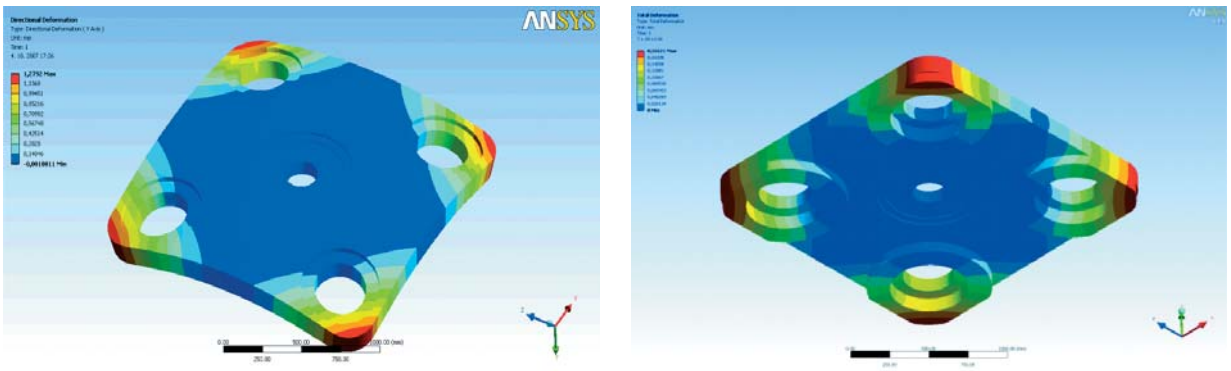

Fig. 1. Strength analysis of welded bottom plate

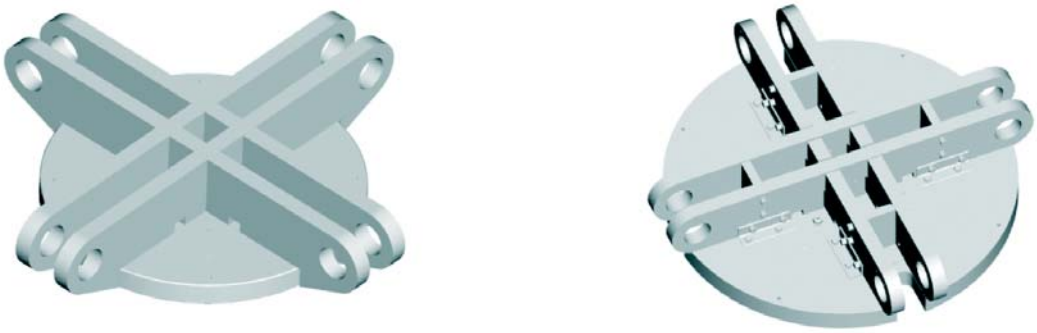

Fig. 2. Upper plate constructional modification

two rings which contain temperature and vibration sensors and the output sensor data were used in the evaluation of the bearing life-time.

The study requested the possibility to replace the tested bearings from the fastening apparatus to change the same bearing type to repeat the test. However this is not possible because the fastening apparatus was designed with clearance fit for the inner bearing rings and axle and also the outer bearing ring and outer rings. This arrangement does not correspond to real-life arrangements and leads to the destruction of the outer ring of one of the tested bearings. For this reason a separate fastening apparatus will be manufactured for each tested bearing set with overlapping identical to the real-life conditions used in wind-generators. The dismantling of the bearings from the fastening apparatus will however be very complicated, if not impossible. Real-life conditions are nonetheless more important criterion when testing the life-time of bearings.

4. Electrical part

To assure the function of the testing apparatus, the mechanical part must be complemented by appropriate electrical part, such as driving units used to launch all mechanisms and units that regulate and operate driving mechanisms based on the testing methodology. The designed apparatus has a testing state function and this requires the monitoring and recording of the measured data. The complete electrical part of the device can also be called the electric outfit of the machine.

The electric part of the designed device can be divided into the following parts:

- power (force) part: this part includes bus-bar, belaying and switching elements, frequency transducer, which drives the main gear of the testing state and ensures constant RPM during the whole test a gradual startup and shutdown or immediate stop in case of emergency state. The force part also includes the power supply of the pumps used in the hydraulic device and drive of the ventilator and pumps of the cooling assembly. Each device is powered by the required voltage, in this case either 230 V 50 Hz or 24 V DC from a switching supply,
- control part, which consists of a PLC automat, input control elements (buttons, touchscreen), transducers, output – action elements (electromagnetic valves of the hydraulic device, switching elements of ventilators and cooling pumps, input control part of the frequency transducer regulating the RPM, stop, start, emergency stop of the main traction, relay, signalization...),

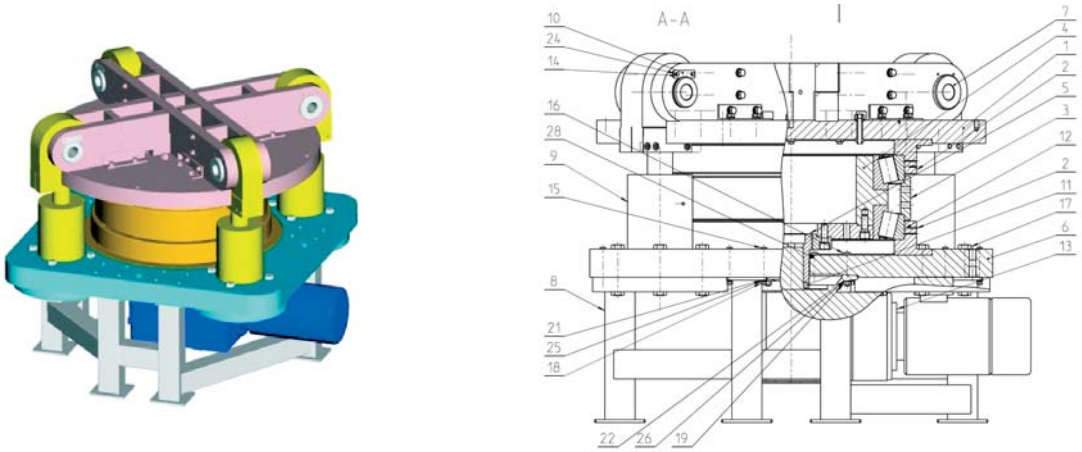

Fig. 3. Testing apparatus for special large-scale bearings

- monitoring part containing certified pressure transducers, temperature, vibration, time and datalogger. This part also includes a PC.

The electric part was designed based on the following:
- input voltage - 3PEN ~ 50 Hz 400V-TN-C-S,
- operating environment – normal, according STN 33 0300 čl.3.1.1 standard.

The design of the electric outfit of the machine of the testing apparatus contains the design of the mechanical arrangement of the distributor, including the electrical connection of devices within the said distributor, electrical connection of devices placed on the testing state and design of the datalogger. The following figure shows the block scheme of the device.

The design of the electromotor and the associated parameters, such as power, RPM, torque etc. are based on the following

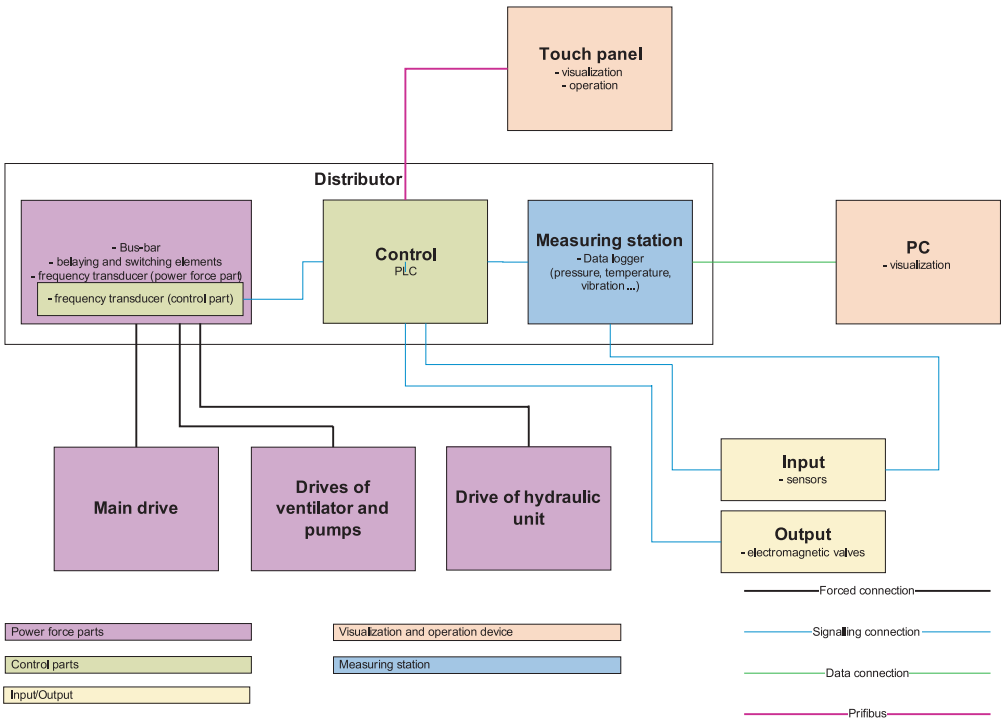

Fig. 4. Block scheme of the device

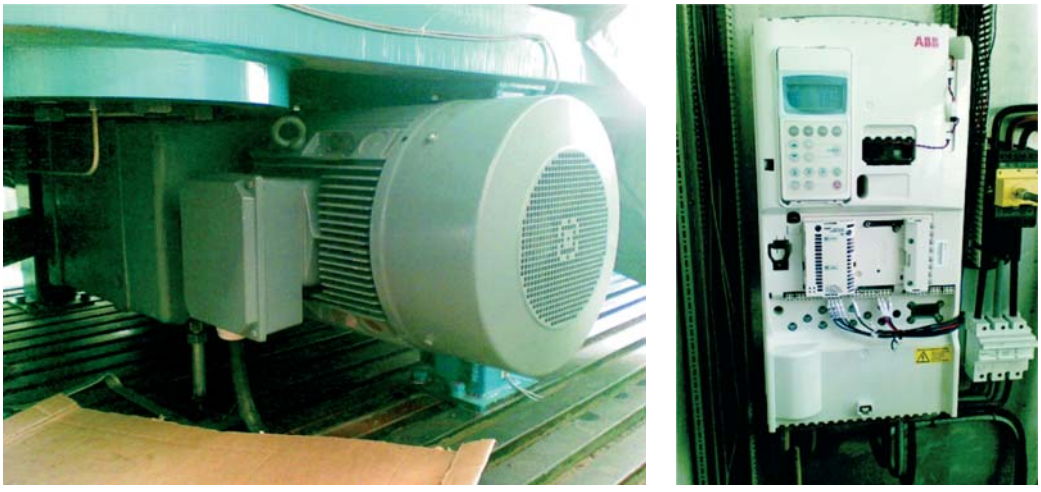

Fig. 5. Asynchronous motor with a bevel-spur gear, frequency transducer

conditions: maximum RPM of the tested bearings should be 40 rev./min. with a maximum load of 4000 kN and the total central momentum of the system must be calculated to the electric drive output shaft. It is also necessary to assure that the electric drive is capable of achieving the required RPM under load within the required time without overloading the motor. An asynchronous motor with a bevel-spur gear shaft was used in the design to assure a safety coefficient of 1.3.

Parameters of the asynchronous motor:
- power output: 55 kW,
- nominal current at 400V: 8.1A,
- nominal revolutions: 1460 rev./min,
- nominal moment: 26.9 Nm.

Gear parameters:
- gear ratio: 5.64.

The asynchronous motor and gear are used to drive the tested bearings through a toothed pinion. The motor is fed via a frequency transducer with direct torque control (DTC). A frequency transducer was necessary because the test state required changes in RPM together with fluid start-up a shutdown along the set rise and fall ramp. The used frequency transducer is manufactured by ABB company, type ACS 800-03E-08A8-4 with the following parameters:
- power output: 4 kW,
- nominal current 8.8 A,
- input voltage Un = 400 V, 50 Hz.

This frequency transducer is placed within the distributor. Other electric devices, such as terminal blocks, fuses, contractors, fuses, 24V DC switched power supply, PLC automat, 230V technological power plugs, datalogger etc. are also placed within the distributor.

An operating unit is used to automate and allow for independent test state execution without the need for human interaction. In this case the SIEMENS S7-CPU224XP PCL automat was used, alongside two expansion modules: EM223 adding digital I/O ports and EM235 adding analogue I/O ports. The PLC automat registers input signals from sensors and switches outputs connected to action units or signalizations. The outputs are switched according to pre-programmed sequences based on the test progress. The mentioned SIEMENS PLC automats (S7-2xx) are programmed in the Step7 – MicroWin programming environment. This software tools allows for the development of virtual logical circuit (PLC automat programming) used to control the device. In the past these logical circuits were built using mechanical switching components – relays, which caused frequent malfunctions, the circuits were complicated, required much maintenance and subsequent modification and changes of work sequences were was limited. However because PLC automats allow the creation of virtual logical circuits it is possible to debug, verify and if necessary also change the circuit without the need for mechanical changes.

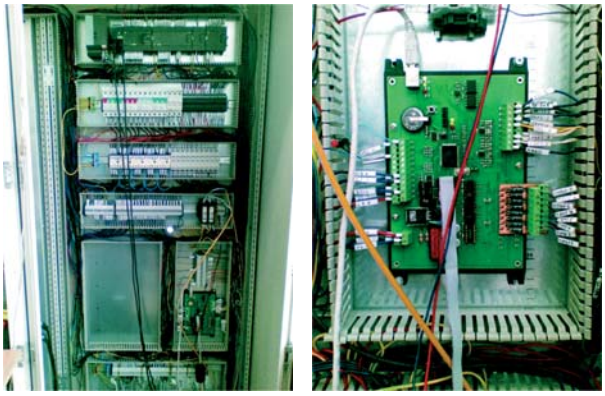

Fig. 6. Layout of the distributor, datalogger

A touchscreen (TP177Micro) was used to reduce the number of mechanical inputs (buttons, switches) and output signaling elements (LED, lighting columns). The PLC automat is connected with the touchscreen via a communication bus (PROFIBUS). The test state can be controlled via the touchscreen and also allows for visual monitoring (graphical symbols or text) about the device state.

Sensors installed in the testing state can be divided into two groups. The first group contains sensors which assure the functioning of the testing state and safe operation thereof. The following sensors are present:
- pressure sensor in the pressure battery,
- security sensor of minimum pressure in pressure battery,
- hydraulic oil temperature sensors,
- sensors of hydraulic oil levels in the oil tank,
- sensors of hydraulic oil filter clogging,
- sensor of lubricating oil temperature in the tank,
- sensor of lubricating oil levels in the tank.

The outputs of these sensors are in digitized form and are fed to the digital input ports of the PLC automat. This group also includes sensors which detect impacts in the tested bearings. The output of these sensors is fed to converters which provide output current within the 4 – 20 mA range which is then fed to analogue input of the PLC automat. The time variation of impact in the tested bearings is shown on the touchscreen in units of decibels.

The second group consists of sensors which measure quantities associated with the bearing test. The following sensors are present:
- sensors of outer bearing rings temperature,
- sensor of environmental temperature,
- sensor of temperature of input lubricating oil,
- sensor of temperature of output lubricating oil,
- sensor of pressure within the hydraulic system,
- vibration sensors.

These sensors have analogue outputs. Sensors of outer bearing rings temperature and environmental temperature are produced by type K thermocouples. Their output is in the form of voltage. Output of sensors recording vibration speed is fed to converters

which provide output current in the 4 – 20 mA range. Output from other sensors is in the 4 – 20 mA range. The output quantities of these sensors must be recorded because they are necessary in the testing procedure. Thus, the output from these sensors is fed to analogue inputs of the datalogger, including the digital signal from the inductive sensor which is used as incremental counter of the number of revolutions.

The datalogger is a device whose purpose is to log and archive the obtained sensor signals. In our case the datalogger is designed based on a personal computer and the measuring board. The hard disk is used as recording medium with the aim of archiving measured data. The designed measuring board used analogue inputs which can be configured to different voltage and/or current input ranges based on required conditions and the sensors used. In addition to the mentioned analogue inputs the card also contains digital I/O ports. Digital ports are used to control the board or inform the system of specific test states. In our case signals from the PLC automat are fed to the board and the board output is then fed back to the PLC automat. This measurement board is equipped with a digital signal processor (DSP), which controls the board, processes the measured data and assures communication with the computer via USB ports.

A driver was programmed to enable communication between the board and the used operating system (Windows XP). This driver is part of the so-called "Datalogger manager" application which has the following use:

- setup hardware parameters for the mutual communication between the operating system and the measurement board,
- control the functioning of the measurement board (measurement start/stop...),
- output the board state and measured quantities onto the computer monitor,
- write acquired data from the measurement board into a database.

The My SQL database system was used due to the number of recorded quantities and the overall test length.

An application was developed to allow not only local but also remote monitoring of the acquired and current test data through

Fig. 7. Web interface allowing data assessment

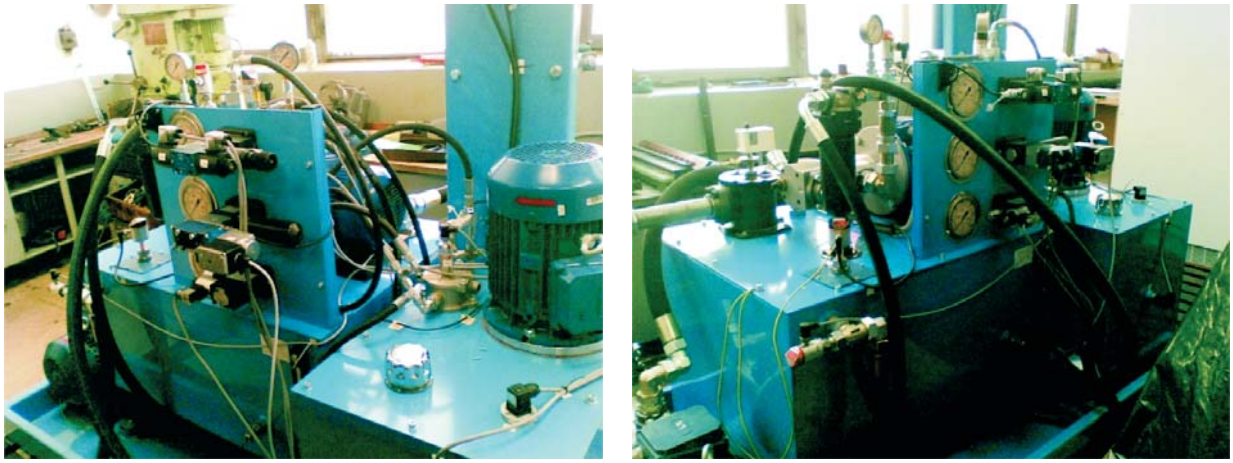

Fig. 8. Hydraulic assembly of the testing apparatus

web interface. This allows any user with access to the internet and the necessary credentials to acquire or browse the measured data.

The application itself contains administrative and user access. The first allows the user to save the measurement. This includes the creation of a new measurement with defined test duration and sampling intervals, choice of monitored quantities and definition of boundary conditions indicating critical or emergency values which result in test termination. Both accesses allow numeric or graphical examination of the recorded data. Individual graphs can be shown for different time segments and number of samples shown in the graph. The acquired time behavior can be saved in picture form onto the computer from which the user has logged on to the remote system database. Data contained in the database can be user-saved either as a text document or in excel data format (xls).

5. Hydraulic part

The hydraulic part of the testing apparatus is divided into two parts – the pressure part, assuring the required pressure in hydraulic cylinders and the lubricating part – assuring bearing lubrication during test execution.

Four hydraulic cylinders form the main component of the pressure part, designed in such a way that each cylinder is capable of exerting a pressure equal to 1000 kN. This application is typical of high pressure which is necessary to obtain the required loading force with small flow rate of the hydraulic oil. This allowed for the use of pressure sources with a constant pressure of 300 bar used to fill the hydraulic cylinders. By using pressure sources it was possible to eliminate the need for constant compressor use, which is used to guarantee system pressure. The required pressure change and the resulting load variations are effectuated during rise and fall time of the bearing test via proportional reductive valve. A mechanical reductive valve is set to the desired value and then used to control the pressure during the test execution. This approach was chosen to automate the bearing testing, where during rise and fall time based on the chosen approach the bearing is gradually loaded and unloaded. The gradual loading and unloading of the bearing is assured by a proportional reductive valve which varies the pressure according to the input voltage magnitude in the 0 – 10 V range from the analogue output of the PLC automat. The proportional reductive valve is characteristic of high pressure losses which translate into frequent pump activation. For this reason the system is switched to the mechanical reductive valve once the required pressure has been reached, resulting on lower pressure losses. This is conditioned by the following criterion: the value of the mechanical reductive valve must be equal to value of the proportional reductive valve at the time of switching. Change of direction of the hydraulic cylinders piston movement is effectuated via switching of the appropriate valve which conducts the hydraulic oil before or after the piston of individual hydraulic cylinders.

The lubricating component of the hydraulic part assures sufficient lubricating texture on the running surface of the tested bearings and to regulate temperature of the bearings within the operating conditions. The lubricating oil is pulled from the reservoir using a pump and passed through a filter and eight nozzles directly onto the running surface of the bearings. The oil flow rate must be equal to 50 l/min to achieve optimal lubricating and cooling effects. The oil residing at the bottom of the testing state must be pumped back to the reservoir due to its high viscosity. Oil levels in the reservoir are monitored via level meter. Oil levels beyond or below the selected threshold indicate malfunctioning of the lubricating system requiring the stoppage of the testing state.

This lubricating part also contains a cooling circuit. If the lubricating temperature exceeds the specified value, a pump is activated and pulls the lubricating oil from the reservoir into the cooler. This cooler is equipped with a ventilator. The cooling cycle is terminated once the temperature of the cooling oil drops to the specified value.

Operation of the hydraulic part is assured by the PLC automat according to preprogrammed sequences.

6. Conclusion

The University of Zilina cooperated with PSL a.s. Povazska Bystrica to develop, construct and build a testing state for testing special, large-scale barrel bearings. Using modern CAD, CAE and PDM systems it was possible to construct this device in relatively short time and components were developed simultaneously. Operation of the testing state is user-friendly and simple thanks to the use of a PLC automat. Automation allows bearings to be evaluated without interruption which is advantageous from a time point of view. This testing state is unique and perhaps one of its kind and allows testing of special, non-standard bearings. However other sensor types or sensors of different quantities can be used because the data logger design was designed with flexibility and universality in mind.

This work was supported by the Slovak Research and Development Agency under the contract No. APVV-0505-07

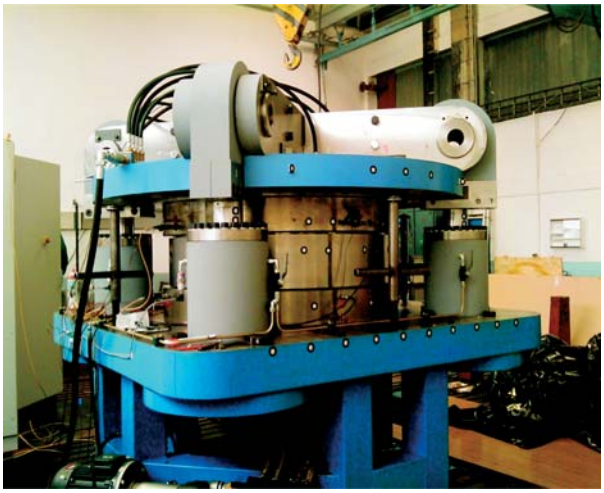

Fig. 9. Operation of the testing apparatus

References:

[1] http://www.ozeport.sk/zdroje/veterna.html
[2] http://www.vestas.com/en/wind-power-solutions.aspx
[3] http://www.pslas.com/sk/index.php

Zuzana Ondrova *

DYNAMIC ANALYSIS OF A 4–AXLES RAILWAY VEHICLE MODEL

The paper deals with using dynamic simulations in fields of construction, production and operating of railway vehicles. It contained process of dynamics solution of choices referent vehicle by the help special solution software – MSC ADAMS. The creating of virtually model included creating model for railway vehicle and the model of track which is assigned for motion of railway vehicle.

In the end of paper there are summary of obtained data from dynamic analysis which give us integrated view of railway vehicle behavior by the run on given track.

1. Introduction

Rising demands on construction, used materials and rail vehicle technical equipment also increased the overall complexity, software dependency and last but not least also the total costs of the vehicle production. Currently, vehicle manufacturers focus on vehicle safety, taking into account the overall comfort and operating safety of the vehicle itself and also to provide additional comfort for passengers and service staff, increase the transport capacity while, at the same time minimizing the total and maintenance costs. However, to be able to achieve the afore-mentioned goals, alternative development and production routines must be used in the forthcoming railway vehicles.

Prior the real-life deployment of a new technical solution, we must test all vehicle parameters and properties via practical experiments.

Simulations and analyzes are gaining more and more attention in the process of vehicle production. This allows us to obtain data about vehicle operating behavior from various, sometimes highly extreme conditions before the actual production of a new vehicle is launched. This way we can study effects of input parameters on the operation, safety, service life and reliability of single vehicle components, railway vehicles or complex train sets.

By data evaluation from experimental measurements or from computer simulation we can evaluate railway vehicle dynamics.

2. Railway Vehicles Simulation Computations

Simulation computations represent a feasible means of analyzing railway vehicles. In our case they consist of analysis of dynamic properties. By entering relevant input parameters we can obtain vehicle evaluation details pertaining to the vehicle behavior on the track.

It is advantageous that obtaining relevant parameters about vehicle motion we don't have to perform any real-life measurements on the railway vehicle or the actual track. But it is more demanding to obtain correct values of geometric, mass and flexible joint parameters of a mechanical system for creating a mathematic and subsequently a virtual vehicle model. Track parameters are also very important because they can severely influence all our computations.

2.1 Virtual model

To create a dynamic model, one must have deep knowledge of mechanical system properties – in our case those pertaining to the model of the railway vehicle. This data analysis is performed on the basis of existing railway vehicles used in practical real-life scenarios. In practice we know that the production vehicle contains a broad spectrum of properties, some of which are more or less needed. These properties are mutually interconnected in a very narrow manner.

Regardless of which vehicle is used, it stands to reason that without sufficient knowledge of the given problem, parameters and an express definition of simulation computations purposes the output will only be a mixture of partial or incomplete results. [2].

2.2 Computation model

The computational model can be created on the basis of various points of view but the critical criterion is always the purpose of

* **Zuzana Ondrova**
Department of Traffic and Operating Technique, Faculty of Mechanical Engineering, University of Zilina, E-mail: zuzana.ondrova@fstroj.uniza.sk

the analysis. Models can be viewed in a multitude of manners, including the following representations: geometrical, plane or space models, furthermore as linear or nonlinear models and also according to the type of analyzed field (e. g. frequency, time domain etc.)

The computation model used in my work is a nonlinear model whereby the bogie frame and car body are rigid and interconnected with elastic joints. Dynamic simulation was carried out in the time domain.

Solution of mathematical model is based on finding all characteristic numbers and characteristic vectors. The majority of used mathematic methods are assigned to the solution of characteristic number standard problem, meaning that the general problem must first be transformed into a standard problem.

Of the available classic solution methods, the Jacob's method of rotation is very convenient in our case. However, other methods, such as Rayleigh-Ritz method, method of inverse iteration, Gramm-Schmidt orthogonal method, Lanczo´s method etc. may also be used. [2].

3. Programs for Simulation Computations

Current computer assistance program products include a range of intelligent tools and software modules which enhance the efficiency of the engineer. These systems analyze possible solutions and reject those which are unsuitable due to restrictions imposed by physical laws or restrictions defined within the project.

The MBS (Multi Body Simulation) technology is most commonly used in solution and evaluation of various dynamic properties of mechanical systems. It is based on simulation of mechanical systems (MSS) and the subsequent definition of local stresses in every instant of time. MBS offers simple simulation of active components such as shafts, crank shafts etc. In some cases it is possible to use history of loading results obtained by MBS when solving real-life mechanism by FEM (finite element method).

MBS has one great advantage – it allows the evaluation of various effects that influence the system. In the case of railway vehicles, it is possible to detect component fatigue depending on suspension settings, operation style or track quality.

3.1 Aplications – ADAMS/Rail

Dynamic analysis problems can be solved using software specifically designed for the field of railway vehicles. The Rail module is intended for simulation computations of railway vehicles. This module performs dynamic simulations of mechanical system parameters not only with arbitrary structures but also for a combination of rigid and flexible bodies upon which inertia, gravity and excitation forces are exerted.

To assure proper functioning of all stages of railway vehicle development, testing, production, construction and operation, the program must be interfaced with all leading producers to allow data sharing and data interchange.

The option to create an animated model showing the actual movement of the object and a graphical description of all physical parameters such as speed, acceleration, shift, forces, etc. are all useful extensions of this program. This module also includes the computation of mechanical system characteristic frequency and also various pathways of vehicle excitation.

It is important to create a model that is as accurate as possible – otherwise simulation results will be unpredictable. Thus, we must know how to prepare input parameters and how to use them to achieve our goal purpose.

In addition to the previous, the vehicle model must be appropriately combined with the track model to assure complete evaluation during dynamic simulation and to mimic the railway vehicle behavior when running on tracks [1].

4. Dynamic Analysis of a 4-axle two – Bogies Railway Vehicle Model

The reference vehicle used in the dynamic analysis is a 4-axle two – bogies coach wagon that is otherwise known as ERRI Wagon. The vehicle model is equipped with springs and dampeners with nonlinear characteristics. Geometric parameters, mass parameters and parameters of elastic joints are identical to those present in the simulated model in MSC ADAMS/Rail.

Wheels of the wheelset have a wheel profile of S1002. The axle guiding in bogie frame is supported by a bail arm. Wheelsets are connected to the bogie frame spring via primary suspension. This system consists of a coil spring and hydraulic dampers located between the axle box and the bogie frame. The car body is connected to the bogie frame spring via a system of secondary suspensions [2].

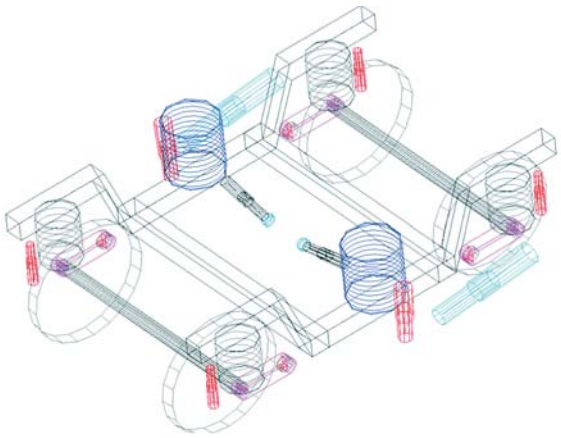

Fig. 1 Bogie frame model (ADAMS/Rail)

4.1 Vehicle model

The vehicle model consists of the bogie frame (bogie subsystem) and a car body (subsystem of car body) model. Each subsystem assembly contains several construction components, in addition to the car body model which consists of one complex unit. These parts have properties and geometric parameters based on real-life railway vehicles.

The assembly of the ERRI model is comprised of the following three subsystems:

- *car body,*
- *front bogie,*
- *rear bogie.*

To assemble the model, all components (wheelset, bogie frame, suspension (primary and secondary), dampers (lateral, vertical and anti-yaw dampers) etc.) must be defined. Pre-existing templates can also be modified according to our own requirements by simply changing the model parameters [1].

Each simulation/analysis takes into account real-life data. If the desired requirements are not met, it is necessary to change the geometric form of the model or to add data otherwise neglected at the stage of model reduction (additional friction, definition of components elasticity which are not rigid, etc.). The simulation can be rerun several times until goal output parameters are met.

4.2 Track model

The track model is based upon real-life geometrical data, specifically the track is located between **SURANY – ULANY NAD ZITAVOU**. I chose this track on the basis of data availability. This track is representative of dynamic analysis due to the presence of many curves with various radius parameters and the resulting sections of transit curves and ascending rails, important for general evaluation of vehicle behavior during operation on the given track.

The chosen track has a length of 5882 m and there are five right and a three left-hand curves. The complete track data was imported into the simulation software (all curve radiuses, degree of rail incline and track leveling). Fig. 4 shows the track overview. The track radius and particular lengths of total track length are displayed in Fig. 4. The maximum vehicle speed allowed on the whole track is 60 km/h. All my computations were computed at this speed. Vehicle derailment protection was analyzed and compared for variants of rail profiles and cant rail UIC60/1:40, S49/1:40 and S49/1:20 [2].

5. Vehicle Derailment Protection

Vehicle derailment protection is defined as the ratio between the guide force and the wheel force. Results which are presented in Fig. 6 represent a variation of forces in wheel/rail interaction.

To simplify the orientations in these results we can state that:

- The bottom part of the graph describes the track geometry.
- The vertical axis on the left-hand side of graph specifies the reciprocal of curve radius,
- The vertical axis on the right-hand side of graph specifies the degree of incline value of outer stretch of rails.

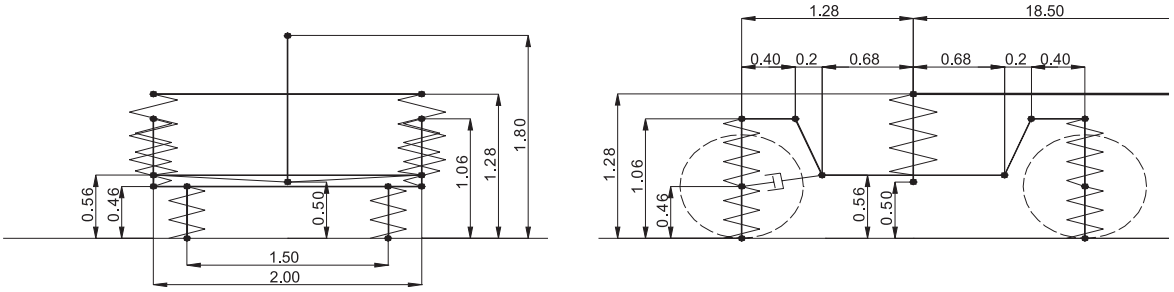

Fig. 2 Geometric parameters of vehicle model [2]

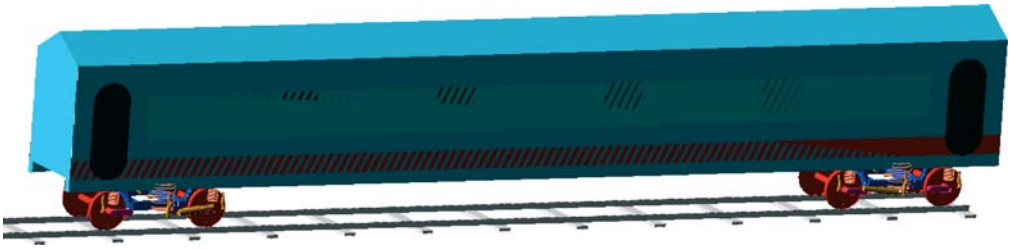

Fig. 3 Vehicle model ERRI (ADAMS/Rail)

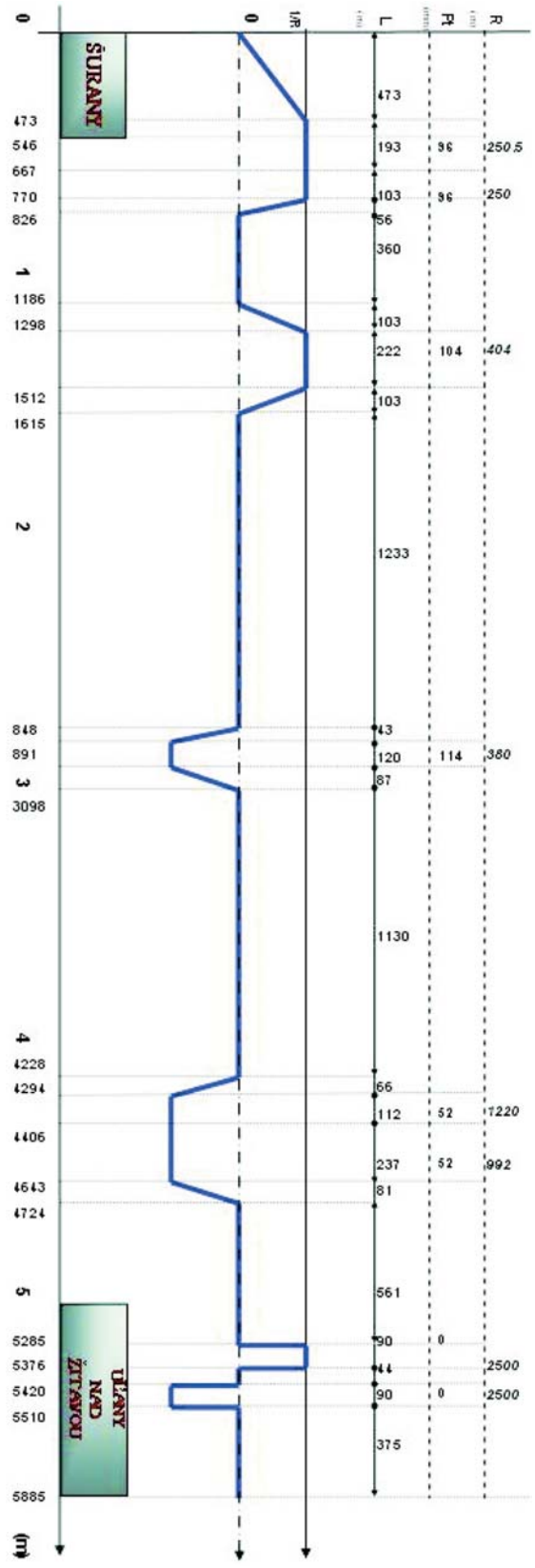

Fig. 4 Track overview diagram [2]

- The upper half and positive values of radius are characteristic of right-hand curves, the lower half and negative values of radius are characteristic of left-hand curves.
- The degrees of incline are numbered upwardly from zero (from below).

In the other graphs there are descriptions of wheel forces (Q) in [N], guide forces Y [N] and vehicle derailment protection (BPV), which have a non-dimensional value [-]. Identification of single positions on vehicle bogies is in conformance with marked output (Fig. 5) signal and can be obtained at the end of the simulation computations [2].

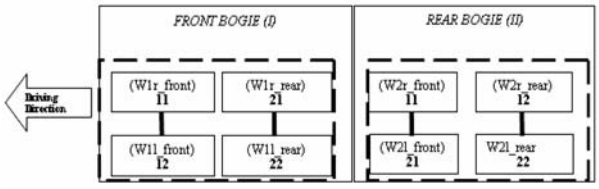

Fig. 5 Location of positions in vehicle [2]

6. Conclusion

From Fig. 6 it is evident that the majority of the load is exerted onto the wheel during curve cornering – which is the thread up wheel of the first wheelset from the first bogie of vehicle. The right guide force creation and transmission in the horizontal plane is located within this point. The second wheel of the thread up wheelset is assigned to decrease the wheel and also guide force. Influence of transient performance in the force range can be seen in the transit curve. On locally straight tracks the wheel force nominal values are stable and the values of guide forces are close to zero.

Variation of forces confirmed the running stability of our vehicle and the relationship between the vehicle virtual model and the track is comparable to the expected real-life conditions.

The results of wheel and guide forces as well as vehicle derailment protection are all within the allowed limits. The worst ratio of vehicle derailment protection on this section is 0.5, which is less than the permissible value of 1.2 for wheel profile S1002.

The created vehicle model can be used in other simulations by simply changing some of the parameters of the vehicle and can also be employed when evaluating passenger comfort if various acceleration forces that act upon the vehicle are obtained.

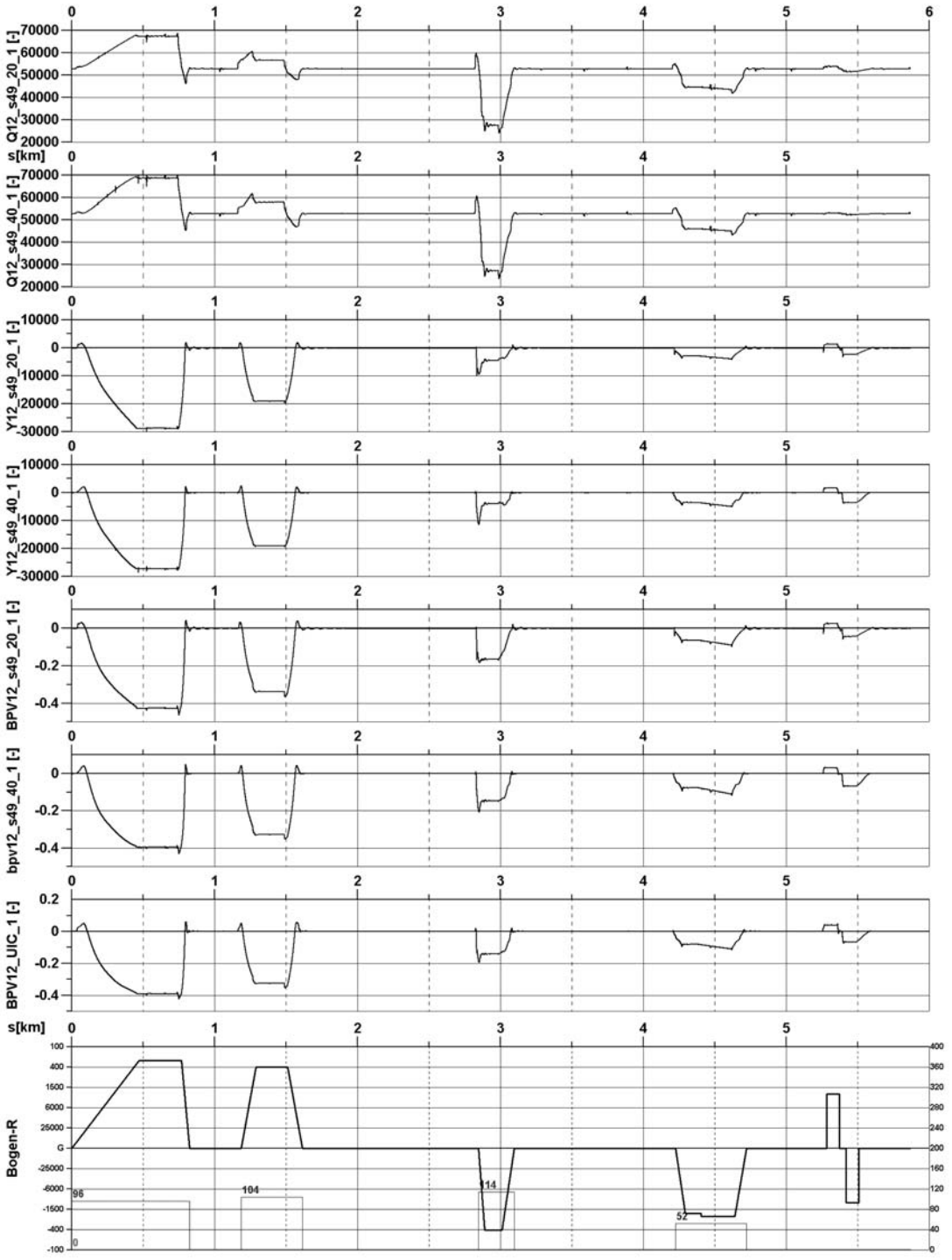

Fig. 6 Evaluation of chosen parameters for rail profile S49 and cant rail / 1:20 a 1/40 and UIC [2]

References

[1] ONDROVA, Z., GERLICI, J., LACK, T.: *Analysis of Dynamical Properties for Rail Vehicle at Travel wake of Real Track (in Slovak),* SETRAS 2006, ISBN 80-969165-8-0. pp. 163-169. EDIS – University of Zilina, 2006.

[2] ONDROVA, Z. (2008): *Dynamical Simulations of Travel Rail Vehicel wake of Real Track (in Slovak)*, Dissertation thesis, 2008.

Zdena Kralova – Eva Skorvagova – Juraj Ruttkay *

SOME EXTRALINGUAL VARIABLES OF L2 PHONIC COMPETENCE

The study assessed the relation between the overall degree of perceived foreign accent in non-natives' English speech and some extralingual factors. These variables include musical ability, phonic mimicry ability and type of personality. Five native speakers of English were asked to auditorily evaluate the samples of free English speech produced by each of 79 non-native talkers using the equal-appearing interval scale. The 5-point scale was used to rate each of the variables for each non-native speaker and the interclass correlation coefficients were calculated to identify the most important predictors of L2 pronunciation quality. The findings reported may be important for the learning and teaching second languages.

1. Introduction

This paper reports research which attempts to identify factors which explain the variance in a second language (L2) phonic competence. The authors investigate the influence and interrelatedness of extralingual variables (musical ability, phonic mimicry ability and type of personality), usually considered significant in foreign language acquisition, especially on the level of phonology, i. e. in acquiring the phonological subsystem of a foreign language. The data collected in empirical research presented in this paper show that, although the influence of some of these variables is debatable, it is not always possible to single out one of them and to disregard the rest of them. It is not always possible to say which of these influences will prevail under some circumstances either. The acquisition of a phonological system is an immensely complex process, influenced by numerous factors simultaneously. We tried to "capture" the possible influence of three potentially relevant factors, usually intuitively recognised, by professionals and laymen alike, as highly influential.

For the last 40 years, beginning with the classic article of Asher and García [1], the variety of variables influencing the acquisition of the phonological system of a foreign language has been investigated in a large number of experimental studies. Although considerable individual variation can be observed in adults' mastery of L2 production and perception, the L2 literature, as well as our common experience as language users, generally indicates the most adult L2 learners will permanently speak the L2 with a foreign accent. One interpretation of this observation is, in the scientific study of foreign accent, that success in acquiring the phonetics and phonology of an L2 is dependent on a number of variables which influence the performance of individual L2 users. Identifying such factors may be important for the teaching and learning foreign languages. The studies of the issue published so far differ greatly in terms of the languages, subjects, methods or procedures examined. These differences appear to be responsible for the often divergent results of the studies. The relative importance of many factors is uncertain because many variables relating to subject characteristics tend to be confounded, and because of the lack of adequate experimental control in some studies.

2.Acquisition of L2 pronunciation

2.1. L2 pronunciation research

The acquisition of the phonetic/phonological component in a second language is a complex and dynamic process which is influenced by the context and conditions in which the language is learned. The overall quality of L2 pronunciation is likely to vary depending on the characteristics of the subjects. The subjects examined in previous studies have differed in a number of potentially important ways. Most previous studies have examined English as the target L2 being learned. The native languages spoken by the subjects have been far more diverse. The nonnative subjects mostly differed in L2 experience, the age of L2 onset, the length of residence in L2-speaking country, the degree of motivation to speak an L2 and many other variables [e.g., 2 – 11]. The fact that the subjects examined in previous research differed along the dimensions just described often makes direct comparisons across studies problematic. Thus, this should not lead one to conclude that the degree of L2 pronunciation accuracy cannot be scaled reliably and validly.

The studies of the overall degree of L2 foreign accent have also differed in terms of the techniques used to elicit nonnative speech samples. In most studies, subjects have been asked to read words, sentences or paragraphs [e.g., 1, 3, 7]. In a number of

* **Zdena Kralova[1], Eva Skorvagova[2], Juraj Ruttkay[3],** Faculty of Science, University of Zilina, Slovakia
[1] Department of English Language and Literature, E-mail: zdena.kralova@fpv.uniza.sk
[2] Department of Pedagogy, Psychology and Social Science
[3] Department of Music

studies, subjects have also been asked to produce samples of free (i. e., extemporaneous) L2 speech [e.g., 12 – 15]. And finally there have been studies in which subjects were asked to repeat speech materials after hearing a native speaker model in a direct repetition technique [8] or a delayed repetition technique [16]. Some researchers have used more than one elicitation technique [e.g., 12, 14, 17].

A control group of native speakers was recruited in most of the studies cited so far in addition to groups of nonnative subjects. The numbers of raters used in various L2 pronunciation studies have differed greatly, ranging from just one [18] to 85 [19]. It is not known at present how many raters are needed to provide a reliable estimate. Unfortunately, not all the studies have included a native group [20, 21]. This may lead to several problems – for example, it remains uncertain how the native speaker would performed under the specific circumstances of a particular experiment. One important methodological question pertains to the characteristics of the listeners. In some studies, naive raters were recruited to evaluate speech samples [e.g., 1, 8]. In other studies, "expert" raters such as linguists or teachers have participated [e.g., 15, 22]. [14] reported that experienced raters generally perceived a higher degree of L2 foreign accent in nonnative speech than inexperienced raters, while [7] found no significant differences between experienced and inexperienced raters. In Slovakia it seems to be a problem to recruit the homogeneous group of English native speakers who would be willing to participate in an experiment (often time consuming one) and who would not be trained or experienced EFL teachers.

The listeners who evaluate L2 speech usually use a rating scale to indicate the quality of L2 pronunciation they perceive in a speech sample. No standard scale for measuring the accuracy of L2 pronunciation has been developed so far. The equal-appearing interval (EAI) scales differ in resolution. A 5-point scale has been used most commonly [e. g., 7, 12, 13]. [8, 22] employed a continuous scale to evaluate foreign accent. [23] carried out a research to determine whether foreign accent is a metathetic continuum (a continuum that can be divided into equal intervals ranging from high to low) or a prothetic continuum (a continuum that is not amenable to linear partitioning). They indicated that foreign accentedness is a metathetic continuum, which means that it is appropriate to use an EAI scale and found that a 9-point (or 11-point) scale should be used to rate L2 speech samples for degree of foreign accent.

2.2. Factors influencing L2 pronunciation

The differences between studies in design and methodology have led researchers to draw rather conflicting conclusions about the influence of certain factors on L2 pronunciation. The factors that received the most attention in the literature are undoubtedly the L2 onset age and the length of stay in an L2-speaking environment. Unfortunately, hardly any study in the existing literature [24] has examined the changes in degree of L2 pronunciation accuracy in a longitudinal design. Affective and social factors as well as individual aptitude have been seen as possible predictors of the second language phonetic performance [2]. Contact with native speakers has also been reported as having a significant influence on the second language pronunciation [14, 25, 26]. Specific phonetic training has generally been found to be positively associated with phonetic development in L2. Other factors such as attitudinal and motivational variables have sometimes – though not always – proved to be influential [14]. A number of other factors related to the speakers' backgrounds, including gender [1, 8, 14], mimicry ability [14, 25, 26] and professional motivation [27] have also been found to be significantly correlated with global accentedness scores in at least some studies. These results, however, have not been consistently replicated, and require further examination before any firm conclusions can be drawn.

Musical ability

Musical ability has as yet not been identified as one of those variables that have an important influence on L2 pronunciation quality [14]. However, some hypotheses assume that there is a positive correlation between music perception/production and the perception/production of the sounds of L2. It has been partly verified that there is a significant correlation between music production and the production of vowels [20]. Singing talent has been linked to the ability to mimic pronunciation by [8]. [28] has demonstrated that this skill is not improved by musical training and so there is a chance that it is innate and cannot be altered by education.

Mimicry ability

Pronunciation is generally taught on the basis that imitation is the natural mechanism for its acquisition. Except for one study [8] the ability to mimic unfamiliar speech sounds has repeatedly been identified as a significant predictor of L2 pronunciation quality [14, 25, 26]. The imitation paradigm [29] has shown that subjects shift their production in the direction of the target, indicating the use of episodic traces in speech perception. Recent studies have shown that traces of episodic memory are retained and used in speech perception, and that both speech perception and production are more plastic than previously considered [e. g., 30].

Type of personality

Findings from several studies [e.g., 31] showed that anxiety significantly contributes to students' success in learning L2. This affective dimension of L2 learning involves having difficulty concentrating in the class, feeling afraid, embarrassed or uncomfortable to speak in L2. Extroversion and introversion have been discussed as personality factors in second language learning [e.g., 32], though the contribution of either factor to learning is not clear. Personality factors such as self-esteem, inhibition, anxiety, risk-taking and extroversion, are thought to influence second language learning because they can contribute to motivation and the choice of learning strategies.

3. Methodology

Speakers

Seventy-nine (59 female and 20 male) subjects examined in the study were Slovak first-year university students enrolled in the English Language and Literature course. They were approximately at an intermediate level of English proficiency, aged between 18 and 20 and had typically started learning English at elementary school with a focus on grammar-based instruction. The majority of them had never lived in an English-speaking country.

Assessors

5 native English control subjects (3 American – 2 male, 1 female; 2 British – 1 male, 1 female) were asked to auditorily evaluate the English texts produced by each of the 79 talkers. The raters were English native speakers more or less experienced in ELT who had lived in Slovakia for several months/years.

The assessor of musical ear and memory test was an expert musician, the assessor of the phonic mimicry ability test was a phonetician and the marker of the personality questionnaire was a psychologist (Table 1). All assessors were asked to use a five-point scale to indicate the degree of relevant material and to rate each talker by a mark on a scale from 1 (low) to 5 (high) (Table 2).

Material

Pronunciation samples (a free, extemporaneous talk in English), direct phonic imitation and musical tasks were recorded on a recorder with a condense microphone for further analysis and reference. The collection took place in classrooms at the University of Zilina and required approximately 25 minutes for each student. The information concerning personality was elicited from the participants by the way of a questionnaire which required 50 minutes to complete (Table1).

Procedure

Relying on the data most frequently presented in research papers and theoretical discussions, we aimed primarily at investigating the possible influence of three extralingual factors[1)] (EF1 – musical ability, EF2 – phonic mimicry ability, EF3 – type of personality) upon the pronunciation accuracy observed in the interlanguage of learners of English as a foreign language.

Native speakers were asked to auditorily evaluate the samples of free English speech (3 minutes) produced by each of the non-native talkers using the equal-appearing interval 5-point scale. An average rating was obtained for each speaker and the variable English phonic competence (EPC) was computed by averaging across each rater`s score.

The musical ability of the subject was tested in a basic test of musical ear and memory (10 minutes). The test was performed and assessed by a musician in a 5-point scale. The English words and phrases were modelled on the tape and repeated immediately afterwards to test the direct mimicry ability (10 minutes). The 16-factor questionnaire [33] was administered in a group form without any time limit given. Scoring was processed using Psychosoft System Brno. The global personality factor EX Extroversion appeared to be the most important for the profile interpretation.

The data were collected, then evaluated. The interclass correlation coefficients (r) were calculated to identify the significant predictors of L2 pronunciation quality (Table 3). To assess their relative contribution to EPC, the variables were submitted to a simple correlation. Correlation coefficients were calculated for each factor by applying the scoring coefficients generated by the principal component analysis to standardized values for subjects' responses. The variables were correlated with the total pronunciation rating and the correlation coefficients (r) were obtained. The result is statistically relevant for the phenomena with the correlation coefficients higher than the critical values for the variable length 79 on the 0.05 level = 0.2787. For lower values the correlation is not evident. The closer is the value to 1.0, the stronger is the correlation between the variables.

4. Results

Testing methods Tab. 1

Extralingual factor	Abbr.	Testing method
musical ability	EF1	perceptual assessment (J. Ruttkay)
phonic mimicry ability	EF2	perceptual assessment (Z. Kralova)
type of personality	EF3	16-factor personality questionnaire (E. Skorvagova)

Evaluation scale Tab. 2

Evaluation scale					
	5	4	3	2	1
EPC	excellent	very good	good	average	poor
EF1	excellent	very good	good	average	poor
EF2	excellent	very good	good	average	poor
EF3	extrovert (10 – 8 points)	neutral (7 points)	neutral (5 – 6 points)	neutral (4 points)	introvert (3 – 1 points)

[1)] intralingual factors – characteristics related to a language system;
paralingual factors – temporal characteristics partly related to a language system;
extralingual factors – characteristics not related to a language system;

Correlation of EPC and EF Tab. 3

Student	EPC	Extralingual factors		
		EF1	EF2	EF3
1	**2.6**	3	3	4
2	**3.2**	5	4	3
3	**2**	3	3	2
4	**2.2**	2	2	4
5	**2**	1	2	4
6	**1.6**	2	1	4
7	**2.2**	1	2	3
8	**2.4**	3	3	4
9	**2.4**	3	2	3
10	**1.8**	3	4	2
11	**2.2**	2	3	2
12	**2.2**	5	1	4
13	**1.6**	5	4	5
14	**3.6**	4	2	4
15	**3.2**	3	4	3
16	**1.8**	3	3	3
17	**3.4**	5	4	4
18	**3.2**	5	5	3
19	**2.8**	5	3	4
20	**2.8**	4	3	3
21	**2**	2	1	3
22	**2**	2	2	3
23	**1.6**	1	4	2
24	**2.6**	5	5	3
25	**4.4**	3	5	5
26	**1.6**	1	1	3
27	**2.6**	2	3	4
28	**1.8**	4	1	2
29	**2.8**	5	3	4
30	**2.8**	1	3	4
31	**2**	4	3	3
32	**3.4**	3	3	4
33	**3.2**	4	2	5
34	**2.2**	2	3	4
35	**2.4**	2	4	3
36	**2.8**	3	1	2
37	**2.4**	1	2	4
38	**3.8**	5	5	2
39	**3.2**	2	1	3
40	**2.4**	3	4	5
41	**3.2**	5	3	3
42	**4.6**	5	5	4
43	**2.6**	4	3	3
44	**1.4**	2	2	4
45	**2.6**	1	3	4
46	**3.4**	1	3	2
47	**3**	4	4	2
48	**2.6**	2	1	3
49	**2.4**	3	1	4
50	**3.4**	5	2	3
51	**2.4**	3	1	3
52	**3**	2	1	3
53	**2.2**	1	2	3
54	**2.8**	3	2	3
55	**2.4**	2	4	4
56	**3.4**	3	2	3
57	**2.8**	2	1	3
58	**1.6**	1	4	4
59	**2.6**	2	2	3
60	**3.2**	5	3	3
61	**2.4**	4	1	3
62	**2.4**	1	4	2
63	**3.4**	1	5	4
64	**3**	1	1	4
65	**2**	1	3	3
66	**2.6**	3	3	4
67	**2.6**	1	1	3
68	**3.4**	1	2	3
69	**3.6**	1	3	4
70	**1.8**	1	1	3
71	**2.6**	5	2	4
72	**2**	5	3	3
73	**3**	2	1	4
74	**1.8**	3	4	3
75	**2.2**	4	1	4
76	**1.4**	5	1	2
77	**2.8**	3	2	3
78	**2.6**	3	4	3
79	**2.4**	2	3	3
Mean	**2.59**	**2.85**	**2.63**	**3.32**
r	**-**	**0.2298**	**0.2881**	**0.1387**

5. Conclusions

Preliminary analysis revealed that much the same EPC ratings were provided by the five raters. The mean for all the native speaker evaluations was 2.59 and there was a standard deviation of 0.73. Initially, the three measured variables were correlated with the total pronunciation ratings (0.2787 on the 0.05 level). These produced the following correlations:

EF1 (musical ability) $r = 0.2298$
EF2 (mimicry ability) $r = 0.2881$
EF3 (type of personality) $r = 0.1387$

The correlation between EPC and the factors is rather weak. The results show that only one of the factors (EF2) proved relevant for the differences in the foreign language pronunciation rating and no statistically significant correlation could be established between the variables EF1 and EF3.

The study assessed the relation between the overall degree of the perceived foreign accent in non-natives' English speech and three extralingual factors which are supposed to affect L2 pronuncia-

tion. The empirical data clearly indicated that the so-called foreign accent phenomenon is a highly complex one. Namely, it is not always possible to detect a clear corelation between the observed level of phonic performance of a foreign language learner and any of the factors usually considered crucial for the foreign accent reduction. Thus it is not always possible to isolate those variables which are considered the most important. The mutual influence of a number of factors appears to be so complex that the influence of each and every one of them cannot be singled out and analysed independently, without taking all the others into consideration.

Note, however, that longitudinal research is needed to determine more precisely at what point in L2 learning, if any, the individual factors cease to have an effect on the pronunciation of L2. The results found in this study could prove to be of interest for language teaching methodology as it should be the goal of L2 teachers to find the most efficient methodology for L2 (not only pronunciation) learning that would take into consideration the individual differences between students, thus making the acquisition of L2 a more effective, enjoyable and less frustrating experience.

References

[1] ASHER, J. J., GARCIA, R.: *The Optimal Age to Learn a Second Language,* The Modern Language Journal, vol. 53, 3/1969, p. 334–341.

[2] FLEGE, J. E.: *A Critical Period for Learning to Pronounce Foreign Languages,* Applied Linguistics, vol. 8, 2/1987, p. 162–177.

[3] FLEGE, J. E.: *Factors Affecting Degree of Perceived Foreign Accent in English Sentences,* Journal of the Acoustical Society of America, vol. 84, 1/1988, p. 70–79.

[4] SINGLETON, D.: *Language Acquistion: the Age Factor,* Clevedon: Multilingual Matters Ltd., 323 p., 1989.

[5] PATKOWSKI, M. S.: *Age and Accent in a Second Language,* Reply to James Emil Flege, Applied Linguistics, vol. 11, 1/1990, p. 73–89.

[6] FLEGE, J. E.: *Perception and Production: the Relevance of Phonetic Input to L2 Phonological Learning,* Crosscurrents in Second Language Acquisition, T. Heubner and C. A. Ferguson (eds.). Philadelphia: John Benjamins, p. 249–289, 1991.

[7] BONGAERTS, T., VAN SUMMEREN, C., PLANKEN, B., SCHILS, E.: *Age and Ultimate Attainment in the Pronunciation of a Foreign Language,* Studies in Second Language Acquisition, vol. 19, 4/1997, p. 447–465.

[8] FLEGE, J. E., MUNRO, M. J., MacKAY, I. R. A.: *Factors Affecting Strength of Perceived Foreign Accent in a Second Language,* Journal of the Acoustical Society of America, vol. 97, 5/1995, p. 3125–3134.

[9] BIALYSTOCK, E.: *The Structure of Age: in Search of Barriers to SLA,* Second Language Research, vol. 13, 2/1997, p. 116–137.

[10] FLEGE, J. E., FRIEDA, E. M., NOZAWA, T.: *Amount of Native-Language (L1) Use Affects the Pronunciation of an L2,* Journal of Phonetics, vol. 25, 2/1997, p. 169–186.

[11] PISKE, T., MacKAY, I. R. A., FLEGE, J. E.: *Factors Affecting Degree of Foreign Accent in an L2: a Review,* Journal of Phonetics, vol. 29, 1/2001, p. 191–215.

[12] OYAMA, S.: *The Sensitive Period for the Acquisition of a Nonnative Phonological System,* Journal of Psycholinguistic Research, vol. 5, 3/1976, p. 261–283.

[13] PIPER, T., CANSIN, D.: *Factors Influencing the Foreign Accent,* The Canadian Modern Language Review, vol. 44, 3/1988, p. 334–342.

[14] THOMPSON, I.: *Foreign Accents Revisited: the English Pronunciation of Russian Immigrants,* Language Learning, vol. 41, 2/1991, p. 177–204.

[15] KRALOVA, Z.: *Slovak-English Phonic Interference (in Slovak)*, Faculty of Science, University of Zilina, 100 p., 2005.

[16] FLEGE, J. E., YENI-KOMSHIAN, G., LIU, H.: *Age Constraints on Second Language Acquisition,* Journal of Memory and Language, vol. 41, 1/1999, p. 78–104.

[17] MARKHAM, D.: *Phonetic Imitation, Accent, and the Learner*, Lund: Lund University Press, 1997, 269 p.

[18] SNOW, C. E., HOEFNAGEL-HOHLE, M.: *Age Differences in the Pronunciation of Foreign Sounds,* Language and Speech, vol. 20, 3/1977, p. 357–365.

[19] NEUFELD, G. G.: *Towards a Theory of Language Learning Ability,* Language Learning, vol. 29, 2/1979, p. 227–241.

[20] TAHTA, S., WOOD, M., LOEWENTHAL, K.: *Foreign Accents: Factors Relating to Transfer of Accent from the First Language to a Second Language,* Language and Speech, vol. 24, 2/1981, p. 265–272.

[21] ELLIOT, R. E.: *Field Independence/Dependence, Hemispheric Specialization, and Attitude in Relation to Pronunciation Accuracy in Spanish as a Foreign Language,* The Modern Language Journal, vol. 79, 3/1995, p. 356–371.

[22] FLEGE, J. E., FLETCHER, K. L.: *Talker and Listener Effects on Degree of Perceived Foreign Accent,* Journal of the Acoustical Society of America, vol. 91, 1/1992, p. 370–389.

[23] SOUTHWOOD, M. H., FLEGE, J. E.: *Scaling Foreign Accent: Direct Magnitude Estimation Versus Interval Scaling,* Clinical Linguistics and Phonetics, vol. 13, 5/1999, p. 335–449.

[24] MEADOR, D., FLEGE, J. E., Mac KAY, I. R. A.: *Factors Affecting the Recognition of Words in a Second Language,* Bilingualism: Language and Cognition, vol. 3, 1/2000, p. 55–67.

[25] SUTER, R. W.: *Predictors of Pronunciation Accuracy in Second Language Learning,* Language Learning, vol. 26, 2/1976, p. 233–253.

[26] PURCELL, E. T., SUTER, R. W.: *Predictors of Pronunciation Accuracy: An Examination,* Language Learning, vol. 30, 2/1980, p. 271–187.
[27] MOYER, A.: *Ultimate Attainment in L2 Phonology,* Studies in Second Language Acquisition, vol. 21, 1/1999, p. 81–108.
[28] MORGAN, C.: *Musical Aptitude and Second-Language Phonetics Learning: Implications for Teaching Methodology,* Simon Fraser University, PhD Thesis, 2003.
[29] GOLDINGER, S. D.: *Echoes or Echoes? An Episodic Theory of Lexical Access,* Psychological Review, vol. 105, 2/1998, p. 251–279.
[30] SHOCKLEY, K., SABADINI, L., FOWLER, C. A.: *Imitation in Shadowing Words,* Perception and Psychophysics, vol. 66, 3/2004, p. 422–429.
[31] SEMMAR, Y.: *An Exploratory Study of Motivational Variables in a Foreign Language Learning Context,* Journal of Language and Learning, vol. 4, 1/2006, p. 118–132.
[32] RICHARDS, J. C., PLATT, J., PLATT, H.: *Longman Dictionary of Language Teaching and Applied Linguistics.* Harlow: Pearson Education Limited, 2002.
[33] CATELL, R. B., CATELL, A. K., CATELL, H. E. P.: *16-factor Personality Questionnaire (in Slovak)*, Bratislava: Psychodiagnostika, 1997.

COMMUNICATIONS – Scientific Letters of the University of Zilina
Writer's Guidelines

1. Submissions for publication must be unpublished and not be a multiple submission.
2. Manuscripts written **in English language** must include **abstract** also written in English. The submission should not exceed **10 pages** with figures and tables (format A4, Times Roman size 12). The **abstract** should not exceed 10 lines.
3. Submissions should be sent: **by e-mail** (as attachment in application MS WORD) to one of the following addresses: *komunikacie@uniza.sk* or *holesa@uniza.sk* or *vrablova@uniza.sk* or *polednak@fsi.uniza.sk* **with a hard copy** (to be assessed by the editorial board) **or on a CD** with a hard copy to the following address: Zilinska univerzita, OVaV, Univerzitná 1, SK-010 26 Zilina, Slovakia.
4. Abbreviations, which are not common, must be used in full when mentioned for the first time.
5. Figures, graphs and diagrams, if not processed by Microsoft WORD, must be sent in electronic form (as GIF, JPG, TIFF, BMP files) or drawn in contrast on white paper, one copy enclosed. Photographs for publication must be either contrastive or on a slide.
6. References are to be marked either in the text or as footnotes numbered respectively. Numbers must be in square brackets. The list of references should follow the paper (according to **ISO 690**).
7. The author's exact **mailing address of the organisation where the author works, full names, e-mail address or fax or telephone number,** must be enclosed.
8. The editorial board will assess the submission in its following session. In the case that the article is accepted for future volumes, the board submits the manuscript to the editors for review and language correction. After reviewing and incorporating the editor's remarks, the final draft (before printing) will be sent to authors for final review and adjustment.
9. The deadlines for submissions are as follows: September 30, December 31, March 31 and June 30.

COMMUNICATIONS

SCIENTIFIC LETTERS OF THE UNIVERSITY OF ZILINA
VOLUME 11

Address of the editorial office:
Zilinská univerzita
Office for Science and Research
(OVaV)
Univerzitna 1
SK 010 26 Zilina
Slovakia
E-mail: komunikacie@nic.uniza.sk,
polednak@fsi.uniza.sk

Each paper was reviewed by two reviewers.

Journal is excerpted in Compendex and Scopus

It is published by the University of Zilina in
EDIS – Publishing Institution of Zilina University
Registered No: 1989/98
ISSN 1335-4205

Published quarterly

Single issues of the journal can be found on:
http://www.uniza.sk/komunikacie